Studies on Transition Metal Oxide Catalysts for Waste Gas Treatment

RYOJI KUMA

2021

Copyrights

Chapter 2

This is a post-peer-review, pre-copyedit version of an article published in Topics in Catalysis. The final authenticated version is available online at: http://dx.doi.org/10.1023/A:1013897331031

Chapter 3

© 2020. This manuscript version is made available under the CC-BY-NC-ND 4.0 license http://creativecommons.org/licenses/by-nc-nd/4.0/ http://dx.doi.org/10.1016/j.apcata.2020.117496

Chapter 4

This document is the Accepted Manuscript version of a Published Work that appeared in final form in Industrial & Engineering Chemistry Research, copyright © American Chemical Society after peer review and technical editing by the publisher. To access the final edited and published work see http://dx.doi.org/10.1021/acs.iecr.0c02308.

Chapter 5

This is the peer reviewed version of the following article: *ChemCatChem* **2020**, *12*, 5938–5947, which has been published in final form at http://dx.doi.org/10.1002/cctc.202001155. This article may be used for non-commercial purposes in accordance with Wiley Terms and Conditions for Use of Self-Archived Versions.

Preface

Ever since the 18th century, the world's industrial structure and economy have made remarkable progress triggered by the Industrial Revolution, and an affluent society has been realized by the explosive increase in productivity. Among them, transportation technologies such as automobiles, and heavy industry powered by fossil fuels, have greatly contributed to the development of human society. However, in exchange for their abundance, serious environmental pollution has been caused. Among these pollutants, nitrogen oxides (NO_x=NO, NO_2) are known to cause acid rain and photochemical smog, which adversely affect animals, plants, and human health, and a wide variety of technologies to reduce NO_x (de-NO_x) have been developed all over the world.

The catalytic treatment method has been widely employed for emission control of NO_x generated from mobile sources such as automobiles, and those from stationary sources such as power plants. Pt-Pd-Rh-based de-NO_x catalysts, generally called three-way catalysts, are mainly used for automotive exhaust gas treatment, and V_2O_5/TiO_2-type catalysts for power plants. From the viewpoints of cost reduction and protection of rare resources, the reduction of the loading amount of precious metals on the automotive catalysts has been required. Thus, dedicated research and developments for the improvement of catalysts have been ongoing from both academic and industrial sides.

In addition, NO_x is also emitted from municipal waste incineration plants, and the exhaust gas contains dioxins, which has significant toxicity such as teratogenicity. It is known that the V_2O_5/TiO_2 catalyst also has dioxins decomposition activity, hence a simultaneous NO_x and dioxins removal using one catalytic treatment device has been adopted. To obtain a catalyst suitable for such simultaneous removal, improvements have been made based on the conventional V_2O_5/TiO_2 catalyst. For further breakthrough of

such exhaust gas treatment catalyst performance, not only conventional trial-and-error by field test on an actual scale, but also characterization utilizing cutting-edge analysis technology such as X-ray absorption fine structure spectroscopy (XAFS) is essential.

In this thesis, the author focuses on the research conducted for unraveling the factors effective for the improvement of activity and durability of de-NO_x catalysts, using non-precious, transition metal oxides as active species. The author investigated the local structure, redox behavior, and deactivation mechanism on these catalysts in detail, by means of spectroscopic analyses such as XAFS. Further, by utilizing the knowledges obtained from these studies, the author succeeded in developing a high-performance de-NO_x catalyst for low temperatures, with excellent catalyst activity and durability.

A part of the studies in the present thesis was conducted at Department of Molecular Engineering, Graduate School of Engineering, Kyoto University from 1997 to 1999, under the supervision of Professor Satohiro Yoshida, Professor Takuzo Funabiki, and Professor Tsunehiro Tanaka. Other parts of the studies were performed at Catalyst Research Laboratory of Nippon Shokubai Co., Ltd. from 1999 to 2020. The author has been studying the transition metal oxide catalysis for the de-NO_x reaction, from the viewpoint of physico-chemical investigation of catalysts, aiming to develop new catalysts with excellent performance.

The author wishes to express his sincere appreciation to Professor Tsunehiro Tanaka for his valuable and instructive guidance over the studies in Kyoto University, and subsequent cooperation throughout the work in Nippon Shokubai Co., Ltd. The author would like to express his special appreciation to Professor Satohiro Yoshida and Professor Takuzo Funabiki for their insightful instructions concerning catalyst sciences and fruitful discussions regarding the present study.

The author also wishes to express his appreciation to Professor Hirofumi Aritani

at Saitama Institute of Technology, Dr. Takashi Yamamoto at Tokushima University, Dr. Yoshiumi Kohno at Shizuoka University, and Dr. Saburo Hosokawa, Dr. Kentaro Teramura, and Dr. Hiroyuki Asakura at Kyoto University for their cooperation in experiments and helpful advices. The author gratefully acknowledges Professor Kazu Okumura at Kogakuin University for his kind cooperation and insightful advices for the measurements and analyses of XAFS spectra. The author also acknowledges Dr. Ken-ichi Kimijima at High Energy Accelerator Research Organization (KEK-PF) for his helpful aid in the measurement of *in-situ* XAFS.

The author would like to express his gratitude to his managers, Dr. Kazuhiko Murata and Atsushi Morita for their comprehensive supports for the studies at Nippon Shokubai Co., Ltd. The author is grateful to Dr. Tomoyuki Kitano and Mr. Takuya Tsujiguchi for their dedicated cooperation and fruitful discussion throughout the present study. The author would like to express his thanks to his colleagues, Mr. Hiroki tsutsumi, Mr. Masafumi Sugio, Mr. Yoshio Nakamura, Mr. Takuya Tsujiguchi, and Dr. Yuta Tanaka for their cooperation, especially in overnight XAFS experiments at KEK-PF. Many thanks to Mr. Etsushige Matsunami and Ms. Akiko Kuriyama for their helps on XPS measurement.

The author also would like to express his appreciations for his wife, Taeko, for her dedicated helps. Finally, the author would like to offer his heartfelt gratitude to his parents, Hiromi and Mariko, for their sincere support.

Ryoji Kuma

Hyogo,

November, 2020

-CONTENTS-

Chapter 1

General Introduction

1. Developments in non-PGM automotive catalysts

The abatement of NO_x generated in the combustion of fossil fuels has been a common issue in the world, and enormous technological developments have been made to solve the problem. Catalytic NO_x treatment is one of the important technologies for the NO_x abatement, and Pt-Pd-Rh-based three-way catalysts have been mainly used as automotive catalysts. Additionally, a great deal of research on the catalysts using Ag, Fe, and Cu as active species has been conducted as well, to decrease the usage of expensive precious-metal-group materials [1–6].

In the 1990s, Iwamoto et al. reported that Cu/ZSM-5 catalysts showed excellent activity for the selective catalytic reduction of NOx using hydrocarbon as a reducing agent (HC-SCR) [7,8], and special attentions were paid on the research of copper zeolite-based HC-SCR catalysts. Although conventional three-way catalysts do not show sufficient activity under excess oxygen [9], the HC-SCR reaction on the Cu/ZSM-5 catalyst is promoted by the presence of oxygen [10]. Thus, Cu-based catalysts for oxygen-rich exhaust gas applications such as lean burn engines and diesel engines have been researched by academic and industrial researchers. Three types of zeolites, ferrierite (FER), ZSM-5 (MFI), and mordenite (MOR), have been studied as support materials for Cu catalysts [11], and the HC-SCR activities using C_2H_4 are in the following order; Cu-MFI > Cu-MOR = Cu-FER > Cu-Y. It is well known that preparation methods play

important roles for the HC-SCR activity, where ion-exchange is superior to impregnation or precipitation methods [12]. Cu/Al_2O_3 is also active for HC-SCR [13], and Yoshida et al. reported that tetrahedrally coordinated Cu^{2+} species act as active sites for NO-CO-C_3H_6-O_2 reaction [14]. Ag/Al_2O_3 catalysts have been studied as one of non-platinum group catalysts, which exhibit a good HC-SCR activity in a wide temperature window [15–18]. The addition of second material has been studied to modify the Al_2O_3 support of Ag/Al_2O_3 catalysts, and the addition of Cs or Mg demonstrated remarkably improved activity, with and without SO_2, by suppressing the growth of Ag particles [18].

On the other hand, developments on the application of SCR using NH_3 or urea as a reducing agent (NH_3-SCR) to the automotive exhaust gas treatment has advanced in recent years. The details of the NH_3-SCR using V_2O_5/TiO_2-based catalysts are described in the following section. In addition to conventional V_2O_5 catalysts, Ag-, Fe-, and Cu-based catalysts were found to possess good activities for the NH_3-SCR [19–21]. Analogous to the case of HC-SCR, zeolites such as ZSM-5, MOR, FER, and beta (BEA) have been reported to be suitable as the support materials for Cu catalysts [22,23]. Recently, the zeolites with small pores such as SAPO-34 and SSZ-13, both having chabazite (CHA) structure, have been focused on [23]. Hamoud et al. reported that dispersed isolated Cu^+/Cu^{2+} species, which are active sites for low-temperature NH_3-SCR, are responsible for an excellent activity of Cu-SAPO-34 catalyst at low temperatures (< 300 °C) [24]. Furthermore, as Fe-ZSM-5 catalysts exhibit superior performances at higher temperatures (300–450 °C), a dual layer catalyst combining Cu-CHA with Fe-ZSM-5 was reported by Metkar et al. [25]. If these NH_3-SCR technologies can be widely employed as an automotive exhaust gas treatment method, cost reduction effect can be expected by applying these non-platinum group metal catalysts.

2. NH_3-SCR catalysts for stationary sources

The NH_3-SCR technology is known as proven method for treating exhaust gases from the stationary sources such as power plants, and has been adopted worldwide due to its efficiency and economics [26,27]. The NH_3-SCR is shown by the reaction formulae as follows;

$$4NO + 4NH_3 + O_2 \rightarrow 4N_2 + 6\ H_2O$$

$$2NO_2 + 4NH_3 + O_2 \rightarrow 3N_2 + 6\ H_2O$$

$$NO + NO_2 + 2NH_3 \rightarrow 2N_2 + 3H_2O$$

NO_x is selectively reduced to produce N_2 and water, even in the presence of excess oxygen.

In 1957, NH_3-SCR was patented by Engelhard corporation, wherein precious metals, Co, Ni, and Fe were listed as active species of catalysts [27–29]. Supported noble metal catalysts exhibit the NH_3-SCR activity. However, these catalysts have disadvantages of high cost and low selectivity, namely, a high amount of N_2O is produced at low temperatures [30], and the decomposition of NH_3 proceeds at high temperatures [31,32], therefore sufficient treatment performance cannot be obtained.

Afterwards, catalyst improvement was promoted mainly in Japan and the United States [27], and a low-cost V_2O_5/TiO_2 catalysts that exhibit good activity and selectivity was developed in the 1960s. The V_2O_5/TiO_2 catalysts were put into practical use in the 1970s by a great deal of efforts of Hitachi Zosen, Nippon Shokubai, and IHI [27,33,34], and these catalysts have been contributing to the purification of the exhaust gases from stationary sources. For the requirement to suppress plugging by dust and reducing pressure loss, monolithic catalysts with parallel channels such as plate-, corrugated-, and

honeycomb-type catalysts have been employed (Figure 1).

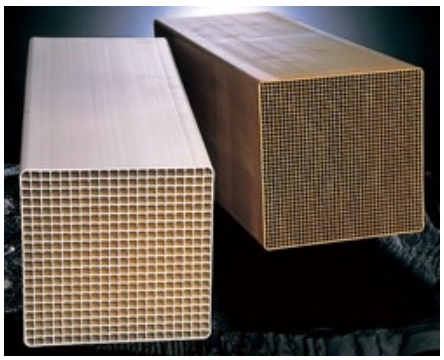

Figure 1. Honeycomb-monolith SCR catalyst

Figure 2 illustrates a conventional power plant flue gas treatment process. Exhaust gas containing harmful substances such as NO_x and SO_x generated by combustion in a boiler is introduced into a SCR reactor after adding NH_3. Subsequently, dust contained in the flue gas is removed by an electric dust collector, SO_x is removed by a desulfurizer, and then the treated gas is discharged from a stack. The main deteriorating factors of the NH_3-SCR catalyst are (1) pore blockage due to the accumulation of NH_4HSO_4 (ammonium bisulfate, ABS) at low temperature [35–38], and (2) sintering of active species at high temperature [39–41]. To avoid these deteriorations, a temperature range of 300–400 °C is considered to be optimum, and the decomposition of NH_3 can be suppressed in this temperature range.

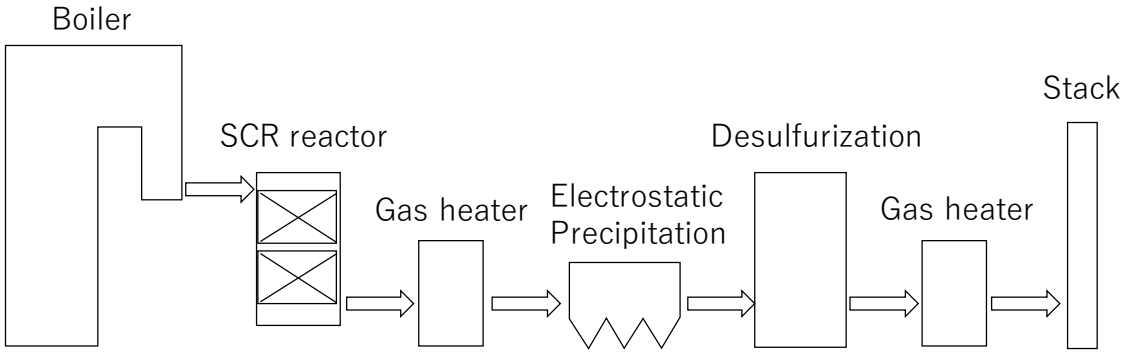

Figure 2. Typical emission control process for flue gas from a power plant.

However, even at the temperature range of 300–400 °C, the V_2O_5/TiO_2 catalysts gradually deteriorate due to the ABS accumulation and sintering. Further catalyst improvements for these problems led to the development of V_2O_5-WO_3/TiO_2 commercial catalysts [42–44]. The catalytic activity and lifetime were significantly improved owing to the addition of WO_3, which increases acidity, thermal stability, and SO_2 durability. Even after the commercialization of the V_2O_5-WO_3/TiO_2 catalyst, there has been a demand for further improvement of catalytic performance to reduce the catalyst volume, for cost advantage.

It is well-known that the surface acidity is a crucial factor for the NH_3-SCR performance. NH_3 is adsorbed on the surface acid sites such as V^{5+}-OH and then reacts with NO [45,46]. Therefore, controlling the surface acidity has been considered to be important for the improvement of the catalytic activity. According to literature reports, WO_3 is effective for enhancing the surface acidity of V_2O_5/TiO_2 catalysts [47–51], and surface sulfates are also known to increase the acidity [52–54]. However, Kobayashi et al. reported that too strongly adsorbed NH_3 on the acid sites is not preferable for the NH_3-SCR reaction, indicating that more stringent acidity control is required for further development of the active catalysts.

3. Dioxins decomposition catalysts

NO_x and SO_x are known to exist in the flue gas from municipal waste incinerators, and what is worse, a small amount of dioxins are also contained, as reported by Olie et al. in 1977 [55]. The term “Dioxins” refers to 75 types of Polychlorinated dibenzo-*p*-dioxins (PCDDs), 135 types of Polychlorinated dibenzofurans (PCDFs), and 12 types of Polychlorinated biphenyls (PCBs) (Figure 3). Toxicity varies depending on the number and position of chlorine bonded to the benzene ring.

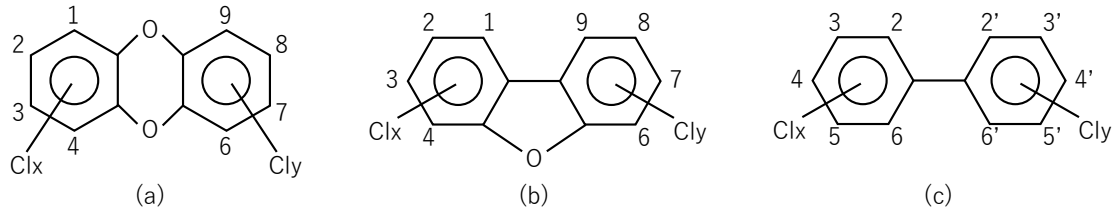

Figure 3. General chemical structures of (a) PCDDs, (b) PCDFs, and (c) PCBs.

Afterwards, a great number of waste gas treatment technologies for the decomposition of dioxins were extensively investigated mainly in Germany and Sweden [56,57]. Several dioxins removal processes are adopted today, such as the injection of pulverized lime and activated carbon, in combination with the improvement of combustion efficiency. In addition, fabric filters have been employed to collect dioxins adhering to fly ashes, as well as dioxin droplets.

A typical flue gas treatment process for a municipal waste incinerator equipped with a fabric filter is shown in Figure 4. Generally, resins such as PTFE and heat-resistant nylon are used as the material for the fabric filter [58]. Due to its low heat-resistance, the

exhaust gas from the incineration boiler is cooled to ~150 °C before introducing into the fabric filter [59].

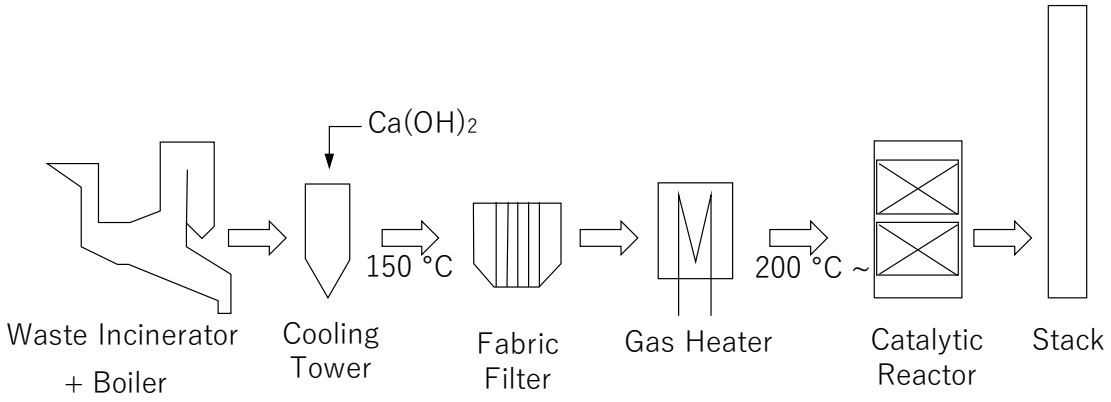

Figure 4. Typical flue gas treatment flow for the removal of dioxins and NO_x from a municipal waste incineration plant.

Furthermore, as it was difficult to obtain a sufficient efficiency for the dioxins abatement using these technologies, the catalytic dioxins decomposition process was employed. The development of catalysts exhibiting a high decomposing efficiency for dioxins has been studied by many researchers. In 1987, Hagenmaier et al. reported that copper is active for the decomposition of dioxins [56]. CrO_x/TiO_2 catalysts exhibited a good decomposition efficiency at 325 °C [60], but these catalysts are not suitable due to a high toxicity of Cr itself. Mn-based catalysts such as MnO_x/TiO_2 and MnO_x/Al_2O_3 are also active for the decomposition of dioxins [61,62], however, these catalysts deactivates due to the presence of Cl [63].

On the contrary, the V_2O_5/TiO_2 SCR catalysts were found to exhibit an excellent activity for the decomposition of dioxins, and durability against Cl [63–66]. These catalysts enabled a simultaneous abatement of dioxins and NO_x in the flue gas from the waste incinerators. As shown in Figure 4, The catalytic reactor is placed after the fabric filter to prevent catalyst poisoning and physical blockage by the dust. At the low temperatures

such as 150 °C, as the catalytic activity is very low and the deactivation by the ABS accumulation is accelerated, the flue gas after the fabric filter is generally re-heated using a gas heater to ~200 °C.

From the viewpoint of understanding the dioxins decomposition mechanisms, the importance of dechlorination step has been argued among researchers. Yang et al. studied the decomposition of dioxins over V_2O_5-WO_3/TiO_2 catalysts, describing that highly chlorinated dioxins were converted to lowly chlorinated dioxins via dechlorination assisted by OH radical [67]. In the literature reported by Larrubia et al. [68], they concluded that the dechlorination from dioxins is not a crucial step for the decomposition reaction. Additionally, the intramolecular oxygen bridge in dioxins is considered to be adsorbed to V_2O_5-WO_3/TiO_2 catalyst more preferentially than terminal Cl [69]. According to these reports, the dechlorination step may not be crucial for the entire mechanisms of the dioxins decomposition reaction.

Several researchers have been studying the dioxins decomposition catalyst using actual PCDDs and PCDFs [67–72], but as dioxins are extremely harmful to human health, most researchers use alternative substances such as chlorotoluene, chlorobenzene, or chlorophenol in their research on V_2O_5/TiO_2-type decomposition catalysts [73,74]. However, these studies focused on the reactions in the temperature ranges higher than 200 °C, therefore, further studies on the low-temperature catalytic decomposition of dioxins are required.

4. Low-temperature SCR catalysts

As shown in Figure 2, the NH_3-SCR catalyst is generally located just after the boiler in the treatment of exhaust gas from power plants, to operate the catalyst at the

temperatures higher than 300 °C. In this case, the catalyst deteriorates due to catalyst poisons such as alkalis, phosphorus, and heavy metals contained in the dust in the flue gas, as well as attrition by the dust. On the contrary, if a catalyst that can operate at a low temperature such as 200 °C or less is developed, the catalyst can be located after an electrostatic precipitator or a desulfurizer, and the catalytic reaction system with a longer life is expected. Moreover, as NO_x is also included in the flue gas from the municipal waste incinerators (Figure 4), low-temperature activity is required for the simultaneous NO_x/dioxins abatement mentioned above. Therefore, an NH_3-SCR catalyst that exhibits high activity at low temperature is demanded.

A number of studies have been published investigating low-temperature NH_3-SCR catalysts such as Mn-, Fe-, and V-based catalysts. Mn-Ce/TiO_2 catalysts are known to be highly active at low temperature ~150 °C, owing to an enhanced redox capability of MnO_x induced by active oxygen species in CeO_x [75–78]. However, Mn-based catalysts have the problem of a deactivation due to H_2O and SO_2 [79]. Although the improvement of durability for these catalysts have been studied by several researchers [80,81], further improvement is required for practical use.

In contrast, V_2O_5-WO_3/TiO_2 and V_2O_5-MoO_3/TiO_2 have been employed for the low-temperature NH_3-SCR in the practical stationary sources, owing to their durability against SO_2 [82–85]. It is known that MoO_3 is the more effective promoter than WO_3 at low temperatures, for both catalytic activity and durability [82,85]. However, as the deactivation due to the accumulation of ammonium sulfate salts such as ABS is accelerated at the temperatures lower than 200 °C, the improvement of activity and durability is required.

It is agreed by researchers that the process of reoxidizing V^{4+} generated in the catalytic reaction cycle to V^{5+} by gas phase oxygen is a rate-determining step at low temperatures [26,49,86–89]. On the other hand, the presence of dispersed two-dimensional

polymeric vanadate has been considered to be crucial for the low-temperature NH_3-SCR activity [39,90–93]. The redox capability of vanadium species is enhanced by a greater mobility of lattice oxygen in the polymeric vanadate species [39], which should accelerate the reoxidation of V^{4+} toV^{5+} at low temperatures.

5. Outline of the present thesis

The main purpose of this thesis is the investigation of the factors affecting the performance of waste gas treatment catalysts using transition metal oxides as active species, for the development of new catalysts. The author has been engaged in various analysis methods focusing on the local structure of active sites on catalysts. Among them, XAFS is a very powerful tool for analyzing local structure [94] and electronic state [95] of active species, and has been established as a general catalytic analysis method today. In recent years, an increasing number of reports have been published on *in-situ* XAFS [96–100], a method for structural and electronic analysis of the catalyst under actual reaction conditions, and it is greatly contributing to obtaining detailed information on the state of the active species during the reaction.

Chapter 2 describes the study on the copper-based automotive catalysts, clarifying the relationship between catalytic activity and local structure of active sites. The catalytic activity is tested for NO-CO reaction in the presence of O_2 over Cu/Al_2O_3, which is one of basic reactions in SCR. Further, the local structure of active sites on this catalyst is characterized in detail, using Cu K-edge XAFS analyses in combination with UV/VIS/NIR. The catalytic activity of Cu/Al_2O_3 is affected by the factors such as valence state, dispersion, and local geometry of active sites, and the author has been trying to

control these factors by Cu loading amount and calcination conditions of the catalyst. Obtained knowledges on the XAFS analysis in this study is applied to the analyses of catalysts in Chapters 3 and 4.

Chapters 3, 4, and 5 deal with physico-chemical characterizations of V_2O_5/TiO_2-SiO_2-MoO_3 (V/TSM) commercial catalyst developed by the author, which exhibits excellent activity and durability for the simultaneous NO_x/dioxins purification reaction at low temperatures. TiO_2-SiO_2-MoO_3 (TSM) mixed oxide, support material of V/TSM, is prepared via coprecipitation method, wherein molybdenum oxide species are highly dispersed. The mechanism for the superior performance of V/TSM is investigated by comparing with other catalysts such as V_2O_5/TiO_2-SiO_2, V_2O_5-MoO_3/TiO_2, and V_2O_5-MoO_3/TiO_2-SiO_2 that are conventionally employed for practical use.

In Chapter 3, the effects of support material of V/TSM on dioxins decomposition performance are studied. The structure of TSM is investigated by means of Mo K-edge and Ti K-edge XAFS, and the role of molybdenum oxide in the V/TSM catalyst is discussed. In this chapter, the author clarifies the formation of TSM solid solution based on these analysis results. The coexistence of Mo and Ti in the TSM solid solution is expected to be effective for the enhancement of redox capability, which is crucial for the dioxins decomposition activity at low temperatures. The information on this TSM solid solution plays important roles for discussions in Chapters 4 and 5 as well.

Chapter 4 elucidates the mechanism of the supreme activity of the V/TSM catalyst for low-temperature NH_3-SCR. Redox behaviors of vanadium species, which is considered to be a key factor for improving the low-temperature NH_3-SCR activity, are

studied by means of temperature-programmed reduction experiments with H_2 and in-situ V K-edge X-ray absorption near-edge structure method. According to the author's previous study [101], polymeric vanadate species are formed on V/TSM, and it is one of the purposes in Chapter 4 to obtain further information on the polymeric vanadate. The relationship between local geometry around the vanadium species and NH_3-SCR activity is discussed, focusing on reducibility and reoxidizability of vanadium oxides on the V/TSM catalyst.

The V/TSM catalyst exhibits not only high activities for NH_3-SCR and dioxins decomposition, but also an excellent durability against SO_2. In Chapter 5, the deactivation mechanism by SO_2 is studied using Fourier transform infrared spectroscopy and temperature programmed desorption. As described above, it is known that the deactivation of NH_3-SCR catalysts is caused by the accumulation of ammonium sulfate compounds such as ABS. These sulfates are generally considered to be formed via the oxidation of SO_2 to SO_3, however, this oxidation can hardly proceed at low temperatures (< 200 °C). To solve this question, the author presents a new deactivation mechanism at low temperatures throughout this study, and the origin of the improved durability of the V/TSM catalyst is presumed from decomposition and desorption behaviors of accumulated ammonium sulfate salts.

References

[1] K. Theinnoi, S. Sitshebo, V. Houel, R. R. Rajaram, A. Tsolakis, *Energy & Fuels* **2008**, *22*, 4109–4114.

[2] R. Burch, J. P. Breen, F. C. Meunier, *Appl. Catal. B Environ.* **2002**, *39*, 283–303.

[3] A. Battiston, *J. Catal.* **2003**, *218*, 163–177.

[4] K. Shimizu, J. Shibata, A. Satsuma, *J. Catal.* **2006**, *239*, 402–409.

[5] T. Yamamoto, T. Tanaka, R. Kuma, S. Suzuki, F. Amano, Y. Shimooka, Y. Kohno, T. Funabiki, S. Yoshida, *Phys. Chem. Chem. Phys.* **2002**, *4*, 2449–2458.

[6] A. J. Binder, T. J. Toops, R. R. Unocic, J. E. Parks, S. Dai, *Angew. Chemie Int. Ed.* **2015**, *54*, 13263–13267.

[7] M. Iwamoto, in *Stud. Surf. Sci. Catal.*, **1990**, pp. 121–143.

[8] S. Sato, Y. Yu-u, H. Yahiro, N. Mizuno, M. Iwamoto, *Appl. Catal.* **1991**, *70*, L1–L5.

[9] S. Matsumoto, *Catal. Today* **2004**, *90*, 183–190.

[10] G. Centi, S. Perathoner, L. Dall'Olio, *Appl. Catal. B Environ.* **1996**, *7*, 359–377.

[11] R. Mrad, A. Aissat, R. Cousin, D. Courcot, S. Siffert, *Appl. Catal. A Gen.* **2015**, *504*, 542–548.

[12] Z. Chajar, M. Primet, H. Praliaud, M. Chevrier, C. Gauthier, F. Mathis, *Appl. Catal. B Environ.* **1994**, *4*, 199–211.

[13] C. Márquez-Alvarez, I. Rodríguez-Ramos, A. Guerrero-Ruiz, G. L. Haller, M. Fernández-García, *J. Am. Chem. Soc.* **1997**, *119*, 2905–2914.

[14] H. Yoshida, T. Hirakawa, H. Oyama, R. Nakashima, S. Hinokuma, M. Machida, *J. Phys. Chem. C* **2019**, *123*, 10469–10476.

[15] T. Miyadera, *Appl. Catal. B Environ.* **1993**, *2*, 199–205.

[16] K. Shimizu, J. Shibata, H. Yoshida, A. Satsuma, T. Hattori, *Appl. Catal. B Environ.* **2001**, *30*, 151–162.

[17] N. Bogdanchikova, *Appl. Catal. B Environ.* **2002**, *36*, 287–297.

[18] P. M. More, *J. Environ. Manage.* **2017**, *188*, 43–48.

[19] B. Guan, R. Zhan, H. Lin, Z. Huang, *Appl. Therm. Eng.* **2014**, *66*, 395–414.

[20] K. Shimizu, A. Satsuma, *Appl. Catal. B Environ.* **2007**, *77*, 202–205.

[21] S. Shwan, J. Jansson, L. Olsson, M. Skoglundh, *Catal. Today* **2015**, *258*, 432–440.

[22] A. Sultana, T. Nanba, M. Sasaki, M. Haneda, K. Suzuki, H. Hamada, *Catal. Today* **2011**, *164*, 495–499.

[23] J. H. Kwak, D. Tran, S. D. Burton, J. Szanyi, J. H. Lee, C. H. F. Peden, *J. Catal.* **2012**, *287*, 203–209.

[24] H. I. Hamoud, V. Valtchev, M. Daturi, *Appl. Catal. B Environ.* **2019**, *250*, 419–428.

[25] P. S. Metkar, M. P. Harold, V. Balakotaiah, *Chem. Eng. Sci.* **2013**, *87*, 51–66.

[26] P. Forzatti, *Appl. Catal. A Gen.* **2001**, *222*, 221–236.

[27] T. Boningari, P. G. Smirniotis, *Curr. Opin. Chem. Eng.* **2016**, *13*, 133–141.

[28] J. Cohn, D. Steele, H. Andersen, *U.S. Patent 2975025*, **1961**.

[29] H. Andersen, C. Keith, *U.S. Patent 3008796*, **1961**.

[30] M. D. Amiridis, T. Zhang, R. J. Farrauto, *Appl. Catal. B Environ.* **1996**, *10*, 203–227.

[31] F. Acke, M. Skoglundh, *Appl. Catal. B Environ.* **1999**, *20*, 133–144.

[32] M. Kang, D. Kim, E. Park, J. Kim, J. Yie, S. Kim, L. Hopeweeks, E. Eyring, *Appl. Catal. B Environ.* **2006**, *68*, 21–27.

[33] A. Inoue, K. Horie, K. Saito, Y. Aoki, T. Ono, T. Ohara, *U.S. Patent 4018706*,

1977.

[34] J.-K. Lai, I. E. Wachs, *ACS Catal.* **2018**, *8*, 6537–6551.

[35] F. Nakajima, I. Hamada, *Catal. Today* **1996**, *29*, 109–115.

[36] Z. Zhu, Z. Liu, S. Liu, H. Niu, *Appl. Catal. B Environ.* **2001**, *30*, 267–276.

[37] D. W. Kwon, K. H. Park, S. C. Hong, *Chem. Eng. J.* **2016**, *284*, 315–324.

[38] Y. Xi, N. A. Ottinger, Z. G. Liu, *Appl. Catal. B Environ.* **2014**, *160–161*, 1–9.

[39] I. Nova, L. Dall'Acqua, L. Lietti, E. Giamello, P. Forzatti, *Appl. Catal. B Environ.* **2001**, *35*, 31–42.

[40] L. Lietti, I. Nova, G. Ramis, L. Dall'Acqua, G. Busca, E. Giamello, P. Forzatti, F. Bregani, *J. Catal.* **1999**, *187*, 419–435.

[41] M. Kobayashi, K. Miyoshi, *Appl. Catal. B Environ.* **2007**, *72*, 253–261.

[42] M. A. Vuurman, I. E. Wachs, A. M. Hirt, *J. Phys. Chem.* **1991**, *95*, 9928–9937.

[43] E. Tronconi, I. Nova, C. Ciardelli, D. Chatterjee, M. Weibel, *J. Catal.* **2007**, *245*, 1–10.

[44] M. D. Amiridis, J. P. Solar, *Ind. Eng. Chem. Res.* **1996**, *35*, 978–981.

[45] N.-Y. Topsøe, H. Topsøe, *Catal. Today* **1991**, *9*, 77–82.

[46] N.-Y. Topsøe, *Science.* **1994**, *265*, 1217–1219.

[47] J. P. Chen, R. T. Yang, *Appl. Catal. A Gen.* **1992**, *80*, 135–148.

[48] L. Lietti, J. L. Alemany, P. Forzatti, G. Busca, G. Ramis, E. Giamello, F. Bregani, *Catal. Today* **1996**, *29*, 143–148.

[49] L. Lietti, P. Forzatti, F. Bregani, *Ind. Eng. Chem. Res.* **1996**, *35*, 3884–3892.

[50] D. E. Doronkin, F. Benzi, L. Zheng, D. I. Sharapa, L. Amidani, F. Studt, P. W. Roesky, M. Casapu, O. Deutschmann, J.-D. Grunwaldt, *J. Phys. Chem. C* **2019**, *123*, 14338–14349.

[51] M. Zhu, J.-K. Lai, U. Tumuluri, Z. Wu, I. E. Wachs, *J. Am. Chem. Soc.* **2017**,

139, 15624–15627.

[52] J. Chen, *J. Catal.* **1990**, *125*, 411–420.

[53] M. Kobayashi, M. Hagi, *Appl. Catal. B Environ.* **2006**, *63*, 104–113.

[54] Y. Xu, X. Wu, Q. Lin, J. Hu, R. Ran, D. Weng, *Appl. Catal. A Gen.* **2019**, *570*, 42–50.

[55] K. Olie, P. L. Vermeulen, O. Hutzinger, *Chemosphere* **1977**, *6*, 455–459.

[56] H. Hagenmaier, H. Brunner, R. Haag, M. Kraft, *Environ. Sci. Technol.* **1987**, *21*, 1085–1088.

[57] H. Miller, S. Marklund, I. Bjerle, C. Rappe, *Chemosphere* **1989**, *18*, 1485–1494.

[58] C. Kanaoka, *KONA Powder Part. J.* **2019**, *36*, 88–113.

[59] M. Hiraoka, T. Fujii, K. Kashiwabara, K. Ieyama, M. Kondo, *Chemosphere* **1991**, *23*, 1439–1444.

[60] S. D. Yim, D. J. Koh, I.-S. Nam, *Catal. Today* **2002**, *75*, 269–276.

[61] Y. Liu, Z. Wei, Z. Feng, M. Luo, P. Ying, C. Li, *J. Catal.* **2001**, *202*, 200–204.

[62] Y. Liu, M. Luo, Z. Wei, Q. Xin, P. Ying, C. Li, *Appl. Catal. B Environ.* **2001**, *29*, 61–67.

[63] G. Busca, M. Baldi, C. Pistarino, J. M. Gallardo Amores, V. Sanchez Escribano, E. Finocchio, G. Romezzano, F. Bregani, G. P. Toledo, *Catal. Today* **1999**, *53*, 525–533.

[64] H. Hagenmaier, K.-H. Tichaczek, H. Brunner, G. Mittelbach, *Organohalogen Comp.* **1990**, *3*, 65–68.

[65] R. Weber, T. Sakurai, H. Hagenmaier, *Appl. Catal.* **1999**, *20*, 4–11.

[66] Y. Ide, K. Kashiwabara, S. Okada, T. Mori, M. Hara, *Chemosphere* **1996**, *32*, 189–198.

[67] C. C. Yang, S. H. Chang, B. Z. Hong, K. H. Chi, M. B. Chang, *Chemosphere*

2008, *73*, 890–895.

[68] M. A. Larrubia, G. Busca, *Appl. Catal. B Environ.* **2002**, *39*, 343–352.

[69] D. P. Debecker, R. Delaigle, P. Eloy, E. M. Gaigneaux, *J. Mol. Catal. A Chem.* **2008**, *289*, 38–43.

[70] R. Weber, *Appl. Catal. B Environ.* **1999**, *20*, 249–256.

[71] M. Yu, W. Li, X. Li, X. Lin, T. Chen, J. Yan, *Chemosphere* **2016**, *156*, 383–391.

[72] M. F. Yu, X. Q. Lin, X. D. Li, T. Chen, J. H. Yan, *Aerosol Air Qual. Res.* **2016**, *16*, 2011–2022.

[73] D. P. Debecker, R. Delaigle, K. Bouchmella, P. Eloy, E. M. Gaigneaux, P. H. Mutin, *Catal. Today* **2010**, *157*, 125–130.

[74] C. E. Hetrick, J. Lichtenberger, M. D. Amiridis, *Appl. Catal. B Environ.* **2008**, *77*, 255–263.

[75] P. G. Smirniotis, D. A. Peña, B. S. Uphade, *Angew. Chemie Int. Ed.* **2001**, *40*, 2479–2482.

[76] Z. Wu, R. Jin, Y. Liu, H. Wang, *Catal. Commun.* **2008**, *9*, 2217–2220.

[77] Z. Sheng, Y. Hu, J. Xue, X. Wang, W. Liao, *Environ. Technol.* **2012**, *33*, 2421–2428.

[78] T. Boningari, P. R. Ettireddy, A. Somogyvari, Y. Liu, A. Vorontsov, C. A. McDonald, P. G. Smirniotis, *J. Catal.* **2015**, *325*, 145–155.

[79] C. Gao, J.-W. Shi, Z. Fan, G. Gao, C. Niu, *Catalysts* **2018**, *8*, 11.

[80] Z. Wu, R. Jin, H. Wang, Y. Liu, *Catal. Commun.* **2009**, *10*, 935–939.

[81] Z. Sheng, Y. Hu, J. Xue, X. Wang, W. Liao, *J. Rare Earths* **2012**, *30*, 676–682.

[82] L. Lietti, I. Nova, P. Forzatti, *Top. Catal.* **2000**, *11–12*, 111–122.

[83] L. Zhu, Z. Zhong, H. Yang, C. Wang, *J. Environ. Sci.* **2017**, *56*, 169–179.

[84] L. Xu, C. Wang, H. Chang, Q. Wu, T. Zhang, J. Li, *Environ. Sci. Technol.* **2018**,

52, 7064–7071.

[85] D. W. Kwon, K. H. Park, H. P. Ha, S. C. Hong, *Appl. Surf. Sci.* **2019**, *481*, 1167–1177.

[86] R. Willi, B. Roduit, R. A. Koeppel, A. Wokaun, A. Baiker, *Chem. Eng. Sci.* **1996**, *51*, 2897–2902.

[87] L. Lietti, P. Forzatti, *J. Catal.* **1994**, *147*, 241–249.

[88] I. Nova, C. Ciardelli, E. Tronconi, D. Chatterjee, B. Bandl-Konrad, *AIChE J.* **2006**, *52*, 3222–3233.

[89] A. Marberger, D. Ferri, M. Elsener, O. Kröcher, *Angew. Chemie Int. Ed.* **2016**, *55*, 11989–11994.

[90] L. J. Alemany, L. Lietti, N. Ferlazzo, P. Forzatti, G. Busca, E. Giamello, F. Bregani, *J. Catal.* **1995**, *155*, 117–130.

[91] B. M. Weckhuysen, D. E. Keller, *Catal. Today* **2003**, *78*, 25–46.

[92] P. G. W. A. Kompio, A. Brückner, F. Hipler, G. Auer, E. Löffler, W. Grünert, *J. Catal.* **2012**, *286*, 237–247.

[93] I. E. Wachs, *Dalt. Trans.* **2013**, *42*, 11762.

[94] B.-K. Teo, P. A. Lee, *J. Am. Chem. Soc.* **1979**, *101*, 2815–2832.

[95] A. N. Mansour, J. W. Cook, D. E. Sayers, *J. Phys. Chem.* **1984**, *88*, 2330–2334.

[96] T. Yamamoto, T. Tanaka, S. Takenaka, S. Yoshida, T. Onari, Y. Takahashi, T. Kosaka, S. Hasegawa, M. Kudo, *J. Phys. Chem. B* **1999**, *103*, 2385–2393.

[97] A. Battiston, *J. Catal.* **2003**, *215*, 279–293.

[98] Y. Nagai, K. Dohmae, K. Teramura, T. Tanaka, G. Guilera, K. Kato, M. Nomura, H. Shinjoh, S. Matsumoto, *Catal. Today* **2009**, *145*, 279–287.

[99] D. E. Doronkin, M. Casapu, T. Günter, O. Müller, R. Frahm, J.-D. Grunwaldt, *J. Phys. Chem. C* **2014**, *118*, 10204–10212.

[100] K. Ueda, J. Ohyama, A. Satsuma, *Chem. Lett.* **2017**, *46*, 1390–1392.

[101] M. Kobayashi, R. Kuma, A. Morita, *Catal. Letters* **2006**, *112*, 37–44.

Chapter 2

NO Reduction with CO in the Presence of O_2 over Cu/Al_2O_3 — Structural Analysis of Active Species by Means of XAFS and UV/VIS/NIR Spectroscopy —

Abstract

The local structure around Cu supported on Al_2O_3 was determined by UV/VIS/NIR and XAFS spectroscopic techniques. The relationship between catalytic performance for NO-CO-O_2 reaction and the state of supported Cu species is discussed. A new method for estimating the fraction of aggregated to isolated Cu species is proposed.

1. Introduction

There have been many works on de-NO_x catalysts in a NO-hydrocarbons-O_2 system. However, there have only been a few works using an NO-CO-O_2 system because CO is easily oxidized to CO_2 without reducing NO_x. The author has found that a Cu/Al_2O_3 catalyst promotes NO reduction with CO in the presence of excess oxygen [1,2]. The catalytic performance is shown in Figure 1 [1]. The catalytic property depends strongly on the loading amount of Cu and the calcination temperature, and 0.5 wt% Cu/Al_2O_3 calcined at 773 K was found to be the most effective. The calcination procedure at 1073 K suppresses NO reduction capability, in contrast to the case for a NO-C_3H_6-O_2 system over $Cu–Al_2O_3$ [3,4].

The author has proposed that isolated Cu^{2+} species are active sites for NO-CO-O_2 reaction and that the coexistence of aggregated species drastically reduces the activity. Nevertheless, the existence of aggregated species has not been identified yet. The formation of crystalline CuO was faintly confirmed by XRD characterization on 5 wt% Cu/Al_2O_3 calcined at 773 K. In the case of 10 wt% Cu/Al_2O_3, it was demonstrated that CuO transformed into $CuAl_2O_4$ after calcination at 1073 K. However, the peaks due to $CuAl_2O_4$ were very broad, indicating that the crystallinity was quite low. XRD characterization reflects crystalline phases, the grain sizes of which are larger than 100 Å. Amorphous phases and fine crystallites are often silent in diffraction patterns. In the present study, the author characterized Cu species on Al_2O_3 by means of UV/VIS/NIR and XAFS to clarify the active species for NO-CO-O_2 reaction. Here, the author proposes a new method for estimating the fraction of aggregated Cu species on Al_2O_3.

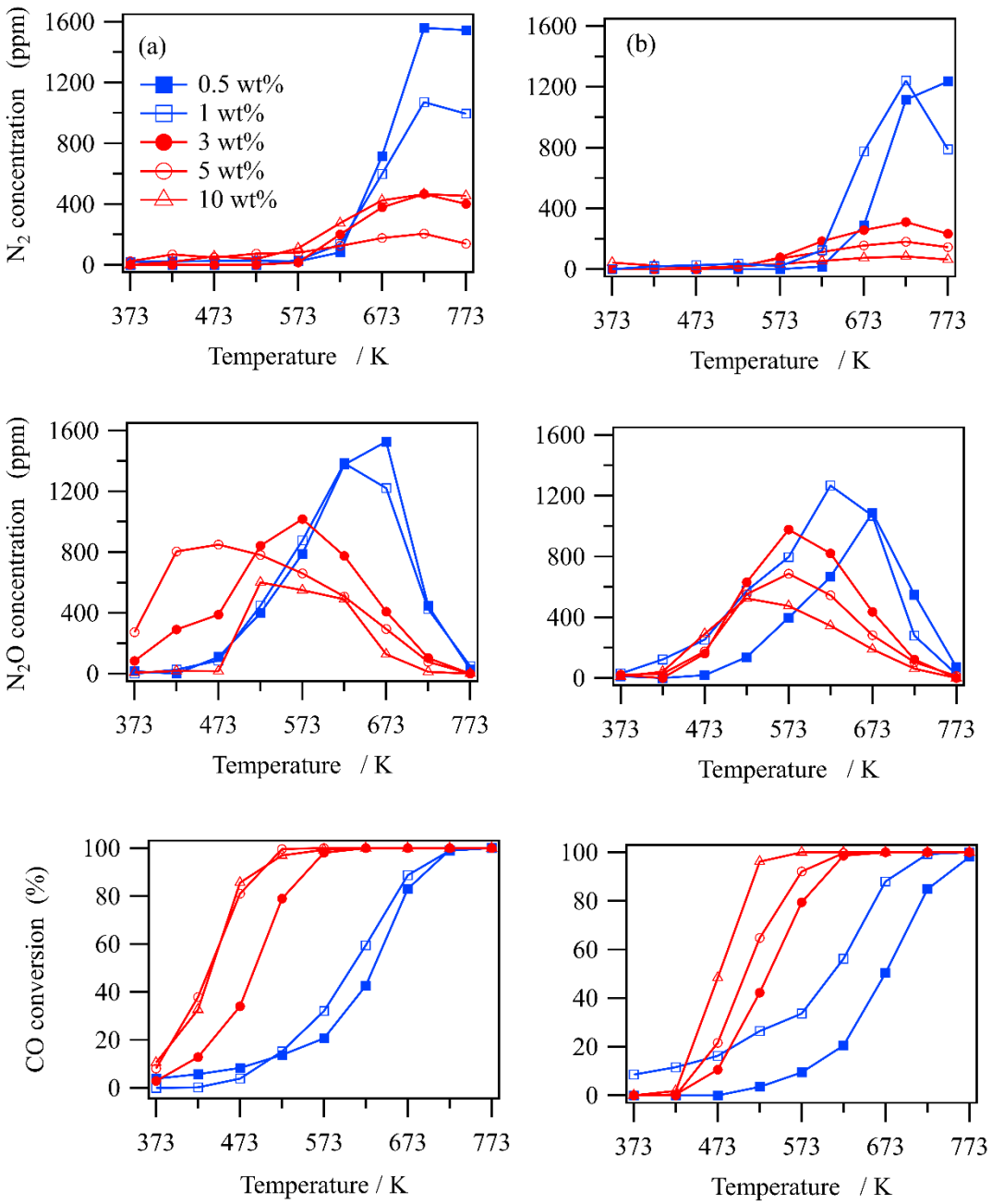

Figure 1. Results of NO-CO-O_2 reaction over Cu/Al_2O_3 calcined at 773 K (a) and 1073 K (b). NO: 1 %; CO: 1 %; O_2: 0.5 %, Ar: balance; Total flow rate: 100 ml min^{-1}; Catalyst: 200 mg. Taken from reference [1].

2. Experimental

An alumina-supported Cu catalyst was prepared by impregnation of γ-Al_2O_3 (JRC-ALO-4; 177 m^2 g^{-1}) with an aqueous solution of $Cu(NO_3)_2 \cdot 2H_2O$ (Wako, 99.9 %) at 353 K, followed by calcination at 773 K for 5 h. High-temperature-treated samples were prepared by further calcination at 1073 K for 12 h. Hereafter, *X*-Cu/Al_2O_3-*Y* denotes *X* wt% Cu/Al_2O_3 calcined at *Y* K. $CuAlO_2$ and $CuAl_2O_4$ were synthesized by citric acid processes. The NO-CO-O_2 reaction was carried out using a fixed bed flow reactor under atmospheric pressure [1]. After the reaction at 773 K, each sample was transferred into a polyethylene bag under a dry nitrogen atmosphere, and the bag was sealed to prevent exposure of the sample to air during XAFS measurement.

X-ray absorption experiments were carried out on the BL01B1 at SPring-8 (Hyogo, Japan. Proposal No. 1999A0083). The ring energy was 8 GeV, and stored current was 70-100 mA. X-ray absorption spectra were recorded in a fluorescence mode with a Si(111) two-crystal monochromator at room temperature. The energy was calibrated by the distinct peak at the Cu K-edge of a Cu foil as 8980.3 eV. Data reduction was performed using a FACOM M1800 computer in the Kyoto University Data Processing Center. The normalization method has been previously reported in detail [5]. Fourier transformation was performed on EXAFS in the range of 3.5 - 14 $Å^{-1}$. For curve-fitting analysis, backscattering amplitude and phase shift functions for a Cu-O pair were obtained from a k^3-weighted EXAFS spectrum of a NiO crystal. Diffuse reflectance UV/VIS/NIR spectra were measured with a Lambda-19 spectrometer (Perkin-Elmer) equipped with a reflectance spectroscopy accessory RSA-PE-19 (Labsphere).

3. Results and Discussions

3.1 XANES

Figure 2 shows XANES spectra and their first derivatives of 0.5-Cu/Al_2O_3-773 and reference compounds. The XANES spectra of Cu_2O and $CuAlO_2$ exhibit a single strong peak due to 1s-4pπ transition around 8980 eV, which is characteristic to Cu^+ species [6–8]. A small preedge peak due to *1s-3d* transition is observed in XANES spectra of Cu^{2+} species (d^9). Although this transition is formally dipole-forbidden, it becomes more intense as the symmetry is distorted from a regular octahedron [9].

The coordination environments of CuO (Cu-O; 1.96 Å ×4 + 2.78 Å ×2) and $Cu(OH)_2$ (Cu-O; 1.94 Å ×4 + 2.63 Å ×2) [10] are fundamentally similar, but the CuO_6 unit in $Cu(OH)_2$ is much more distorted. As a result, the peak intensity due to *1s-3d* transition of $Cu(OH)_2$ (distorted O_h symmetry) was larger than that of CuO (D_{4h} symmetry). Because the majority of Cu species in a $CuAl_2O_4$ spinel are in tetrahedral coordination [11], the *1s-3d* peak is much more intense than the other Cu^{2+} species. Furthermore, the peak energy of T_d species ($CuAl_2O_4$) was found to be lower than that of O_h species ($Cu(OH)_2$) by 1.0 eV, as well as Ti K-edge XANES [12]. On the other hand, the first derivative reflects the electronic state and local symmetry around Cu [13]. The order of peak positions corresponding to the first derivatives is as follows; $Cu^0 < Cu^+ < Cu^{2+}$ (D_{4h}) $< Cu^{2+}$ (O_h) ≈ Cu^{2+} (T_d). In the case of 0.5 wt% Cu/Al_2O_3 pretreated under an O_2 stream at 773 K, a tiny preedge peak exists, and the intensity is larger than that of CuO but smaller than that of $Cu(OH)_2$. The first derivative spectrum shows two peaks, indicated by arrows. One is found for the spectrum of CuO and the other for that of $Cu(OH)_2$.

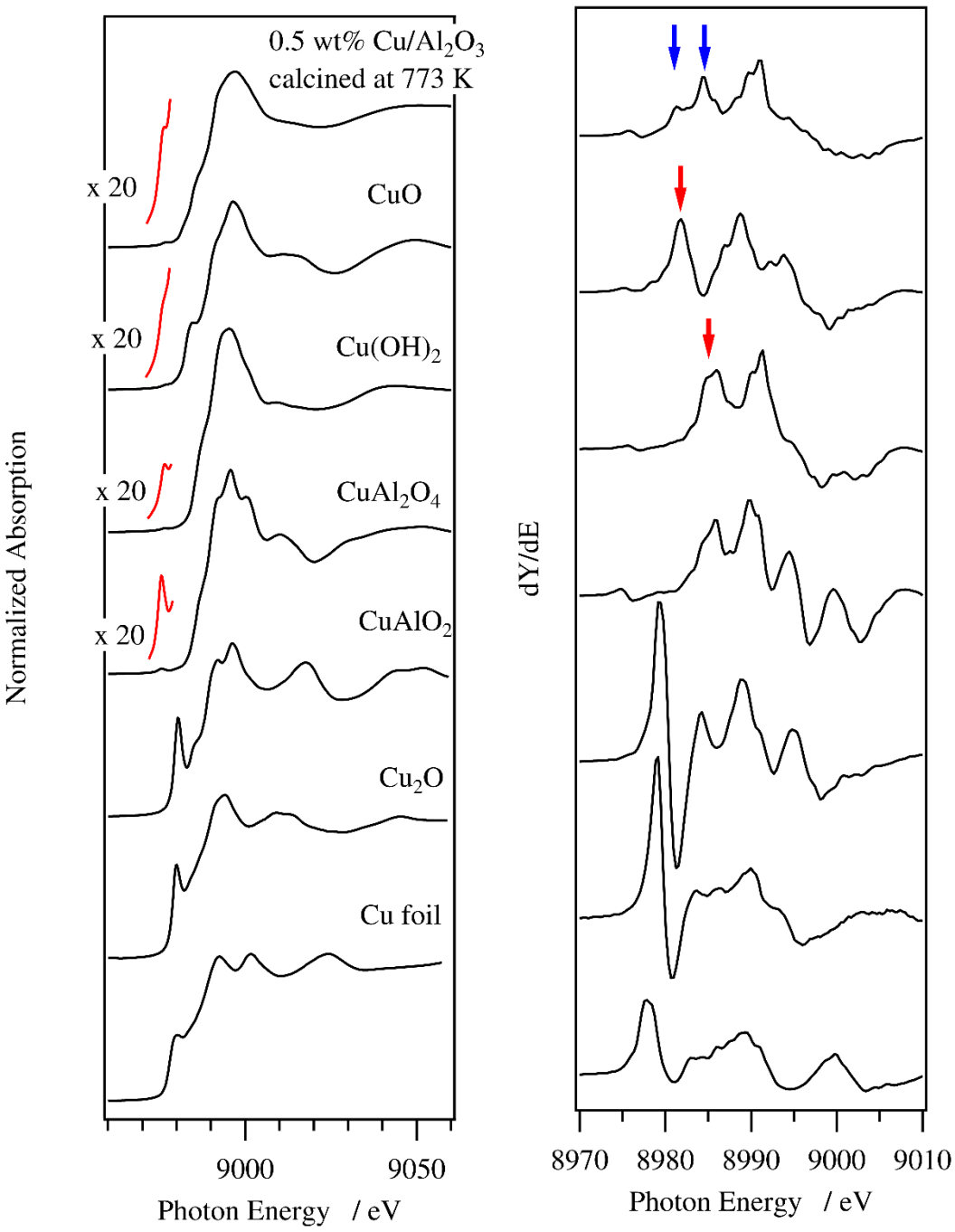

Figure 2. Cu K-edge XANES spectra and their first derivatives of 0.5 wt% Cu/Al_2O_3 calcined at 773 K and reference compounds.

On the basis of these results, the author concludes that Cu species on 0.5-Cu/Al_2O_3-773 consists of a mixture of divalent D_{4h}-like and distorted O_h species, and the distorted CuO_6 is predominant.

Figure 3 shows XANES spectra of Cu/Al_2O_3 catalysts after NO-CO-O_2 reaction. The edge energy and the existence of an *1s-3d* peak demonstrate that all of the Cu species remained divalent throughout the reaction. In the case of Cu/Al_2O_3-773 with various Cu loadings, XANES spectra are quite similar except for that of 10 wt% Cu/Al_2O_3. Although catalytic activity is significantly varied with Cu loadings from 0.5 to 5 wt%, coordination environments are not greatly different.

In the derivative spectra, the first peak around 8981 eV of reacted 0.5-Cu/Al_2O_3-773 is larger than that of the fresh catalyst, indicating that the O_h species was transferred to some extent into a D_{4h}-like species during an NO-CO-O_2 reaction. In the case of the catalyst calcined at 1073 K, a remarkable difference was not observed among 0.5 - 3 wt% catalysts. It should be noted that the *1s-3d* transition peak of 5-Cu/Al_2O_3-1073 is larger than that of 5-Cu/Al_2O_3-773. This feature is clearly shown in the case of 10 wt% Cu/Al_2O_3. Enhancement of the pre-edge peak intensity by calcination at 1073 K corresponds to the formation of T_d species, *i.e.*, a $CuAl_2O_4$ spinel [3,4,14,15]. Furthermore, the peak energy positions of 5- and 10-Cu/Al_2O_3-1073 are lower than those of the original samples by 0.4 and 0.9 eV, respectively. Because the peak intensities of the two samples are weaker than that of a crystalline $CuAl_2O_4$ spinel, the fractions of T_d species in the catalysts are lower than that of $CuAl_2O_4$ (66.5 %) [1,11].

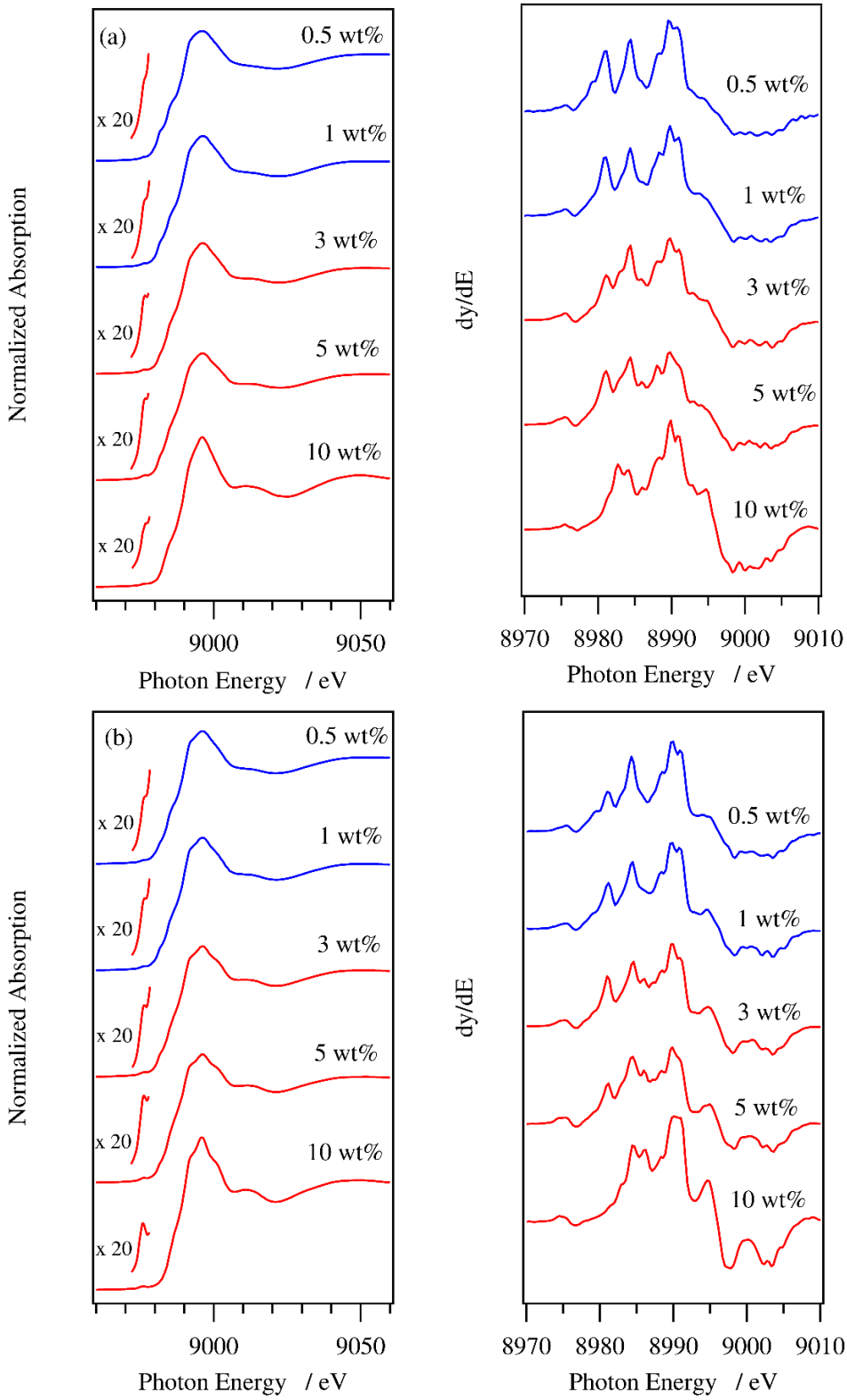

Figure 3. Cu K-edge XANES spectra and their first derivatives of Cu/Al_2O_3 after NO-CO-O_2 reaction at 773 K. Calcination temperatures: 773 K (a) and 1073 K (b).

3.2 EXAFS

Figure 4 shows k^3-weighted Cu K-edge EXAFS spectra and their Fourier transforms of a Cu/Al_2O_3 catalyst after NO-CO-O_2 reaction. As found in the XANES spectra, remarkable changes with Cu loadings were not observed when the loading was less than 5 wt%. A lack of peaks around 2.5 Å in a radial structure function (RSF) indicates that the supported species are in a highly dispersed form. The EXAFS spectrum of 0.5-Cu/Al_2O_3-1073 is similar to that of 0.5-Cu/Al_2O_3-773, but that of 10-Cu/Al_2O_3-1073 resembles that of $CuAl_2O_4$.

The feature of the EXAFS spectrum for the samples calcined at 1073 K gradually changes with the loading amount into that of $CuAl_2O_4$, and the characteristic change is clearly seen around 5-7 $Å^{-1}$. This indicates that Cu species was transformed to some extent into $CuAl_2O_4$ by calcination at 1073 K, the fraction of which increases with the loading amount.

Table 1 shows the results of curved-fitting analysis for the first coordination sphere. The two oxygen atoms along the *Z*-axis for CuO and $Cu(OH)_2$ are elongated by the Jahn-Teller effect, in comparison with the other four oxygen atoms on the *XY*-plane. The curve-fitting analysis reflects only four oxygen atoms at *XY*-plane, and the two residual atoms are not confirmed because of their long bond-length and the large Debye-Waller factor. The $CuAl_2O_4$ used in the present study consists of 66.5 % T_d and 33.5 % O_h Cu^{2+} species [1,11]. However, the obtained EXAFS parameters are not distinguishable from CuO and $Cu(OH)_2$, although the coordination environment is quite different. Therefore, curve-fitting analysis in this system is not very efficient.

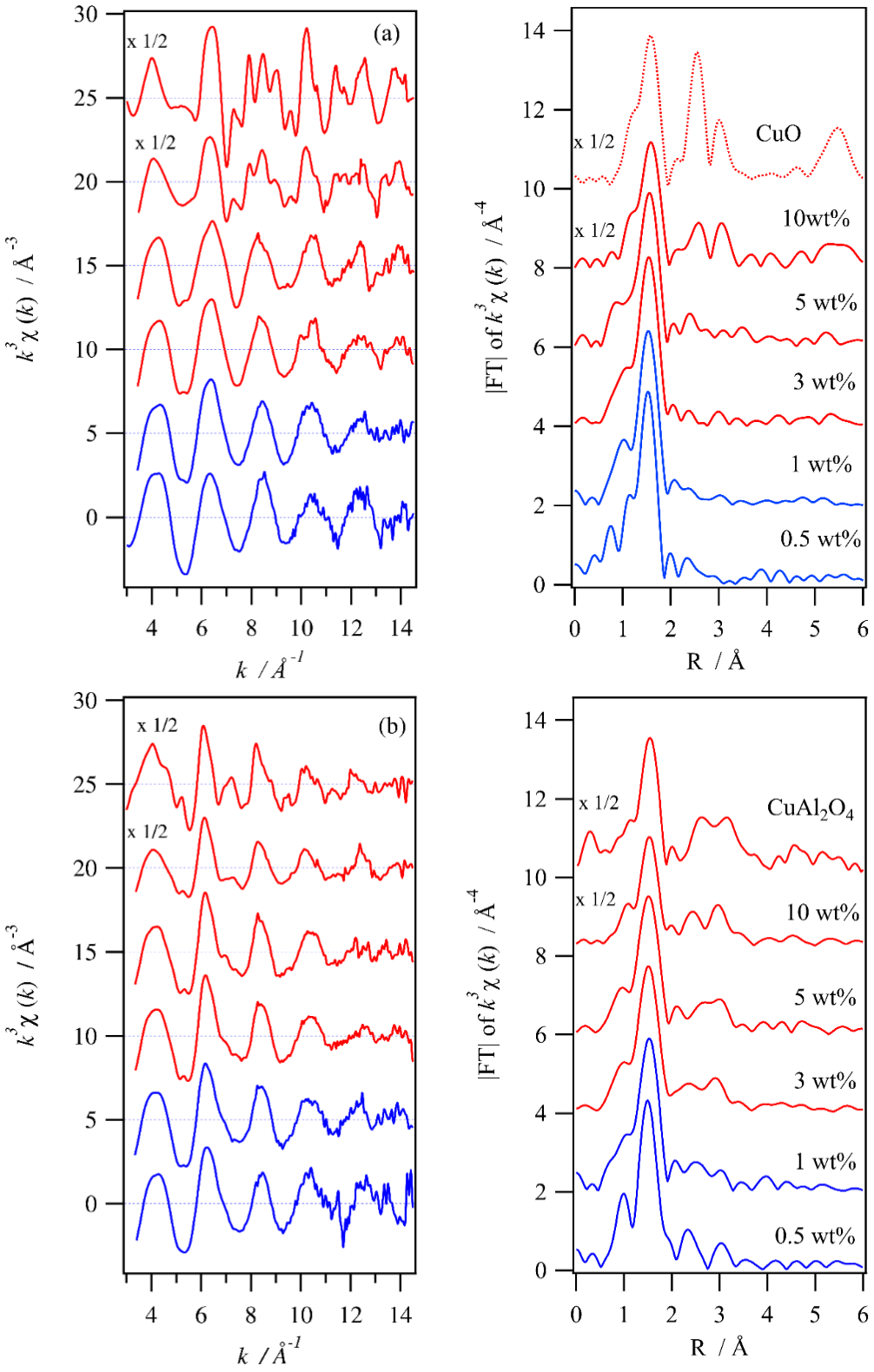

Figure 4. Cu K-edge EXAFS spectra and their Fourier transforms of Cu/Al_2O_3 after NO-CO-O_2 reaction at 773 K. Calcination temperatures: 773 K (a) and 1073 K (b).

Table 1

Results of curve-fitting analysis of Cu/Al_2O_3 after NO-CO-O_2 reaction at 773 K. [a]

Sample	CN [b]	r / Å [c]	$\Delta\sigma^2$ / Å^2 [d]	R (%) [e]
CuO	4.6(1)	1.95(0)	-0.0017(2)	8.6
	[4] [f]	[1.96] [f]		
	[2] [f]	[2.78] [f]		
$Cu(OH)_2$	4.5(1)	1.95(0)	-0.0009(2)	12.2
	[4] [f]	[1.94] [f]		
	[2] [f]	[2.63] [f]		
Cu_2O	2.2(0)	1.86(0)	-0.0028(1)	8.4
	[2] [f]	[1.84] [f]		
$CuAl_2O_4$	5.3(1)	1.95(0)	0.0017(2)	4.9
calcined at 773 K				
0.5 wt% [g]	3.3(0)	1.94(0)	0.0001(1)	6.4
0.5 wt%	3.6(1)	1.93(0)	0.0009(1)	9.6
1 wt%	3.1(0)	1.94(0)	-0.0003(1)	8.3
3 wt%	3.0(0)	1.95(0)	-0.0003(1)	7.5
5 wt%	2.9(0)	1.95(0)	-0.0002(1)	9.0
10 wt%	4.2(1)	1.96(0)	-0.0010(2)	9.8
calcined at 1073 K				
0.5 wt%	3.1(1)	1.93(0)	0.0003(2)	11.5
1 wt%	3.2(0)	1.95(0)	0.0010(1)	6.8
3 wt%	3.0(0)	1.94(0)	0.0011(0)	6.9
5 wt%	2.9(0)	1.94(0)	0.0010(1)	6.9
10 wt%	3.9(1)	1.95(0)	0.0001(1)	8.4

[a] Inverse-Fourier range, Δ R = 1.0 - 1.9 Å; fitting range, Δk = 4.0 - 12.0 Å^{-1}.

[b] Coordination number.

[c] Interatomic distance.

[d] Relative Debye-Waller factor against that of reference compounds (NiO).

[e] $\sqrt{\Sigma\left(k^3\chi_{experimental} - k^3\chi_{calculated}\right)^2 / \Sigma\left(k^3\chi^2_{experimental}\right)^2} \times 100.$

[f] Crystallographic data [10].

[g] Fresh catalyst.

In fact, estimated EXAFS parameters of all of the Cu/Al_2O_3 catalysts lie in experimental errors, despite their quite different loading amounts and calcination temperatures. Combining with XANES characterizations, the author concludes that Cu species on γ-Al_2O_3 are present as a mixture of CuO- and $Cu(OH)_2$-like CuO_6 units and that the two axial Cu-O bonds are much longer than the four equatorial bonds. The Cu species may be located at the octahedral site on the oxygen layer parallel to the (110) plane [16,17] with cubic close-packing lattice oxygen of γ-Al_2O_3.

3.3 UV/VIS/NIR

Figure 5 shows UV/VIS/NIR spectra of Cu/Al_2O_3. All of the catalysts calcined at 773 K exhibit two absorption bands around 40000 and 13000 cm^{-1}, assignable to *LMCT* (ligand-to-metal charge transfer) transition in divalent O_h species [*LMCT*(O_h)] and *d-d* transition of Cu^{2+} [*d-d*(O_h)] species, respectively [1]. Two additional bands appear around 21000 and 7000 cm^{-1} after calcination at 1073 K. The former is due to *LMCT* transition of T_d species [*LMCT*(T_d)] [18], and the latter is due to *d-d* transition of T_d species [*d-d*(T_d)] [4,14,15]. This result shows that the calcination procedure at 1073 K brings about the formation of T_d species, which is a component of the $CuAl_2O_4$ spinel [2,4,14,15]. No bands due to T_d species were observed in the 0.5-Cu/Al_2O_3-1073 spectrum, but the relative intensity of T_d to O_h species increases with increasing loading amount. The same phenomena have been pointed out in a $Cu–Al_2O_3$ system calcined at 1073 K. Shimizu *et al.* estimated the fraction of the T_d/O_h of Cu^{2+} species by deconvolution analysis of Cu L_3-edge XANES, and they concluded that O_h species were the main component at a lower concentration and that the fraction of T_d species increased as the Cu concentration increased [4]. They claimed that Cu^{2+} species preferentially occupied vacant O_h sites on Al_2O_3, followed by allocation at the T_d sites. However, their assumption could not explain

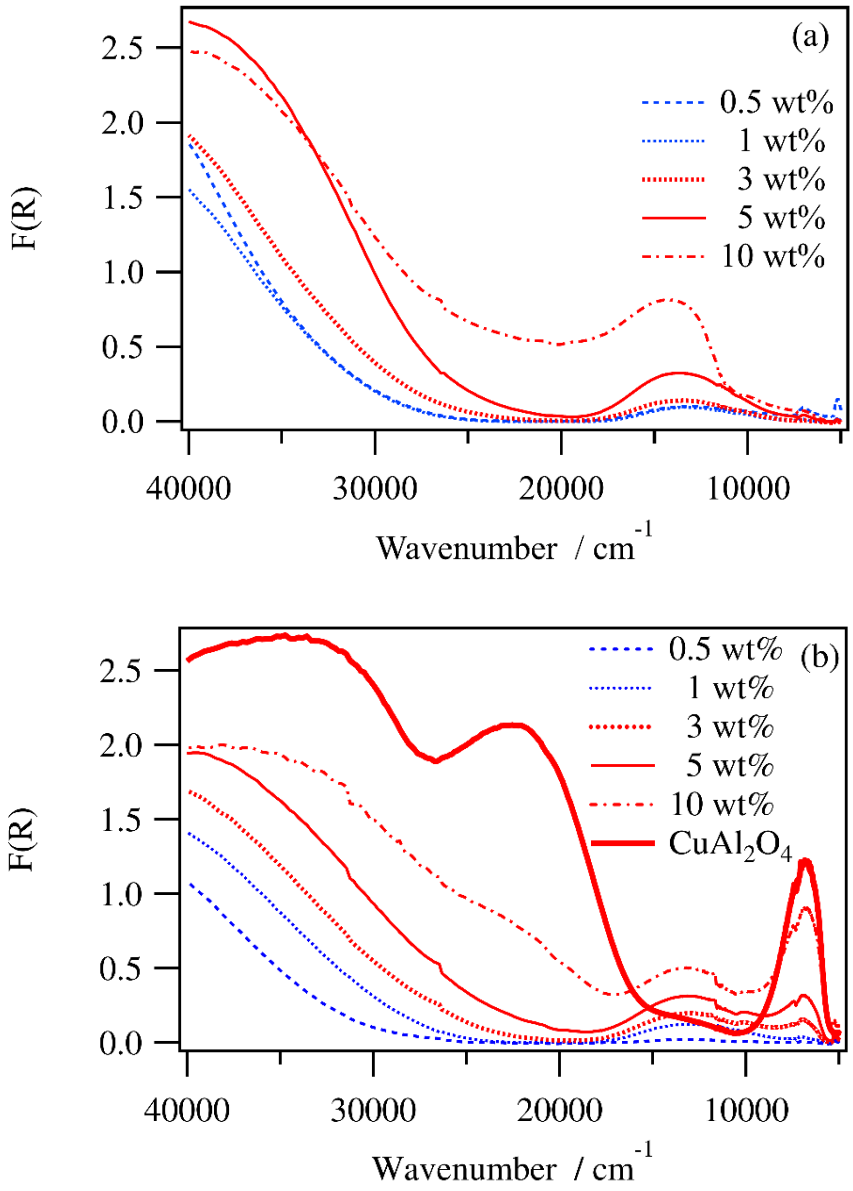

Figure 5. UV/VIS/NIR spectra of Cu/Al_2O_3 calcined at 773 K (a) and 1073 K (b).

a lack of T_d species in samples calcined at 773 K.

As shown in Figure 5, the T_d/O_h ratios of all of the catalyst samples were smaller than that of $CuAl_2O_4$. A $CuAl_2O_4$ spinel is thermodynamically stable under air in the temperature range of 885 to 1444 K [19]. The author assumes that only a limited part of Cu species is present as a $CuAl_2O_4$ spinel and the residues remain as to O_h species. Here, the author proposes that only aggregated Cu species on Cu/Al_2O_3-773 are transformed into $CuAl_2O_4$ by calcination at 1073 K and that isolated Cu species remains as the original structure throughout the calcination procedure.

This is justified by the result that 0.5-Cu/Al_2O_3-773 on which isolated Cu species are dominant exhibits no change in UV/VIS/NIR or XANES by calcination. In general, binary metal oxide synthesis via a solid phase reaction is carried out just below the melting point of the target compound, while the present calcination temperature (1073 K) was much lower than the decomposition temperature of $CuAl_2O_4$ (1444 K). Therefore, it is likely that all of the Cu species on Al_2O_3 do not always form into $CuAl_2O_4$ by calcination at 1073 K. In fact, the author confirmed that formation of $LaAlO_3$ perovskite on La/Al_2O_3 by calcination at 1273 K requires a certain concentration of La atoms above 0.5 mmol per gram of Al_2O_3 [20]. Then, the fraction of aggregated Cu^{2+} species on Cu/Al_2O_3 was estimated by deconvolution analysis of UV/VIS/NIR spectra on the basis of the five following assumptions: (1) an UV/VIS/NIR spectrum consists of four bands, *LMCT*(O_h), *LMCT*(T_d), *d-d*(O_h) and *d-d*(T_d); (2) the absorption coefficient ratio of *d-d*(T_d) to *d-d*(O_h) can be calculated from the corresponding band areas of $CuAl_2O_4$; (3) absorption coefficients of *d-d* transitions for $CuAl_2O_4$ and Cu/Al_2O_3 are identical.; (4) at a calcination temperature of 1073 K, only aggregated Cu species are transformed into a $CuAl_2O_4$ spinel; and (5) the T_d/O_h ratio in any spinel is equal to the thermodynamically equilibrium value (66.5/33.5 at 1273 K; 67.5/32.5 at 1073 K) [11].

First, the author deconvoluted UV/VIS/NIR spectra of $CuAl_2O_4$ (Figure 6) and then estimated the site ratio of T_d/O_h and aggregated species. The results are summarized in Table 2. Although a crystalline CuO phase was detected with XRD characterization on 10-Cu/Al_2O_3-773, the fraction of aggregates was only 28 %. Aggregated species increased with the loading amount. This tendency has been pointed out from ESR characterization [1,21], but quantitative determination of the fraction had not been carried out. An XAFS spectrum reflects the averaged information of the target element.

If an aggregated species is a minority on a catalyst surface, EXAFS analysis should lead to the conclusion that all of the supported species are in a highly dispersed form. The author notes that an aggregated Cu species is not always present as large CuO crystallite. Therefore, XRD and XAFS characterizations could not distinguish the state of loaded Cu species among 0.5 - 5 wt%.

3.4 Active Species for NO-CO-O_2 *Reaction*

All of the catalysts calcined at 1073 K exhibited lower activities than did the corresponding catalysts calcined at 773 K, as shown in Figure 1. This shows that $CuAl_2O_4$ is not effective for NO-CO-O_2 reaction, in contrast to the case of the NO-C_3H_6-O_2 system [3,4]. The coordination environments of Cu species on Cu/Al_2O_3-773 are almost identical regardless of the loading. The definitive difference among various loadings is the presence of aggregated species. In the case of a loading amount of less than 1 wt%, almost all of the Cu species are isolated. The most active catalyst of 0.5-Cu/Al_2O_3 consists of isolated Cu^{2+} species only. However, the lower active catalyst of 3-Cu/Al_2O_3 contains 8 % aggregated species. It has been reported that the turnover frequency of Cu species on Al_2O_3 for CO oxidation drastically increased with loading amount [21].

Table 2

The fractions of tetrahedral species and aggregated species.

Catalyst	A(T_d/O_h) [a]	fr(T_d) (%) [b]	Aggr. (%) [c]
$CuAl_2O_4$	4.72	(66.5)	-
0.5 wt%	0	0	0
1 wt%	0.05	1.9	2.8
3 wt%	0.14	5.4	8.0
5 wt%	0.30	11.2	16.6
10 wt%	0.56	19.2	28.4

[a] Band area ratio of *d-d* transitions in an UV/VIS/NIR spectrum of Cu/Al_2O_3 calcined at 1073 K.

[b] Fraction of T_d species [= A(T_d/O_h)/4.72 x 66.5]

[c] Fraction of aggregated species [= fr(T_d)/67.5 x 100]

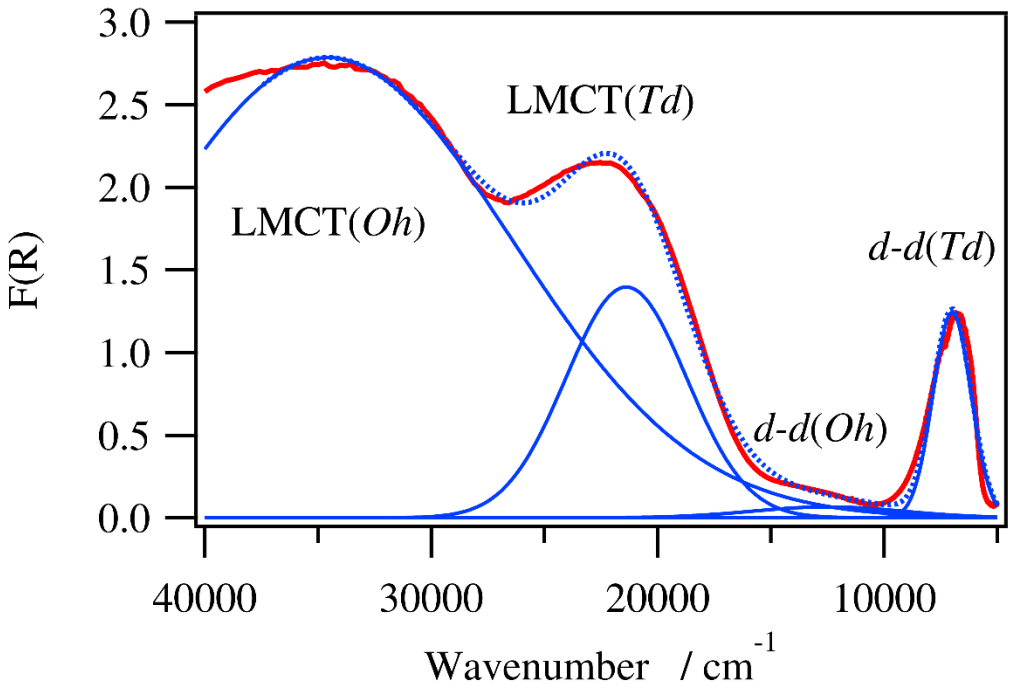

Figure 6. UV/VIS/NIR spectrum of $CuAl_2O_4$ and deconvoluted spectra.

As shown in Figure 1, it is obvious that the existence of aggregated Cu species lowers activities for the NO-CO-O_2 reaction because of the high activity for CO oxidation. The author concludes that the active sites are isolated distorted CuO_6 species supported on Al_2O_3.

4. Conclusions

Cu species on Cu/Al_2O_3 (0.5-10 wt%) calcined at 773 K are a mixture of D_{4h}-like and distorted CuO_6 species. Only aggregated species is transformed into $CuAl_2O_4$ by calcination at 1073 K. In the case of a loading amount of more than 3 wt%, most of the supported Cu species is in a highly dispersed form, but the residues are aggregates. The active sites for the NO-CO-O_2 reaction are the isolated Cu^{2+} species supported on γ-Al_2O_3, and coexistence of aggregated species drastically reduces the activity of NO reduction.

References

[1] T. Yamamoto, T. Tanaka, R. Kuma, S. Suzuki, F. Amano, Y. Shimooka, Y. Kohno, T. Funabiki, S. Yoshida, *Phys. Chem. Chem. Phys.* **2002**, *4*, 2449–2458.

[2] F. Amano, S. Suzuki, T. Yamamoto, T. Tanaka, *Appl. Catal. B Environ.* **2006**, *64*, 282–289.

[3] K. Shimizu, H. Maeshima, A. Satsuma, T. Hattori, *Appl. Catal. B Environ.* **1998**, *18*, 163–170.

[4] K. Shimizu, H. Maeshima, H. Yoshida, A. Satsuma, T. Hattori, *Phys. Chem. Chem. Phys.* **2000**, *2*, 2435–2439.

[5] T. Tanaka, H. Yamashita, R. Tsuchitani, T. Funabiki, S. Yoshida, *J. Chem. Soc.*

Faraday Trans. 1 Phys. Chem. Condens. Phases **1988**, *84*, 2987.

[6] L. S. Kau, D. J. Spira-Solomon, J. E. Penner-Hahn, K. O. Hodgson, E. I. Solomon, *J. Am. Chem. Soc.* **1987**, *109*, 6433–6442.

[7] N. Kosugi, H. Kondoh, H. Tajima, H. Kuroda, *Chem. Phys.* **1989**, *135*, 149–160.

[8] N. Kosugi, Y. Tokura, H. Takagi, S. Uchida, *Phys. Rev. B* **1990**, *41*, 131–137.

[9] J. C. J. Bart, **1986**, pp. 203–296.

[10] A. F. Wells, *Structural Inorganic Chemistry* (Calarendon Press, Oxford, **1975).**

[11] R. F. Cooley, J. S. Reed, *J. Am. Ceram. Soc.* **1972**, *55*, 395–398.

[12] F. Farges, G. E. Brown, J. J. Rehr, *Phys. Rev. B* **1997**, *56*, 1809–1819.

[13] Y. Okamoto, T. Kubota, H. Gotoh, Y. Ohto, H. Aritani, T. Tanaka, S. Yoshida, *J. Chem. Soc. Faraday Trans.* **1998**, *94*, 3743–3752.

[14] R. Friedman, J. Freeman, F. W. Lytle, *J. Catal.* **1978**, *55*, 10–28.

[15] M. C. Marion, E. Garbowski, M. Primet, *J. Chem. Soc. Faraday Trans.* **1990**, *86*, 3027.

[16] B. C. Lippens, J. H. de Boer, *Acta Crystallogr.* **1964**, *17*, 1312–1321.

[17] B. C. Lippens, J. J. Steggerda, *Physical and Chemical Aspects of Adsorbents and Catalysts,* Ed. B.G. Linsen (Academic Press, London, **1970).**

[18] Y. Teraoka, C. Tai, H. Furukawa, S. Kagawa, K. Asakura, Y. Iwasawa, *Shokubai* **1990**, *32*, 426.

[19] K. T. Jacob, C. B. Alcock, *J. Am. Ceram. Soc.* **1975**, *58*, 192–195.

[20] T. Yamamoto, T. Tanaka, T. Matsuyama, T. Funabiki, S. Yoshida, *J. Synchr. Rad.* **2001**, *8*, 634–636.

[21] P. W. Park, J. S. Ledford, *Appl. Catal. B Environ.* **1998**, *15*, 221–231.

Chapter 3

Effect of Molybdenum on the Structure and Performance of $V_2O_5/TiO_2–SiO_2–MoO_3$ Catalysts for the Oxidative Degradation of *o*-Chlorotoluene

Abstract

$V/TiO_2–SiO_2–MoO_3$ (TSM) catalysts exhibit enhanced redox capabilities, but the role of each species in the mixed oxide support is not well understood. Herein, the physicochemical characteristics of molybdenum oxide in TSM were investigated using X-ray diffraction, X-ray photoelectron spectroscopy, and X-ray absorption fine structure spectroscopy, and the performance of V/TSM catalysts for the oxidative decomposition of *o*-chlorotoluene was examined. The V/TSM catalysts exhibited superior performances in this decomposition reaction at low temperatures. The molybdenum species were highly dispersed as Mo^{6+}, replacing Ti^{4+} in the anatase TiO_2 framework and forming a solid solution. The redox capability of the vanadium species in the catalyst was enhanced by electron transfer from the TSM support to vanadium, likely due to the coexistence of Mo^{6+} and Ti^{4+} in the TSM solid solution, which has a unique structure. These results are expected to contribute to enhancing the abatement of dioxins at low temperatures.

1. Introduction

Flue gases from municipal waste incineration processes commonly contain harmful NO_x gases (NO, NO_2) and toxic dioxins, such as polychlorinated dibenzo-*p*-dioxins and polychlorinated dibenzofurans. As such, the catalytic degradation of these pollutants has been intensively investigated, with the decomposition of NO_x and NH_3 being commonly carried out industrially over selective catalytic reduction (SCR) catalysts such as V_2O_5/TiO_2 [1–6]. As V_2O_5/TiO_2 catalysts are also capable of decomposing dioxins, they have been applied for the simultaneous abatement of NO_x and dioxins discharged from municipal waste incinerators [7–15]. Generally, an electrostatic precipitator or a fabric filter is used for such processes (Figure 1), the latter of which is known to collect fly ash more effectively [16]. However, owing to the low heat resistance of fabric filters, the gas temperature should be lower than 150 °C in most cases. Subsequently, the outlet gas from the fabric filter requires reheating to a higher temperature to achieve the catalytic decomposition of both NO_x and dioxins. Although a higher catalytic activity can be achieved at higher temperatures, a large amount of energy is required for the reheating process.

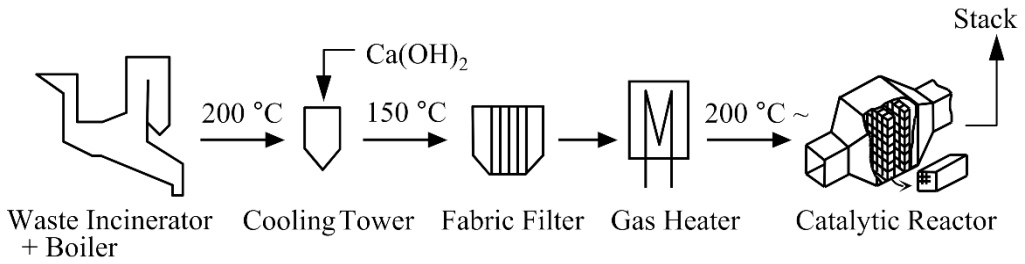

Figure 1. Catalytic dioxins decomposition process in municipal waste incineration plants.

Highly active catalysts are therefore necessary for low-temperature dioxins decomposition and in particular for the fabric filter process. Nevertheless, few reports exist concerning the catalytic decomposition of dioxins at temperatures lower than 200 °C. Although WO_3 or MoO_3 has conventionally been added to promote the activity and SO_2 durability of V_2O_5/TiO_2 catalysts [7,8,10,12], these catalysts require temperatures higher than 250 °C to realize satisfactory dioxins decomposition efficiencies.

In this context, the author previously developed a $V_2O_5/TiO_2–SiO_2–MoO_3$ (V/TSM) catalyst with high activity for low-temperature NH_3-SCR [17]. The mixed oxide support material of this catalyst, TSM, was prepared via a coprecipitation method. As the activity of the V/TSM catalyst was found to be enhanced by its redox capability, the activity would be expected to be improved for the oxidative decomposition of dioxins. However, the role of the TSM support material and the mechanism of redox enhancement require clarification to allow optimization of its composition to obtain a superior catalytic performance.

Thus, the author herein reports the study into the physicochemical characteristics of molybdenum oxide in V/TSM catalysts. Catalytic activity tests were carried out using *o*-chlorotoluene as a substitute for dioxins due to the high toxicity of dioxins and the similar decomposition behavior of *o*-chlorotoluene [18]. The structure–activity relationships for the V/TSM catalysts were investigated using Mo K-edge X-ray absorption near-edge structure (XANES) and X-ray absorption fine structure (EXAFS) spectroscopy. XANES spectroscopy provides information regarding the local geometry around the absorbing atom and its oxidation state, whereas EXAFS spectroscopy is a powerful technique for obtaining direct structural information.

2. Experimental

2.1. Catalyst preparation

TSM mixed oxides were prepared by a coprecipitation method, as described in the author's previous report [17], using titanium sulfate solution (70 g/L TiO_2, Tayca Corp.), silica sol (30% SiO_2, Nissan Chemical Corp.), ammonium molybdate (Taiyo Koko Co., Ltd.). TiO_2–SiO_2 (TS) and TiO_2 were prepared similarly. The SiO_2 content in all TS and TSM samples was fixed to 7 wt%.

For comparison, MoO_3/TS (Mo/TS) and MoO_3/TiO_2 (Mo/TiO_2) were prepared by an incipient wetness method. Ammonium molybdate (1.36 g) was mixed with monoethanol amine (0.55 g, Nippon Shokubai) and deionized water (5 g) at approximately 25 °C, and then the TS or TiO_2 powders (10 g) were impregnated with this molybdenum solution and mixed well. The conditions and procedure for drying and calcination were the same as those employed for the TSM samples. The nomenclature used for the various samples is "XMo/TiO_2", "XMo/TS", and "XTSM", where X represents the molybdenum content calculated as the weight percentage of MoO_3. The molybdenum content in TSM ranged between 5 and to 30 wt%, and those in Mo/TS and Mo/TiO_2 were 10 or 30 wt%. Honeycomb-shaped vanadium catalysts were prepared in accordance with the author's previous report [17]. Ammonium metavanadate was mixed with an aqueous solution of monoethanol amine and oxalic acid at approximately 25 °C. The TSM powders and the vanadium solution obtained above were mixed and kneaded under the continuous addition of water. The resultant blend was fed into an extrusion molding device and molded into a honeycomb monolith. After drying at 60 °C and then calcining at 450 °C for 5 h in air, a honeycomb catalyst with an outer diameter of 50 mm and a pitch of 3.2 mm was obtained.

V_2O_5–MoO_3/TiO_2–SiO_2 (V10Mo/TS) and V_2O_5–MoO_3/TiO_2 (V10Mo/TiO_2) were also prepared by the same method, with ammonium molybdate added to the mixed aqueous solution of ammonium metavanadate, monoethanol amine, and oxalic acid. V_2O_5/TiO_2–SiO_2 (V/TS) was prepared by the same method as V10Mo/TS, except that no ammonium molybdate was added. The loading amount of vanadium on all the catalysts in the present study was fixed at 8 wt% V_2O_5.

2.2. Characterization of the catalysts

The X-ray diffraction (XRD) measurements of the support materials and catalysts were carried out using a Rigaku SmartLab diffractometer with a CuKα radiation source under ambient conditions. The specific surface areas of the samples were evaluated by the Brunauer–Emmett–Teller (BET) method using a Mountech Macsorb Model 1210 apparatus. The samples were degassed in flowing N_2 at 200 °C for 60 min.

X-ray photoelectron spectroscopy (XPS) spectra were obtained using a ULVAC PHI Quantera SXM instrument. The sample powders were fixed on double-sided carbon tape on an Al stub. The spectra were recorded at 25 °C under a pressure of $<1.33 \times 10^{-6}$ Pa using an AlKα radiation source with a beam diameter of 100 μm and a pass energy of 140 eV. The binding energies were calibrated to the C1s peak.

The V K-edge XANES measurements were performed at the BL-9C beamline of the Photon Factory (KEK-PF). The sample masses were calculated to adjust the height of edge jump and mixed with boron nitride (catalyst sample:boron nitride = 1:11) before being pressed into an in situ cell to form a self-supporting disc with a diameter of 7 mm. Nitrogen gas was fed into the in situ cell and the data were collected in transmission mode using a Si(1 1 1) monochromator at ambient temperature (25 °C) or at 200 °C. The XANES spectra were analyzed with the ATHENA software.

The Mo K-edge XAFS measurements were carried out at the BL01B1 beamline of SPring-8 (Japan Synchrotron Radiation Research Institute) in transmission mode. A double-crystal Si(1 1 1) monochromator was used. The sample masses were calculated to adjust the height of edge jump and mixed with boron nitride (catalyst sample:boron nitride = 2:1). The Ti K-edge XAFS measurements were performed at the BL-9C beamline of the KEK-PF using a Si(1 1 1) monochromator. The samples were mixed with boron nitride at a sample:boron nitride ratio of 1:3. For the Mo and Ti K-edge XAFS measurements, each sample mixed with boron nitride was pressed to form a self-supporting disc with a diameter of 10 mm, and the XAFS spectra were recorded at ambient temperature (25 °C) and pressure. The Mo and Ti K-edge XAFS data were analyzed using the REX2000 software (Rigaku Co.).

The V, Mo and Ti K-edge XANES spectra were normalized to the edge jump, and the first derivative of the near-edge region was employed for determination of the edge absorption energy. The k^3-weighted EXAFS oscillations of the Mo and Ti K-edges were extracted using spline smoothing. Subsequently, the filtered k^3-weighted $\chi(k)$ was Fourier transformed into R space (k range: 3–13 $Å^{-1}$) using a Hanning function window [19].

2.3. Catalytic activity measurements

Oxidative degradation tests using *o*-chlorotoluene were conducted in a U-shaped tubular stainless-steel reactor with an inner diameter of 3.8 cm. The honeycomb catalyst to be tested was cut into 25 cells and loaded into the reactor. A reaction gas mixture consisting of 100 ppm *o*-chlorotoluene, 10% O_2, and 10% H_2O by volume and balanced with N_2 was supplied to the reactor. *o*-Chlorotoluene and H_2O were supplied using two glass saturators controlled at 31 °C for *o*-chlorotoluene and 46 °C for H_2O. The reaction gas flow rate was 0.6 Nm^3/h and the gas hourly space velocity (GHSV) was 6,000 h^{-1}.

The reaction was carried out overnight (~15 h) at each temperature, and the *o*-chlorotoluene concentrations before and after the reaction were analyzed by gas chromatography using a Shimadzu GC-14B instrument equipped with a Chromosorb column controlled at 140 °C. The concentrations were analyzed 3–5 times every 20 min, and after confirming the value to be almost constant, the average value was used for decomposition rate calculations. The CO and CO_2 concentrations in the gas were measured using a Horiba PG-250 gas analyzer.

3. Results

3.1. Characterization of the supports and catalysts

Table 1 summarizes the BET specific surface areas of the support materials with various compositions and the corresponding V–Mo containing catalysts. TS and TSM were found to exhibit noticeably high specific surface areas (163 and 135 m^2/g, respectively) compared to TiO_2 (82 m^2/g), which was attributed to the presence of SiO_2 [3]. The surface areas of TS and 10TSM decreased when vanadium and/or molybdenum were added, but remained >100 m^2/g.

3.2. o-Chlorotoluene oxidation activity

The results of the *o*-chlorotoluene oxidation reaction over three types of V–Mo catalysts are shown in Figure 2. In the catalyst outlet gas, no organic compounds were detected with the exception of unreacted *o*-chlorotoluene, and it was confirmed that reacted *o*-chlorotoluene was converted to CO_2 by checking the carbon balance. The V/10TSM catalyst showed a significantly higher activity than the other two catalysts, especially at low temperatures.

Table 1

BET specific surface areas of the support materials and V–Mo catalysts

Sample	Composition	BET surface area / m^2/g
TiO_2	TiO_2 (anatase)	82
TS	93 wt% TiO_2–7 wt% SiO_2	163
30Mo/TiO_2	30 wt% MoO_3/TiO_2	55
30Mo/TS	30 wt% MoO_3/TS	102
10Mo/TiO_2	10 wt% MoO_3/TiO_2	64
10Mo/TS	10 wt% MoO_3/TS	124
30TSM	63 wt% TiO_2–7 wt% SiO_2–30 wt% MoO_3	115
20TSM	73 wt% TiO_2–7 wt% SiO_2–20 wt% MoO_3	122
10TSM	83 wt% TiO_2–7 wt% SiO_2–10 wt% MoO_3	135
V10Mo/TiO_2	8 wt% V_2O_5–10 wt% MoO_3/TiO_2	60
V10Mo/TS	8 wt% V_2O_5–10 wt% MoO_3/TS	111
V/10TSM	8 wt% V_2O_5/10TSM	101

Figure 3 shows the performance of the catalysts with 8 wt% vanadium supported on TSM containing different molybdenum contents, where the MoO_3 = 0 wt% data point corresponds to the performance of the V/TS catalyst. Notably, the catalytic activity is sharply enhanced upon the addition of 5 wt% molybdenum by the coprecipitation method. A gradual increase in catalytic activity is observed up to 10 wt%, but at higher molybdenum loadings, the activity decreases once again, thereby indicating that excess molybdenum inhibits the reactivity. Although the main active species in the *o*-chlorotoluene decomposition reaction is vanadium, it is clear that the activity strongly depends on the addition method and the amount of molybdenum.

3.3. XRD

The XRD patterns of the catalysts and the support materials are shown in Figure 4. In all samples, diffraction peaks ascribable to anatase TiO_2 (JCPDS: 00-021-1272) are observed. The XRD patterns of 30Mo/TiO_2 and 30Mo/TS display strong peaks assigned to α-MoO_3 (JCPDS: 00-005-0508), and weak peaks at the same positions are observed for 10Mo/TiO_2 and 10Mo/TS (inset, Figure 4). In contrast, the crystal phases of α-MoO_3 and V_2O_5 (JCPDS: 00-041-1426) are not detectable for the V10Mo/TiO_2 and V10Mo/TS catalysts. These observations suggest that the structure of molybdenum oxide is modified by interactions with vanadium in the V10Mo/TiO_2 and V10Mo/TS catalysts.

Furthermore, the XRD patterns of TSM display peaks ascribable to anatase TiO_2 but do not display peaks corresponding to molybdenum oxide, even at a MoO_3 content of 30 wt% (30TSM). These results imply that the molybdenum species are highly dispersed within the TSM support.

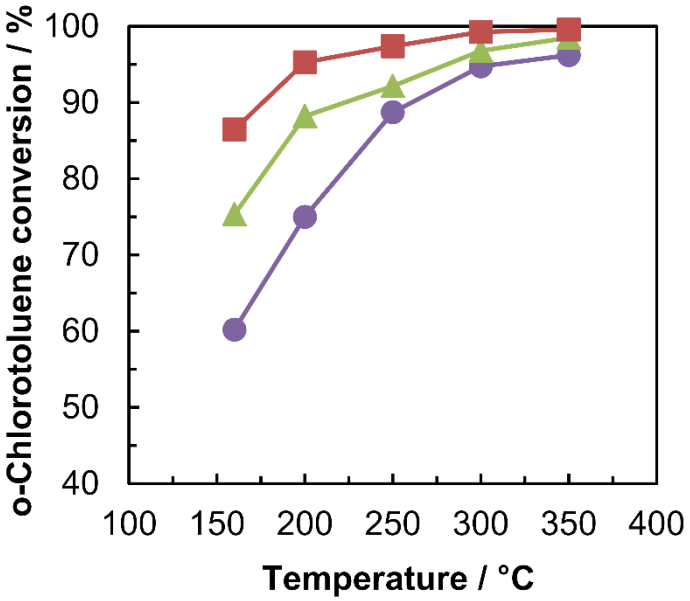

Figure 2. *o*-Chlorotoluene decomposition over V/10TSM (■), V10Mo/TS (▲), and V10Mo/TiO_2 (●). Reaction conditions: 100 ppm *o*-chlorotoluene, 10 vol% O_2, 10 vol% H_2O, N_2 balance; GHSV: 6,000 h^{-1}.

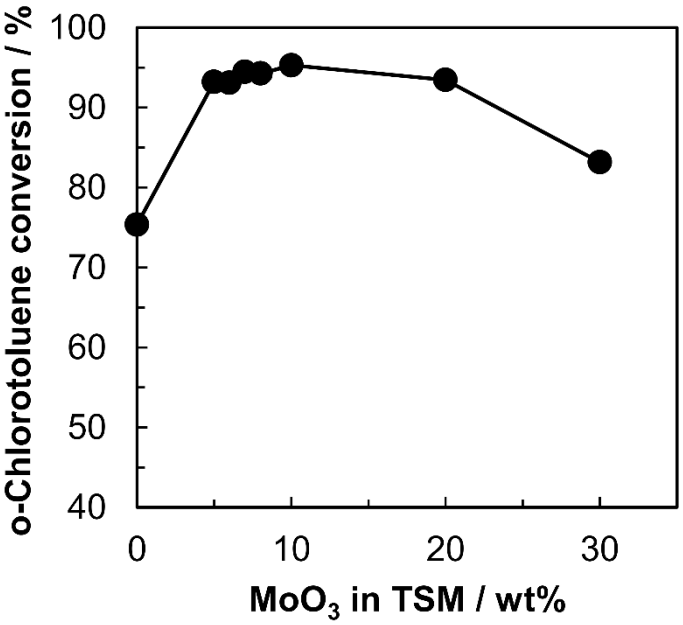

Figure 3. *o*-Chlorotoluene decomposition over V/TSM as a function of MoO_3 loading. The reaction temperature is 200 °C and all other conditions are as described for Figure 2.

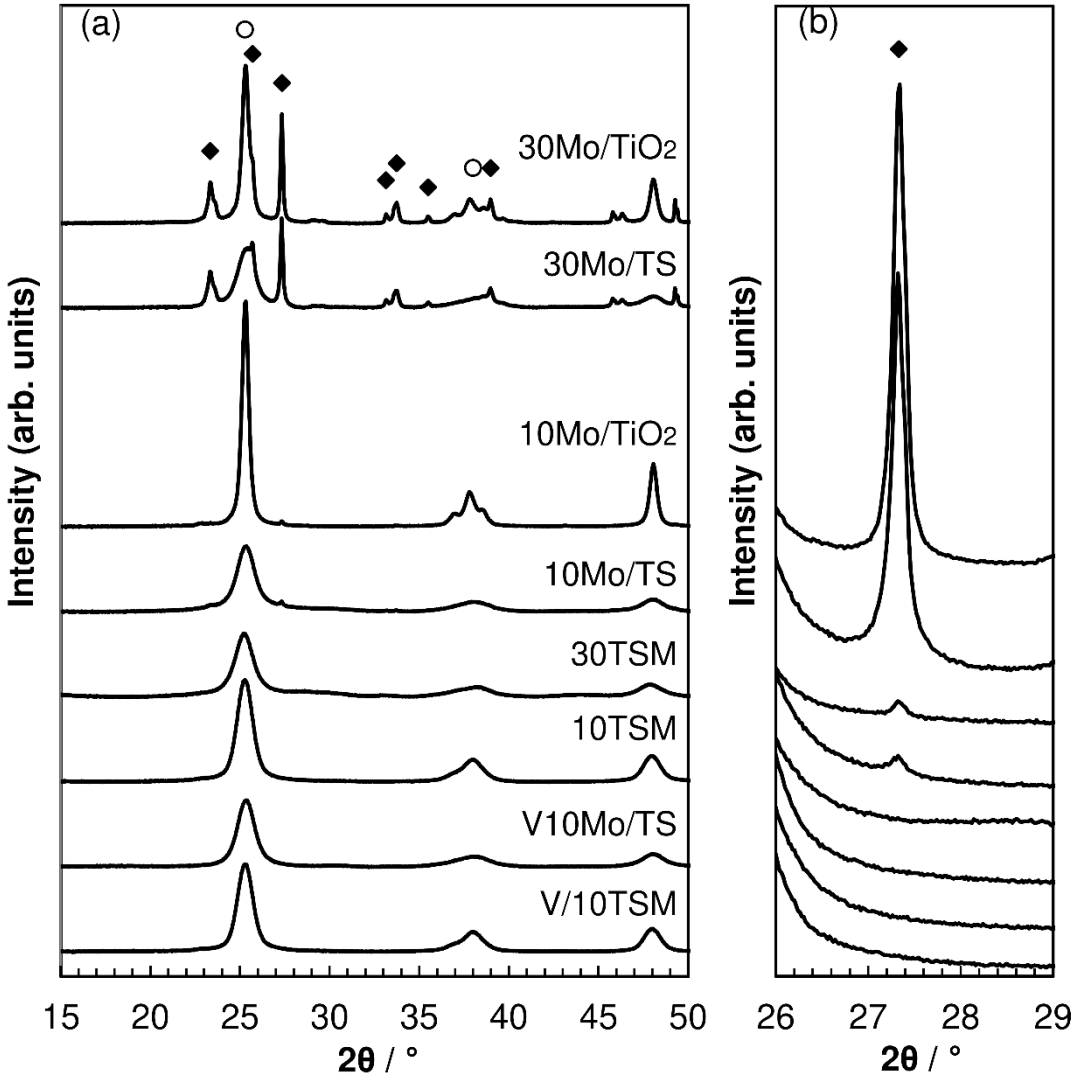

Figure 4. (a) XRD patterns of the Mo-containing catalysts, and (b) enlarged data in the region of 26–29°. Symbols: MoO_3 (◆); TiO_2 (○).

As shown in Figure 5, the diffraction peak observed at 2θ = 48° for 10Mo/TS is consistent with that assigned to the (2 0 0) plane of anatase TiO_2. A peak shift to lower diffraction angles is observed for TSM, with the extent of the shift increasing at higher molybdenum contents. The spacing between the (2 0 0) planes in the atomic lattice of 30TSM can be calculated as 1.900 Å (Table 2), which is clearly greater than that of anatase TiO_2 (1.892 Å).

3.4. XPS

The Mo-containing samples were characterized by XPS to investigate the properties of the surface molybdenum species (Figure 6). The binding energies for Mo3d (232.6 eV) and Ti2p (458.7 eV) were identical in all samples, indicating that the majority of molybdenum and titanium species on the surface are present as Mo^{6+} and Ti^{4+}. The XPS Mo3d peaks of 10Mo/TiO_2, 10Mo/TS and 10TSM, which are almost identical in shape, are broadened at lower binding energies compared to that of MoO_3. This broadening can be attributed to the presence of another type of molybdenum species or to electron transfer between molybdenum and the support material [20]. These results indicate that the electronic features of the surface molybdenum species on 10TSM are similar to those on 10Mo/TiO_2 and 10Mo/TS.

The surface compositions of these samples calculated from the XPS peak areas are summarized in Table 3. The surface atomic ratio of Mo/Ti for 10TSM is lower than those for 10Mo/TiO_2 and 10Mo/TS, thereby indicating that the surface molybdenum density on TSM is lower than those on the other supports, which suggests that molybdenum is incorporated within the particles.

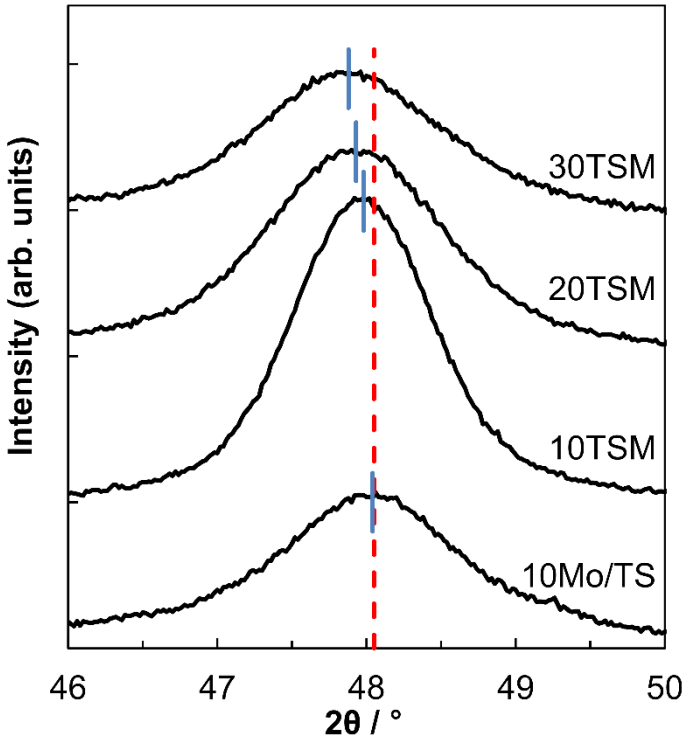

Figure 5. Enlarged XRD patterns of the 10Mo/TS and TSM samples. The peak maxima for these samples (solid blue lines) and anatase TiO_2 (JCPDS No. 00-021-1272, dotted red line) are indicated.

Table 2

XRD peak positions and interplanar distances of the (2 0 0) plane of anatase TiO_2

	2θ / °	Interplanar distance / Å
anatase TiO_2 (JCPDS)	48.05	1.892
10Mo/TS	48.04	1.894
10TSM	47.98	1.896
20TSM	47.92	1.898
30TSM	47.88	1.900

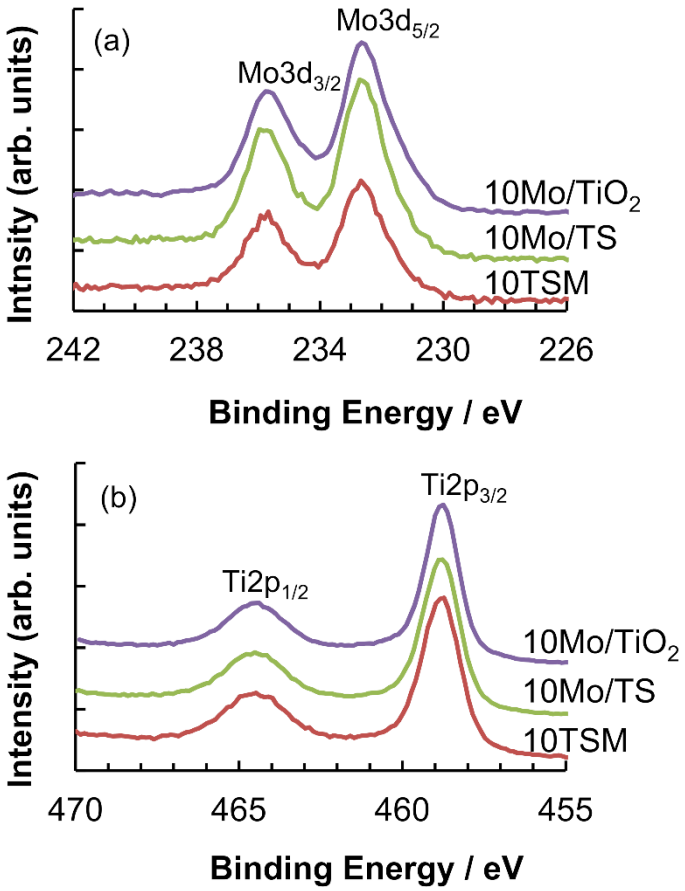

Figure 6. (a) Mo3d and (b) Ti2p XPS spectra of the Mo-containing samples, normalized to the intensity of $Ti2p_{2/3}$ for comparison of the Mo/Ti ratio.

Table 3

Surface atomic compositions and Mo/Ti ratios estimated by XPS

	Surface atomic composition / %				Mo/Ti
	Mo	Ti	Si	O	
$10Mo/TiO_2$	8.0	28.2	-	63.8	0.29
10Mo/TS	6.8	25.5	4.0	63.8	0.27
10TSM	4.6	27.0	5.8	62.6	0.17

3.5. V K-edge XANES spectroscopy

The V K-edge XANES spectra of the three vanadium catalysts as well as the V_2O_4 and V_2O_5 reference samples are presented in Figure 7. For all samples, pre-edge peaks are observed at approximately 5468 eV. These peaks are observable due to the 3d–4p orbital mixing of vanadium, which is induced by the distortion of VO_x from the octahedral VO_6 structure [21–23]. The pre-edge areas and main-edge positions are summarized in Table 4. As indicated, V_2O_5 displays a larger pre-edge area than V_2O_4, suggesting a distorted square-pyramidal structure around the vanadium atom in V_2O_5 [21–25]. The XANES spectra collected at 25 °C (thin line) and 200 °C (bold line) are identical for V_2O_4 and V_2O_5. In contrast, the pre-edge and main-edge positions of the three catalysts shift to lower photon energies after heating to 200 °C, accompanied by a decrease in the pre-edge area. These results suggest that vanadium oxide is reduced to a lower oxidation state owing to the desorption of surface oxygen, and thus the morphology around the vanadium atom is altered. A greater shift is observed in the main-edge position of V/10TSM than in those of V10Mo/TiO_2 and V10Mo/TS, indicating that the surface oxygen around vanadium is more easily desorbed over the V/10TSM catalyst. In other words, the reducibility of vanadium oxide is enhanced when supported on TSM.

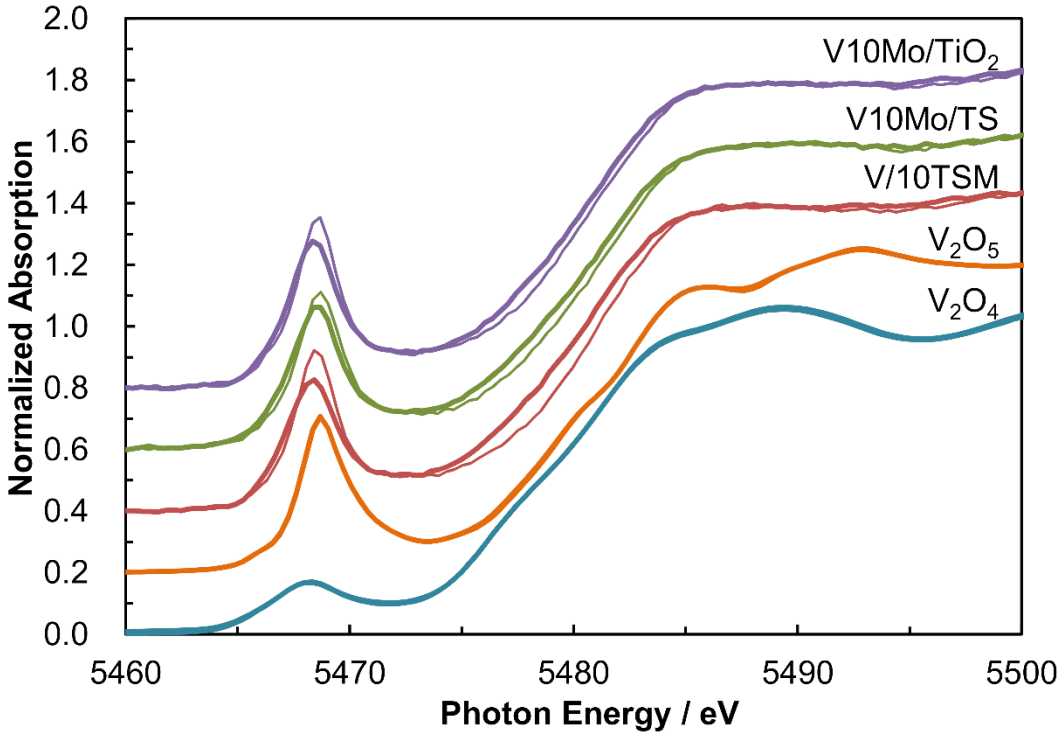

Figure 7. Normalized V K-edge XANES spectra of the V-containing catalysts and reference samples collected at 25 °C (thin lines) and 200 °C (bold lines) under flowing N_2.

Table 4

Pre-edge peak areas and main edge positions in the V K-edge XANES spectra

	Pre-edge peak area		Main-edge position / eV	
	25 °C	200 °C	25 °C	200 °C
V_2O_4	0.96	0.99	5478.6	5478.5
V_2O_5	1.73	1.76	5480.0	5480.1
V10Mo/TiO_2	1.81	1.75	5480.1	5479.7
V10Mo/TS	1.79	1.77	5480.1	5479.7
V/10TSM	1.74	1.65	5480.2	5479.5

3.6. Mo K-edge XANES spectroscopy

Figure 8 displays the Mo K-edge XANES spectra of the molybdenum-containing samples and the molybdenum reference compounds (MoO_2 and MoO_3). All samples with the exception of MoO_2 exhibit pre-edge peaks, which can be observed due to the d–p orbital hybridization caused by the distortion of the octahedral MoO_6 structure [26–29]. For a quantitative analysis, the ATHENA software was used to fit the XANES spectra in this region with a pseudo-Voigt function in combination with an error function (Figure 9). The absorption edge energies and pre-edge peak positions are the same as those of crystalline MoO_3, indicating that molybdenum is present as Mo^{6+}, regardless of the type of support, Mo loading amount, preparation method, or the presence of vanadium. Furthermore, 30Mo/TiO_2 and 30Mo/TS display similar pre-edge intensities to MoO_3, which has distorted octahedral symmetry [26] (magnified spectra in Figure 10). While 10Mo/TiO_2 and V10Mo/TiO_2 exhibit lower pre-edge intensities, 10Mo/TS demonstrates a higher pre-edge intensity than MoO_3. It has been reported that MoO_3/Al_2O_3 catalysts exhibit intense pre-edge peaks, indicating the presence of a monomeric molybdenum oxide species [28]. This species seems to be highly dispersed owing to the large specific surface area of the Al_2O_3 support. Therefore, the increased pre-edge intensity observed for 10Mo/TS can be attributed to the large specific surface area of the TS support, and it is likely that some molybdenum oxides on 10Mo/TS are present as monomeric species. In contrast, 30TSM demonstrates a lower pre-edge intensity than 10Mo/TiO_2, and the intensity decreases as the molybdenum content decreases. According to the XRD results (Figure 4), molybdenum atoms in TSM are more highly dispersed than those in Mo/TiO_2 and Mo/TS; however, monomeric molybdenum oxide species are not formed in the TSM samples, suggesting that the structure around molybdenum is less distorted.

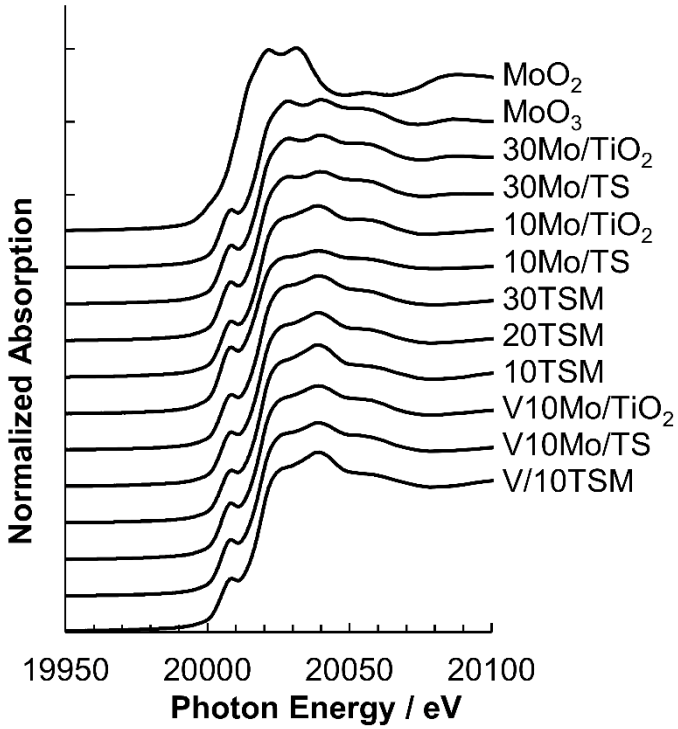

Figure 8. Normalized Mo K-edge XANES spectra of the Mo-containing catalysts and reference samples.

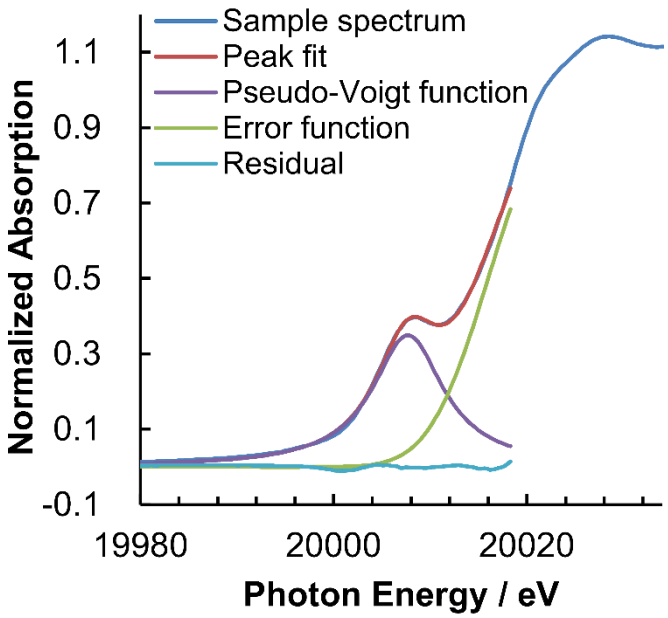

Figure 9. Pseudo-Voigt fitting result for the normalized Mo K-edge XANES spectrum of MoO_3.

The pre-edge intensity of the V10Mo/TS catalyst is clearly lower than that of 10Mo/TS, indicating the presence of an interaction between vanadium and molybdenum on V10Mo/TS. In the case of TSM, the pre-edges of 10TSM and V/10TSM are almost identical, indicating that the local symmetry around molybdenum in TSM is not affected by the presence of vanadium.

3.7. Mo K-edge EXAFS spectroscopy

The k^3-weighted EXAFS spectra of the Mo K-edge and the corresponding Fourier transforms (radial structure function; RSF) of 30Mo/TiO_2 and 30Mo/TS are shown in Figure 11, where the data of crystalline MoO_2 and MoO_3 are shown for reference. Intense peaks at 0.8–2.0 Å assigned to Mo–O are observed for all samples [28–31]. Furthermore, 30Mo/TiO_2 and 30Mo/TS exhibit EXAFS oscillations similar to those of crystalline MoO_3, with a predominant peak at 3.0–4.0 Å owing to Mo–Mo interactions. The majority of molybdenum oxides on these samples are found to be present as crystalline MoO_3, which is in good agreement with the XRD results.

The EXAFS oscillations and RSF of the samples containing 10 wt% molybdenum oxides either with or without vanadium and supported on TiO_2 or TS are presented in Figure 12. The EXAFS spectra and RSF of 10Mo/TiO_2 and 10Mo/TS are quite different from those of crystalline MoO_3, and peaks are observed at approximately 2.4 and 3.0 Å. Although small peaks corresponding to MoO_3 are observed in the XRD patterns (Figure 4), the majority of molybdenum oxides have different structures to crystalline MoO_3. According to the literature concerning the EXAFS spectra of analogous MoO_3/TiO_2 catalysts [32], the peaks observed at 2.0–3.5 Å for samples with lower molybdenum loadings are ascribable to Mo–Mo or Mo–Ti interactions.

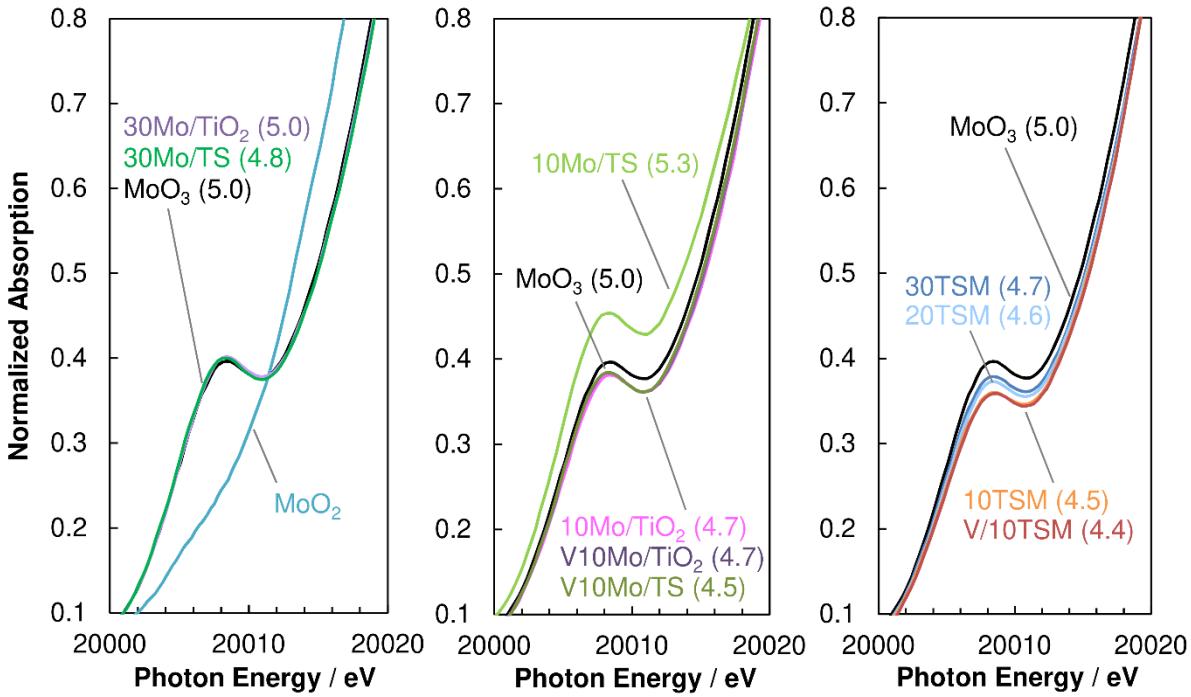

Figure 10. Enlarged pre-edge regions in the normalized Mo K-edge XANES spectra. The values in parentheses are the pre-edge peak areas obtained by pseudo-Voigt fitting.

The positions and intensities of the peaks observed in the 2.0–3.5 Å region of the RSF in Figure 12 are summarized in Table 5. The amplitudes of peaks A and B in the RSF of 10Mo/TS are lower than those in the RSF of 10Mo/TiO_2, indicating a lower crystallinity and/or the presence of monomeric molybdenum species, as suggested by the XRD (Figure 4) and XANES results (Figure 10). Mensch et al. suggested that higher peaks close to 3 Å in the RSF of Mo K-edge EXAFS spectra reflect the polymerization of molybdenum species [28], thereby supporting the present results.

The Mo K-edge EXAFS spectra and the RSF of V10Mo/TiO_2 and V10Mo/TS are similar to those of the samples without vanadium. A slight shift to shorter distances is observed for peak B after the addition of vanadium. This change indicates the presence of interactions between vanadium and molybdenum, as suggested by the XRD and XANES results. The morphology around molybdenum seems to be altered by these interactions.

The EXAFS oscillations and RSF for TSM and V/10TSM are shown in Figure 13. The EXAFS spectrum and RSF of 30TSM are similar to those of 10Mo/TS (Figure 12), with peaks being observed close to 2.4 and 3.0 Å in the RSF. In accordance with the XRD results, it is confirmed that crystalline MoO_3 is not formed in 30TSM.

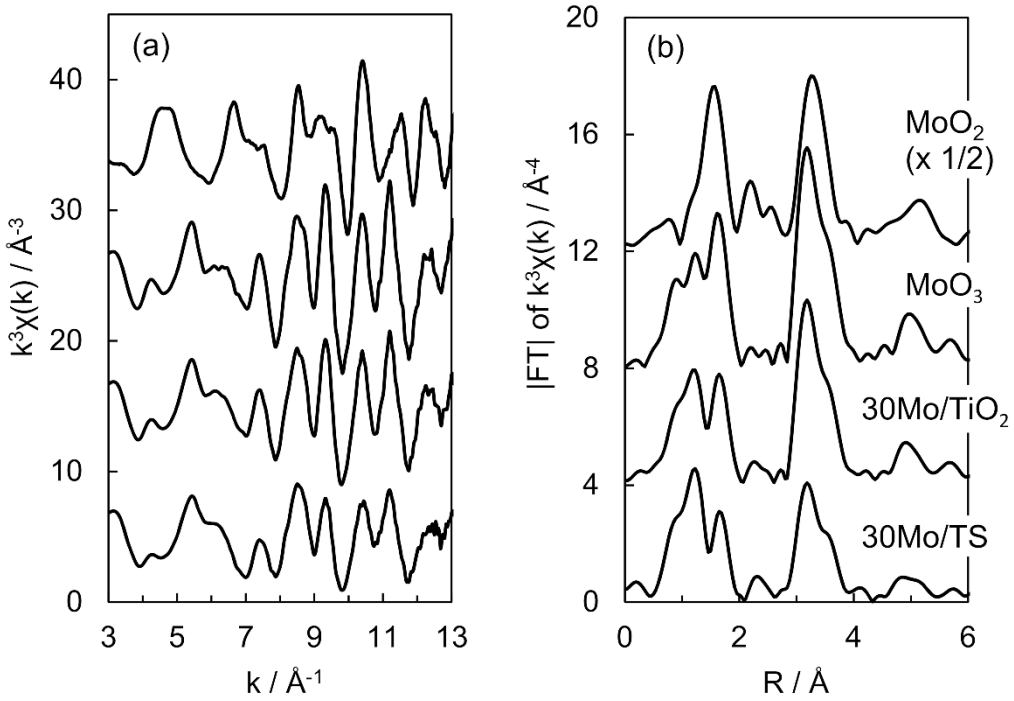

Figure 11. (a) k^3-weighted Mo K-edge EXAFS spectra, and (b) corresponding Fourier transforms of the Mo-containing catalysts and reference samples.

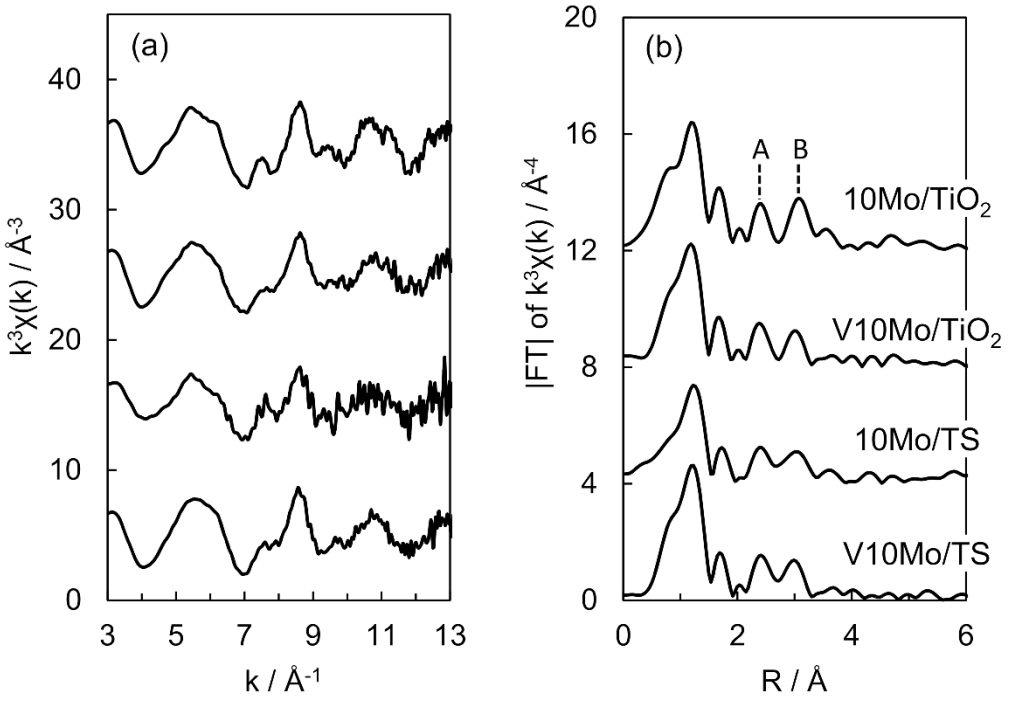

Figure 12. (a) k^3-weighted Mo K-edge EXAFS spectra, and (b) corresponding Fourier transforms of the samples containing 10 wt% molybdenum oxide.

Furthermore, changes in the EXAFS oscillations and RSF are observed as the molybdenum content decreases, and 10TSM shows a characteristic spectrum that is clearly different from those of MoO_2, MoO_3, Mo/TiO_2, and Mo/TS. The positions and intensities of peaks A and B in Figure 13 are shown in Table 5. Shifts to longer distances for peak A and to shorter distances for peak B are observed, correlating to the molybdenum contents in the TSM sample. In addition, the amplitudes of peaks A and B increase with a decrease in the molybdenum content.

V/10TSM demonstrates an EXAFS spectrum similar to that of 10TSM, but peak B is shifted to a lower distance in the RSF. These results indicate that interactions between vanadium and molybdenum occur in the V/10TSM catalyst, similar to those in the other two V–Mo containing catalysts. However, the structure of 10TSM was mostly maintained following the addition of vanadium.

3.8. Ti K-edge EXAFS spectroscopy

The k^3-weighted EXAFS spectra of the Ti K-edge and the corresponding RSF of TiO_2 and 10TSM are shown in Figure 14, with the Mo K-edge EXAFS data for 10TSM and $10Mo/TiO_2$. The TiO_2 used as the support material for $10Mo/TiO_2$ has an anatase structure (confirmed by XRD, data not shown). The EXAFS oscillations in the Mo K-edge spectrum of 10TSM resemble those in the Ti K-edge EXAFS spectra of anatase TiO_2 and 10TSM in the k range of 7–11.5 $Å^{-1}$ (dotted rectangle, Figure 14a), suggesting that the Mo–Mo or Mo–Ti distances in 10TSM are very similar to the Ti–Ti distances in anatase TiO_2. This similarity is reflected in the RSF in the R range of 2–3 Å, whereas the EXAFS spectrum and RSF of $10Mo/TiO_2$ in these ranges are obviously different from those of TiO_2.

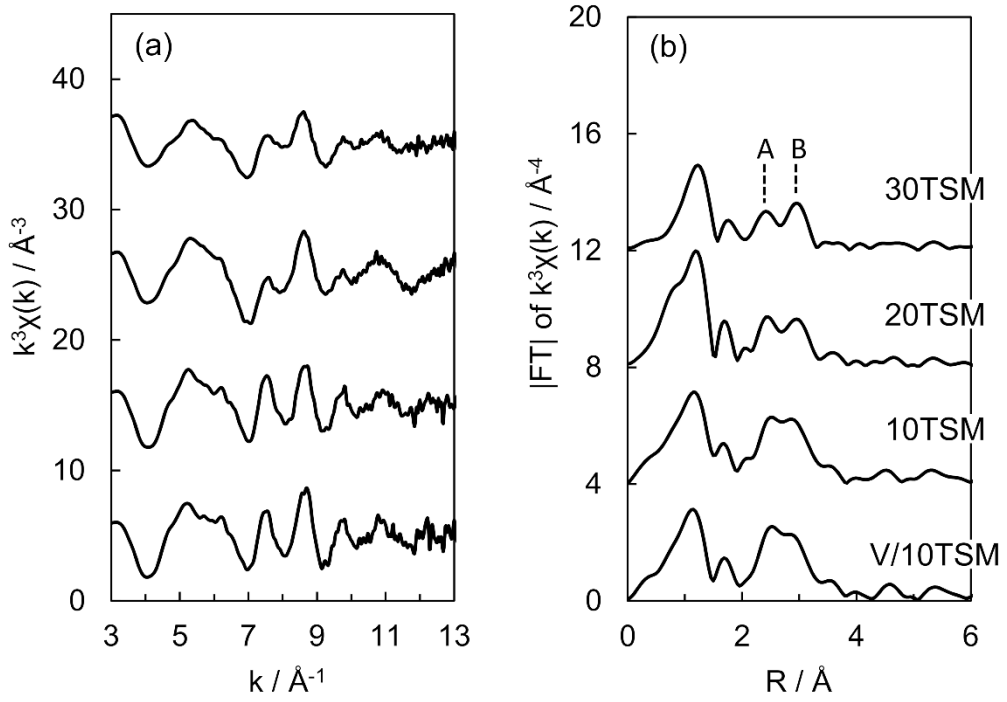

Figure 13. (a) k^3-weighted Mo K-edge EXAFS spectra, and (b) corresponding Fourier transforms of the TSM and V/TSM samples.

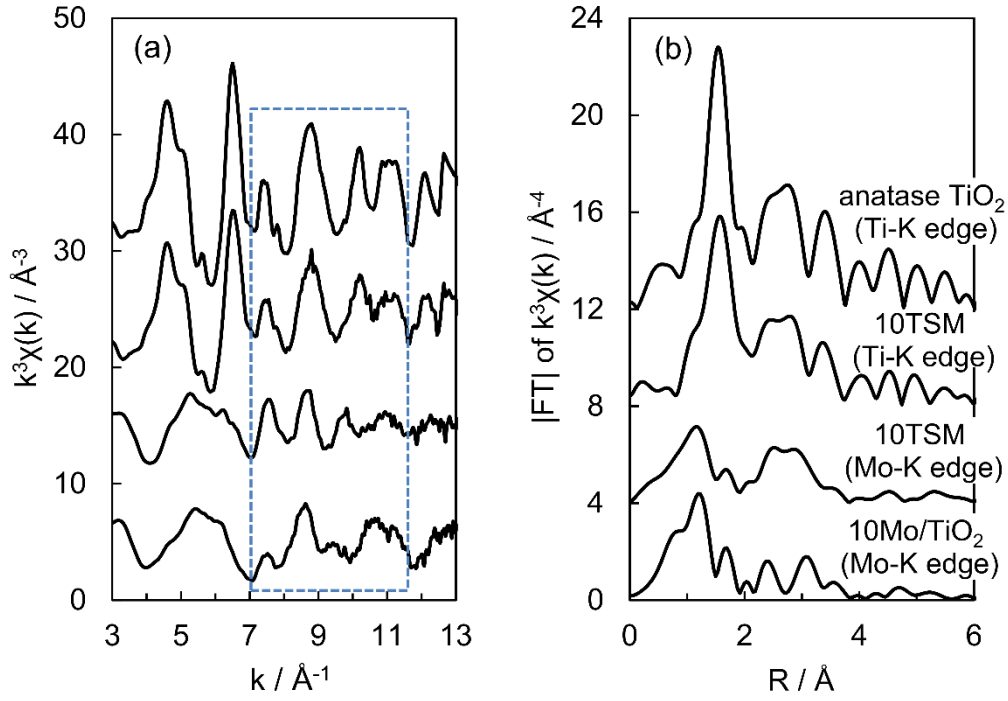

Figure 14. (a) k^3-weighted Ti and Mo K-edge EXAFS spectra, and (b) corresponding Fourier transforms of 10TSM and TiO_2-based samples.

Table 5

Positions and intensities of peaks A and B in the RSF in Figs. 12 and 13

	Peak A		Peak B	
	Position	Intensity	Position	Intensity
10Mo/TiO_2	2.42	1.61	3.07	1.79
V10Mo/TiO_2	2.38	1.51	2.99	1.25
10Mo/TS	2.42	1.25	3.03	1.10
V10Mo/TS	2.42	1.54	2.99	1.38
30TSM	2.42	1.34	2.95	1.63
20TSM	2.45	1.73	2.95	1.65
10TSM	2.53	2.29	2.88	2.22
V/10TSM	2.53	2.55	2.84	2.23

4. Discussion

4.1. Structural characteristics of molybdenum in V/TSM catalysts

V/TSM catalysts, which are highly active for NH_3-SCR [17], also exhibit superior activity for the oxidative decomposition of *o*-chlorotoluene, especially at low temperatures (Figure 2). The V10Mo/TiO_2 catalyst showed the lowest activity, probably owing to its small surface area (Table 1). In contrast, the V/10TSM catalyst exhibited a higher activity than the V10Mo/TS catalyst, which had a higher surface area, thereby suggesting that the catalytic activity is affected by factors other than the surface area.

The V K-edge XANES spectra (Figure 7) revealed that vanadium supported on TSM exhibits enhanced reducibility. Chang et al. suggested that the redox capability of vanadium is important for the oxidative decomposition of 1,2-dichlorobenzene [33]. Similarly, the redox capability of the vanadium species may contribute to the higher activity of V/TSM catalysts.

The major difference between V/10TSM and V10Mo/TS is the method for adding molybdenum. Therefore, the physicochemical properties of molybdenum in the V/TSM catalyst were investigated, and the XRD results showed that molybdenum is dispersed in the TSM support with a structure different from crystalline MoO_3 (Figure 4). The observed shift of the XRD peaks toward lower angles indicates an expansion of the interplanar distance brought about by the presence of molybdenum added by the coprecipitation method.

Moreover, as demonstrated by XPS, molybdenum is incorporated into the bulk structure of the TSM support, and no obvious differences are observed in the electronic behavior of the molybdenum species on the surface (Figure 6). Mo K-edge XANES spectroscopy revealed that the oxidation state of molybdenum in V/10TSM is 6+ and that

the octahedral structure around molybdenum is less distorted than in V10Mo/TS and V10Mo/TiO_2 (Figure 10). These results suggest that the electronic behavior of the surface molybdenum species has almost no influence on the catalytic activity for *o*-chlorotoluene decomposition.

In addition, the RSF data obtained from the Mo K-edge EXAFS spectra established that the Mo–Mo or Mo–Ti distances in the TSM support are different from those in crystalline MoO_3, Mo/TiO_2, and Mo/TS (Figs. 11–13). In the RSF of 10TSM, the peaks A and B were located close to each other and the peak amplitudes were higher than those in other samples. These results imply that the structure of the V/10TSM catalyst is different from those of the other samples, and that 10TSM mostly consists of molybdenum oxide species with similar structures.

The author attempted a curve-fitting analysis on the second shell contributions in the Mo K-edge EXAFS spectra. However, good fitting for the TSM-type samples could not be obtained because in this case, the second shell consists of more than two scatterings and the author could not find an appropriate structural model for these peaks. Moreover, evaluation of the inverse Fourier transforms of the second shell did not reveal any significant difference between the TSM samples and 10Mo/TS, due to overlapping of plural EXAFS oscillations.

In contrast, according to past studies [34,35], Ti^{4+} (0.068 nm) in the lattice can be replaced by Mo^{6+} (0.062 nm), because they have similar ionic radii. Thus, molybdenum in the TSM support can be homogeneously incorporated into the TS framework as Mo^{6+}, forming a solid solution. Furthermore, the RSF of the Ti K-edge and Mo K-edge EXAFS spectra (Figure 14) correspond to the second-shell contributions, and indicate that the Mo–Mo or Mo–Ti distances are very similar to the Ti–Ti distances in anatase TiO_2, strongly supporting the formation of a TSM solid solution.

4.2. Influence of molybdenum oxides on the performance of V/TSM catalysts

The XRD and Mo K-edge XAFS analyses revealed the presence of V–Mo interactions in the V–Mo-containing catalysts, and it was found that the structural changes around molybdenum after the addition of vanadium were not remarkable for 10TSM (Figs. 10 and 13). However, the changes in the V K-edge XANES spectra after heating to 200 °C under flowing N_2 were most evident for V/10TSM (Figure 7). These findings suggest that the superior catalytic activity of V/10TSM is the result of electronic interactions, mainly from the TSM support toward vanadium.

Tsai et al. reported that Mo-doped TiO_2 nanoparticles form a solid solution and that electron transfer from the support material to the active component is induced by oxygen vacancies generated in the nanoparticles [36]. It should be noted that the morphology around molybdenum in these Mo-doped TiO_2 nanoparticles was found to be tetrahedral, which is different from the octahedral structure of molybdenum oxide in the TSM support in the present study. This difference in structure is presumably ascribable to different preparation methods. However, similar to the case of Mo-doped TiO_2 nanoparticles, the author believes that the electron transfer process is related to oxygen vacancies generated in the TSM solid solution.

While 30TSM exhibited a larger interplanar distance than 10TSM (Figure 5), V/10TSM demonstrated a higher activity than V/30TSM (Figure 3). These results indicate that the extent of electron transfer depends not on the total extent of distortion in the anatase TiO_2 framework, but on the local morphologies around molybdenum in the TSM support. Thus, electron transfer from the TSM support to vanadium is found to be enhanced when octahedrally coordinated molybdenum with a less distorted structure is well dispersed in the TSM support, in which Ti^{4+} is replaced by Mo^{6+}. The characteristics

and unique structure of the TSM support contribute to enhancing the redox capability of vanadium in the V/TSM catalyst, resulting in a remarkable low-temperature *o*-chlorotoluene decomposition activity.

The author previously reported that the V/TSM catalyst exhibits an improved NH_3-SCR activity, which seemed to be related to the redox properties of V/TSM [17]. The results in the present study are consistent with this hypothesis and enabled the author to confirm it to be correct, with additional evidence for the role of the support material. Furthermore, it was found that the enhanced redox capability of V/TSM is also effective for the low temperature oxidative decomposition of *o*-chlorotoluene. As a result, the simultaneous decomposition of both NO_x and dioxins can be achieved with a lower catalyst volume.

5. Conclusions

The author herein reported the investigation into the physicochemical characteristics of molybdenum oxide in V/TiO_2–SiO_2–MoO_3 (TSM) catalysts using X-ray diffraction (XRD), X-ray photoelectron spectroscopy (XPS), and X-ray absorption fine structure spectroscopy (XAFS), and their performance for the oxidative decomposition of *o*-chlorotoluene was examined. The V/TSM catalysts showed superior performance for the low-temperature oxidative decomposition of *o*-chlorotoluene, especially in the case of the TSM support containing 10 wt% molybdenum oxide. The vanadium species supported on 10TSM exhibited a higher reducibility, and this improved redox capability of vanadium is likely responsible for the enhanced catalytic activity. XRD, XPS, and Mo K-edge XAFS analyses revealed that the molybdenum present in the

TSM support is octahedrally coordinated, with a less distorted structure than in the case of crystalline MoO_3, and is also highly dispersed inside the TSM framework, thereby indicating the formation of a solid solution. Preparation of the TSM supports via a coprecipitation method appeared to result in the Ti^{4+} within the TiO_2 structure being replaced by Mo^{6+}. Electron transfer from the TSM support to the vanadium species was enhanced by the coexistence of Mo^{6+} and Ti^{4+}, and thus the redox capability of the vanadium species supported on TSM was enhanced. However, the extent of electron transfer depended not on the total distortion of the anatase TiO_2 framework, but on the local morphologies around the molybdenum in TSM. Thus, the superior performance of the V/10TSM catalyst for the low-temperature decomposition of *o*-chlorotoluene was attributed to the high dispersion of Mo^{6+} species in the 10TSM solid solution, which has a unique structure around molybdenum. This detailed physicochemical investigation provided insight into the structure of the TSM solid solution, and the enhanced redox capability of V/TSM was revealed to be effective for the low temperature oxidative decomposition of *o*-chlorotoluene. However, as the behaviors of the vanadium species and the support material during catalytic reactions have yet to be elucidated, future work in the author's group will focus on these points to contribute to the development of novel catalysts for improved NO_x and dioxins abatement.

Acknowledgements

The author acknowledges Dr. K. Kimijima (High Energy Accelerator Research Organization, KEK) and Professor K. Okumura (Kogakuin University) for helpful and valuable assistance in the XAFS experiments. Publication permission and funding from Nippon Shokubai Co., Ltd. is also gratefully acknowledged.

References

[1] L. Lietti, J. Svachula, P. Forzatti, G. Busca, G. Ramis, P. Bregani, *Catal. Today* **1993**, *17*, 131–139.

[2] G. Busca, L. Lietti, G. Ramis, F. Berti, *Appl. Catal. B Environ.* **1998**, *18*, 1–36.

[3] M. Kobayashi, R. Kuma, S. Masaki, N. Sugishima, *Appl. Catal. B Environ.* **2005**, *60*, 173–179.

[4] J. M. Herrmann, J. Disdier, *Catal. Today* **2000**, *56*, 389–401.

[5] I. Giakoumelou, C. Fountzoula, C. Kordulis, S. Boghosian, *J. Catal.* **2006**, *239*, 1–12.

[6] S. T. Choo, Y. G. Lee, I.-S. Nam, S.-W. Ham, J.-B. Lee, *Appl. Catal. A Gen.* **2000**, *200*, 177–188.

[7] S. Krishnamoorthy, J. P. Baker, M. D. Amiridis, *Catal. Today* **1998**, *40*, 39–46.

[8] S. Krishnamoorthy, M. D. Amiridis, *Catal. Today* **1999**, *51*, 203–214.

[9] M. A. Larrubia, G. Busca, *Appl. Catal. B Environ.* **2002**, *39*, 343–352.

[10] E. Finocchio, G. Busca, M. Notaro, *Appl. Catal. B Environ.* **2006**, *62*, 12–20.

[11] D. P. Debecker, R. Delaigle, K. Bouchmella, P. Eloy, E. M. Gaigneaux, P. H. Mutin, *Catal. Today* **2010**, *157*, 125–130.

[12] C. Gannoun, R. Delaigle, D. P. Debecker, P. Eloy, A. Ghorbel, E. M. Gaigneaux, *Appl. Catal. A Gen.* **2012**, *447–448*, 1–6.

[13] M. feng Yu, W. wei Li, X. dong Li, X. qing Lin, T. Chen, J. hua Yan, *Chemosphere* **2016**, *156*, 383–391.

[14] C. E. Hetrick, J. Lichtenberger, M. D. Amiridis, *Appl. Catal. B Environ.* **2008**, *77*, 255–263.

[15] G. Busca, M. Baldi, C. Pistarino, J. M. Gallardo Amores, V. Sanchez Escribano,

E. Finocchio, G. Romezzano, F. Bregani, G. P. Toledo, *Catal. Today* **1999**, *53*, 525–533.

[16] M. Hiraoka, T. Fujii, K. Kashiwabara, K. Ieyama, M. Kondo, *Chemosphere* **1991**, *23*, 1439–1444.

[17] M. Kobayashi, R. Kuma, A. Morita, *Catal. Letters* **2006**, *112*, 37–44.

[18] N. Sugishima, M. Kobayashi, *Shokubai* **2001**, *43*, 559–564.

[19] S. Yamazoe, Y. Hitomi, T. Shishido, T. Tanaka, *J. Phys. Chem. C* **2008**, *112*, 6869–6879.

[20] B. M. Reddy, B. Chowdhury, P. G. Smirniotis, *Appl. Catal. A Gen.* **2001**, *219*, 53–60.

[21] F. Amano, T. Tanaka, *Catal. Commun.* **2005**, *6*, 269–273.

[22] W. C. Vining, J. Strunk, A. T. Bell, *J. Catal.* **2012**, *285*, 160–167.

[23] J. Wong, F. W. Lytle, R. P. Messmer, D. H. Maylotte, *Phys. Rev. B* **1984**, *30*, 5596–5610.

[24] K. L. Bøyesen, K. Mathisen, *Catal. Today* **2014**, *229*, 14–22.

[25] S. Takenaka, T. Tanaka, T. Yamazaki, T. Funabiki, S. Yoshida, *J. Phys. Chem. B* **1997**, *101*, 9035–9040.

[26] H. Aritani, T. Tanaka, T. Funabiki, S. Yoshida, M. Kudo, S. Hasegawa, *J. Phys. Chem.* **1996**, *100*, 5440–5446.

[27] K. Shimura, H. Kanai, K. Utani, K. Matsuyama, S. Imamura, *Appl. Catal. A Gen.* **2005**, *283*, 117–124.

[28] C. T. J. Mensch, J. A. R. Van Veen, B. Van Wingerden, M. P. Van Dijk, *J. Phys. Chem.* **2005**, *92*, 4961–4964.

[29] R. Radhakrishnan, C. Reed, S. T. Oyama, M. Seman, J. N. Kondo, K. Domen, Y. Ohminami, K. Asakura, *J. Phys. Chem. B* **2001**, *105*, 8519–8530.

[30] S. Takenaka, T. Tanaka, T. Funabiki, S. Yoshida, *J. Phys. Chem.* **1998**, *102*, 2960–2969.

[31] J. A. Wharton, D. H. Ross, G. M. Treacy, G. D. Wilcox, K. R. Baldwin, *J. Appl. Electrochem.* **2003**, *33*, 553–561.

[32] M. J. Fay, A. Proctor, D. P. Hoffmann, M. Houalla, D. M. Hercules, *Mikrochim. Acta* **1992**, *109*, 281–293.

[33] H.-Y. Chang, S.-P. Wang, J.-R. Chang, H.-S. Sheu, S.-G. Shyu, *Appl. Catal. B Environ.* **2012**, *111–112*, 476–484.

[34] Y. J. Feng, C. Wang, W. R. Cheng, J. H. Huang, T. X. Zhao, Q. H. Liu, Z. Xie, Z. Y. Pan, S. Q. Wei, *J. Phys. Conf. Ser.* **2013**, *430*, 012090.

[35] H. W. Kang, S. Bin Park, A. H. A. Park, *Int. J. Hydrogen Energy* **2013**, *38*, 9198–9205.

[36] M. C. Tsai, T. T. Nguyen, N. G. Akalework, C. J. Pan, J. Rick, Y. F. Liao, W. N. Su, B. J. Hwang, *ACS Catal.* **2016**, *6*, 6551–6559.

Chapter 4

In-situ XANES Characterization of $V_2O_5/TiO_2–SiO_2–MoO_3$ Catalyst for Selective Catalytic Reduction of NO by NH_3

Abstract

The structures of V_2O_5 catalysts for the selective catalytic reduction (SCR) of NO by NH_3 at low temperatures are investigated using *in-situ* V K-edge X-ray absorption near-edge structure measurements. The V_2O_5 catalyst supported on $TiO_2–SiO_2–MoO_3$ mixed oxide (V/TSM) showed a significantly steep increase in the main-edge energy at the beginning of the reaction. The results indicate that the excellent NH_3-SCR catalytic activity of V/TSM can be ascribed to the remarkable V^{4+}-to-V^{5+} reoxidation capability, and the easier V^{5+}-to-V^{4+} reducibility. This improved redox reactivity is induced by the interaction of the highly dispersed polymeric vanadate with TSM solid solution and by the appropriate surface geometry of vanadium species, which enabled contact with NH_3 and O_2 in the gas phase. The results reported herein should enable the development of improved catalysts for NH_3-SCR.

1. Introduction

Selective catalytic reduction (SCR) of NO_x (NO and NO_2) by NH_3, referred to as NH_3-SCR, is a well-proven NO_x treatment technology that has been used for several decades for the treatment of flue gases from stationary sources. Vanadium oxide catalysts supported on titania (anatase) have been commercially used owing to their high NH_3-SCR activity and resistance against sulfur oxide poisoning [1–6]. Conventional V_2O_5-WO_3/TiO_2 NH_3-SCR catalysts exhibit superior NH_3-SCR activity and durability at elevated temperatures (300–400 °C). In these systems, tungsten oxide acts as a promoter by enhancing the thermal durability of TiO_2 and by altering the surface morphology and surface acidity of vanadium species [7–11]. On the other hand, catalysts containing molybdenum oxide as the promoter instead of tungsten oxide have been employed in industrial applications for the treatment of gases, including flue gases from desulfurizers and municipal waste incinerators, and allow operation at lower temperatures (below 200 °C) [12,13]. Manganese-based catalysts such as Mn-Ce/TiO_2 are also known to exhibit high activity at temperatures below than 180 °C [14–22]. However, V_2O_5/TiO_2-type catalysts are the most commonly applied catalysts for commercial waste gas treatments, as they have been widely used for a long time.

The author previously reported the structure of a TiO_2–SiO_2–MoO_3 (TSM) mixed oxide synthesized via a coprecipitation method and the reactivity of vanadium oxide catalysts supported on TSM (V/TSM) for low-temperature NH_3-SCR [23]. By analyzing the Raman spectra and X-ray diffraction (XRD) data, the author concluded that the highly dispersed polymeric vanadate species on TSM constitute a key factor for its high performance. Further investigations of the V/TSM catalyst using X-ray absorption fine structure spectroscopy (XAFS) and X-ray photoelectron spectroscopy (XPS) revealed

that Mo^{6+} and Ti^{4+} coexist in the anatase-TiO_2 structure of the TSM support, forming a solid solution [24]. However, these analyses were conducted in air at ~25 °C or at high temperatures, and to the best of the author's knowledge, no other studies have reported a similar subject. Therefore, the catalyst structure and reaction mechanism under the reaction gas flow containing NO and NH_3 remain unclear.

XAFS is an effective method for determining the oxidation state and local geometry of vanadium-based catalysts [24–28]. However, there are only a few reported applications of XAFS for studying NH_3-SCR catalysts under the reaction conditions [29–31]. Therefore, the author investigated three kinds of industrial V_2O_5/TiO_2-type catalysts for the NH_3-SCR reaction, including V/TSM, using temperature-programmed reduction with H_2 (H_2-TPR) to provide further insights into the reducibility. Furthermore, the author performed *in-situ* XANES under the reaction conditions to clarify the local structure and oxidation state of the vanadium active center during NH_3-SCR. Herein, the author reports these characteristics of the catalysts in combination with the NH_3-SCR reaction to determine factors that affect catalytic activity.

2. Experimental

2.1. Catalyst preparation

The catalysts were prepared by a method described previously [23,24]. TSM mixed oxide was prepared by a coprecipitation method. Ammonium molybdate (Taiyo Koko Co., Ltd.), silica sol (30 wt% SiO_2, Nissan Chemical Corp.), and aqueous titanyl sulfate solution (70 g/L TiO_2, Tayca Corp.) were mixed with ammonia solution. The resultant mixture was aged at 30 °C for 10 h, following which the precipitate was separated by filtration, and washed with distilled water. The prepared material was placed in a

stainless-steel tray and heated in a box-type furnace at a rate of 100 °C/h to calcine at 500 °C for 3 h in a static air atmosphere. After calcination, the samples were cooled naturally in the furnace to ambient temperature. TiO_2–SiO_2 (TS) and TiO_2 were prepared similarly.

The incipient wetness method was employed for MoO_3/TiO_2 (Mo/TiO_2) using aqueous ammonium molybdate solution. For example, 10 wt% MoO_3/TiO_2 was obtained by mixing ammonium molybdate (1.36 g), monoethanol amine (0.55 g, Nippon Shokubai), and deionized water (5 g) with TiO_2 powder (10 g) at approximately 25 °C. The obtained materials were dried, calcined, and pulverized under the same conditions as those employed for TSM. These samples are designated as "*X*Mo/TiO_2" and "*X*TSM," where *X* is the weight percent of MoO_3.

A V/TSM honeycomb monolithic catalyst was prepared by an extrusion-molding method, as described previously [23]. Briefly, 10TSM powder was mixed with an aqueous solution containing ammonium vanadate, oxalic acid, and monoethanol amine. The resultant blend was extruded to form a monolithic catalyst, with a pitch of 3.2 mm, outer diameter of 50 mm, and length of 300 mm. The catalyst was dried at 60 °C for 10 h and heated in a box-type furnace at a rate of 50 °C/h to calcine at 450 °C for 5 h in a mixed air atmosphere. A V_2O_5/TS (V/TS) honeycomb-monolithic catalyst was prepared using TS powder, following the same procedure as that used for V/TSM. In addition, the same method was employed to prepare V_2O_5–MoO_3/TiO_2 (VMo/TiO_2) by using an aqueous solution containing ammonium molybdate, ammonium metavanadate, oxalic acid, and monoethanol amine. The loading amount of vanadium for each catalyst was fixed at 8 wt% V_2O_5. The compositions of the samples are summarized in Table 1. Derived from titanyl sulfate, ~0.5 wt% of sulfur was present in V/TS, VMo/TiO_2 and V/TSM.

Table 1. Physico-chemical properties of the support materials and V-Mo catalysts

Sample	Composition (wt%)				BET specific surface area (m^2/g)
	TiO_2	SiO_2	MoO_3	V_2O_5	
TiO_2	100	-	-	-	82
TS	93.0	7.0	-	-	163
10Mo/TiO_2	90.0	-	10.0	-	64
30Mo/TiO_2	70.0	-	30.0	-	55
10TSM	83.0	7.0	10.0	-	135
30TSM	63.0	7.0	30.0	-	115
V/TS	85.6	6.4	-	8.0	140
VMo/TiO_2	82.0	-	10.0	8.0	60
V/TSM	76.4	6.4	9.2	8.0	101

2.2. Catalyst characterization

A Mountech Macsorb model-1210 apparatus was used for determining the Brunauer–Emmett–Teller (BET) specific surface areas of the catalysts. The samples were degassed by flowing N_2 at 200 °C for 60 min before the measurement. XRD measurements were performed under ambient conditions in a scanning range of 2θ = 5–80°, using a Rigaku SmartLab diffractometer with Cu Kα radiation.

The author conducted H_2-TPR experiments using a BEL-CAT apparatus (Bell Japan Inc.). The powdered sample (100 mg) was placed in a quartz tube and preheated under the flow of 5 vol% O_2 in Ar at 450 °C for 20 min. After cooling to 50 °C, a stream of 5 vol% H_2 in Ar was fed into the quartz tube, which was then heated to 700 °C at 10 °C/min under the same H_2/Ar flow. The consumed H_2 was detected by a thermal conductivity detector (TCD) using He as the carrier gas.

The V K-edge XANES spectra were measured at the BL-9C beam line of the High-Energy Accelerator Research Organization (KEK-PF), with a ring energy of 2.5 GeV, in the transmission mode with a Si (111) monochromator.

Reaction gases were mixed using individual mass flow controllers at a total flow rate of 200 cm^3/min. The mixed reaction gas contained 200 ppm NO, 200 ppm NH_3, 10 vol% O_2, and 10 vol% H_2O, with N_2 as the balance gas, and water was fed via a saturator. Only N_2 and O_2 were set to pass the saturator, after which NO and NH_3 were fed into the gas stream at the outlet of the saturator to avoid the absorption of NO and NH_3 in liquid water.

Typically, the sample powder, sieved to pass through a 100-mesh sieve, was mixed with boron nitride (Kojundo Chemical Co., Ltd.) in a 1:10 ratio (w/w), and ground with an agate mortar for 30 min. The mixed powder (55 mg) was then pressed in a stainless-steel sample holder for obtaining a self-supported sample disc with a diameter

of 7 mm and thickness of ~1 mm. The catalyst sample was then set in an *in-situ* cell sealed with Kapton film windows, which were attached to the flow-controlling system mentioned above.

Before the catalytic tests, the XANES spectra of the catalysts, were obtained at 200 °C in N_2. Subsequently, the reaction gas was introduced into the *in-situ* cell, and the XANES spectra were measured every 1 min. For comparison, crystalline reference samples (V_2O_3, V_2O_4, V_2O_3, and Na_3VO_4) were also mixed with boron nitride and pressed in the sample holder, and their XANES spectra were collected at 200 °C in N_2. The XANES spectra were analyzed using the ATHENA program.

2.3. Catalytic-activity measurement

The NH_3-SCR catalytic-activity of the three types of catalysts was assessed in the temperature range 150–350 °C in a stainless-steel tube fixed-bed reactor with an inner diameter of 38.1 mm. The honeycomb catalysts to be tested were cut to 4 × 4 cells and installed into the reactor. The reaction gas containing 200 ppm NO, 200 ppm NH_3, 10 vol% O_2, and 10 vol% H_2O, using N_2 as the balance gas, was introduced into the reactor. The gas hourly space velocity (GHSV) was controlled to 11,000 h^{-1}, by maintaining the total gas flow rate at 1.0 Nm^3/h. The concentrations of NO and NO_2 were determined using an online chemiluminescence NO_x analyzer (Thermo Fisher Scientific, Model 5100). A gas chromatograph (Shimadzu GC-14A) equipped with a Porapak-Q column was used for the analysis of N_2O. The conversion of NO was determined using the following equation.

$$\text{NO conversion} = \left(1 - \frac{C_{NO-out}}{C_{NO-in}}\right) \times 100\ (\%)$$

where $C_{NO\text{-}in}$ and $C_{NO\text{-}out}$ are the NO concentrations at the inlet and outlet, respectively.

3. RESULTS

3.1. Physicochemical properties of support materials and catalysts

The BET specific surface areas and the compositions of the vanadium oxide catalysts and their supports are summarized in Table 1. As described in the author's previous study [23], the specific surface area of 82 m^2/g for TiO_2 was approximately half those of TS (163 m^2/g) and TSM (135 m^2/g). The specific surface areas of these materials decreased upon the addition of vanadium and/or molybdenum oxides. The relationship between the loading amount and specific surface area is displayed in Figure 1. TS, V/TS, 10TSM, and V/TSM followed the same linear relationship. However, the specific surface area of 30TSM (115 m^2/g) was higher than the value predicted from this linear function.

Figure 2 shows the XRD patterns of the catalyst samples, wherein diffraction peaks associated with anatase TiO_2 (JCPDS: 00-021-1272) were present in each sample. No visible peaks of crystalline V_2O_5 (JCPDS: 00-041-1426) could be detected for the V/TS catalyst, indicating that vanadium oxide was highly dispersed on TS, likely owing to the large specific surface area.

30Mo/TiO_2 demonstrated intense peaks attributed to MoO_3 (JCPDS: 00-005-0508) in the XRD pattern; 10Mo/TiO_2 displayed weak peaks at the same positions (Figure 2b). In contrast, the XRD patterns of TSM displayed peaks ascribable to anatase TiO_2 and not MoO_3, even when 30 wt% MoO_3 was present (30TSM). These trends in the specific surface area and XRD results may be due to the incorporation of the molybdenum species into the anatase-TiO_2 structure in the TSM solid solution, as reported previously [24].

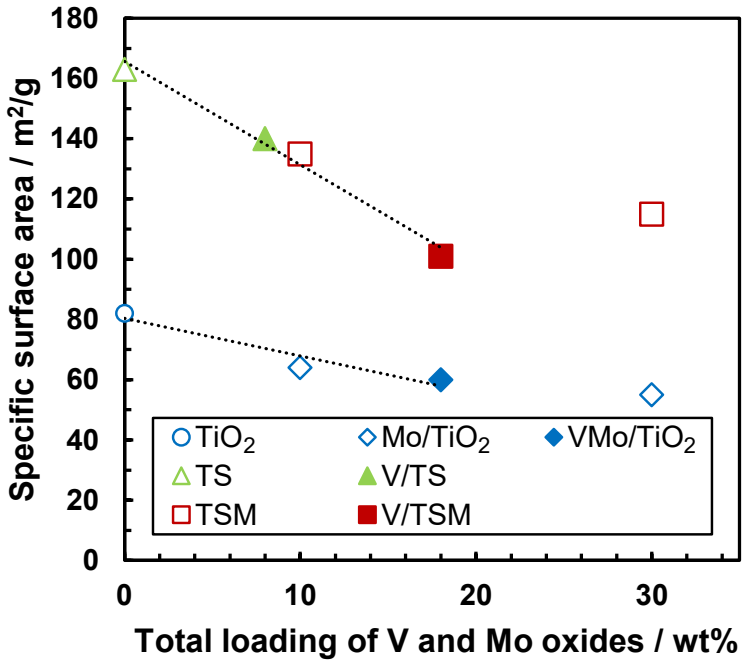

Figure 1. Relationship between loading amount and specific surface area.

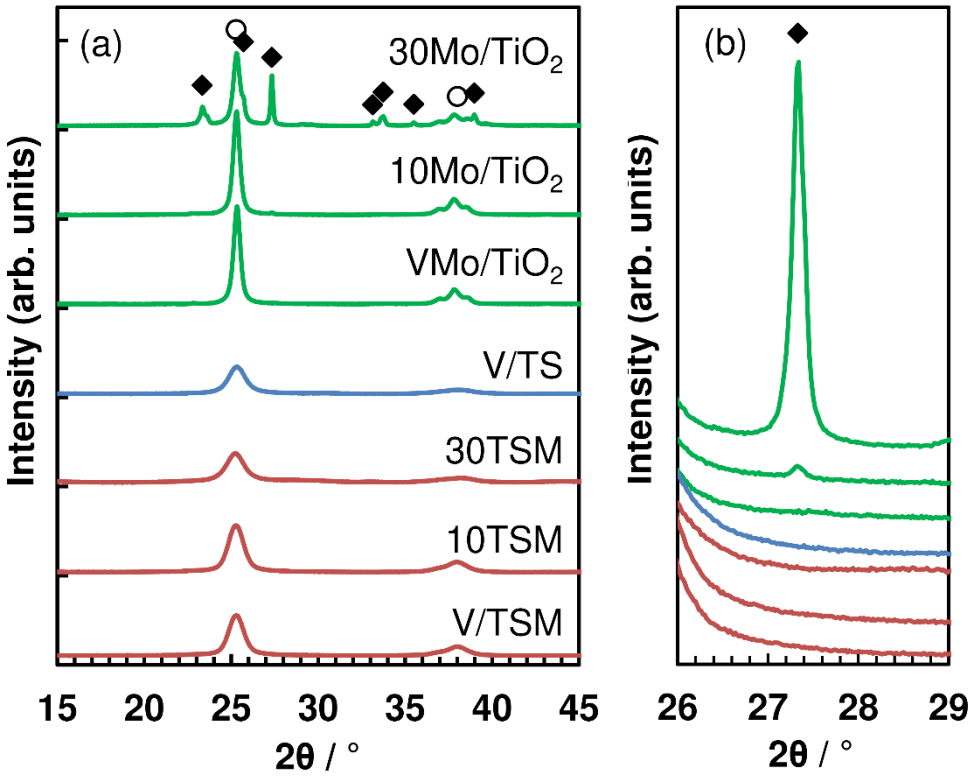

Figure 2. (a) XRD patterns of the catalysts, and (b) magnified data in the 26–29° region; symbols: TiO_2 (○) and MoO_3 (◆).

In contrast to 10Mo/TiO_2, the XRD peaks assigned to MoO_3 were unobservable for VMo/TiO_2, on which both vanadium and molybdenum oxides were loaded. This suggests a change in the structure around molybdenum atom due to an interaction between V and Mo, probably brought about by the formation of the VO_x-MoO_x species as reported by Qiu et al. [32] No XRD peaks ascribable to vanadium- or molybdenum-related compounds were observed for VMo/TiO_2 and V/TSM; indeed, only peaks assigned to anatase TiO_2 were observed. These results indicate that V and Mo are highly dispersed on the catalyst.

3.2. Steady-state catalytic-activity measurements

Catalytic activity tests for the NH_3-SCR reaction were conducted under steady-state conditions. No other components such as N_2O or NO_2 were observed in outlet gas of the reactor, indicating that the N_2 selectivity was almost 100%. As shown in Figure 3, V/TSM exhibits significantly higher catalytic activity than those of VMo/TiO_2 and V/TS within the temperature range 150–350 °C. Arrhenius plots for the NH_3-SCR activity test are shown in Figure 4.

Apparent reaction rate constant k ($cm^3g^{-1}s^{-1}$) was calculated using following equation, assuming a first-order reaction;

$$k = -\frac{F}{m} \times \ln(1 - \text{NO conversion})$$

where F and m are the total gas flow rate (cm^3s^{-1}) and the catalyst weight (g), respectively.

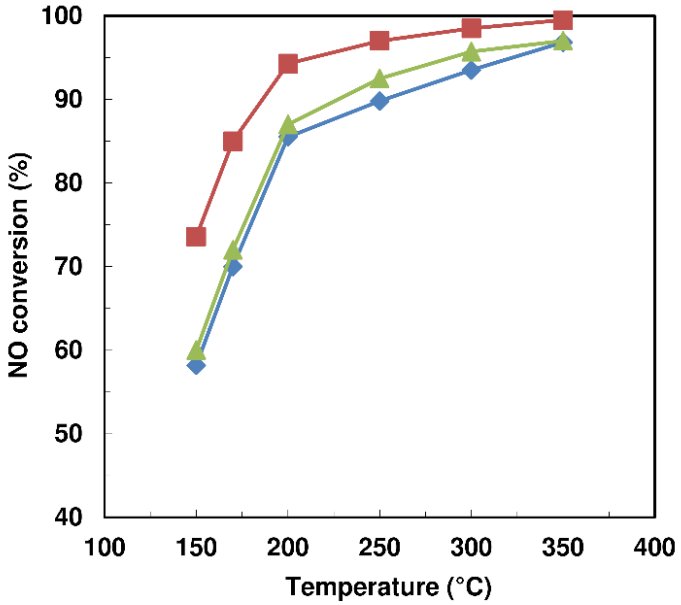

Figure 3. NH_3-SCR activities of V/TSM (■), VMo/TiO_2 (▲), and V/TS (♦). Reaction conditions: 200 ppm NO, 200 ppm NH_3, 10 vol% O_2, 10 vol% H_2O, N_2 balance, space velocity: 11,000 h^{-1}.

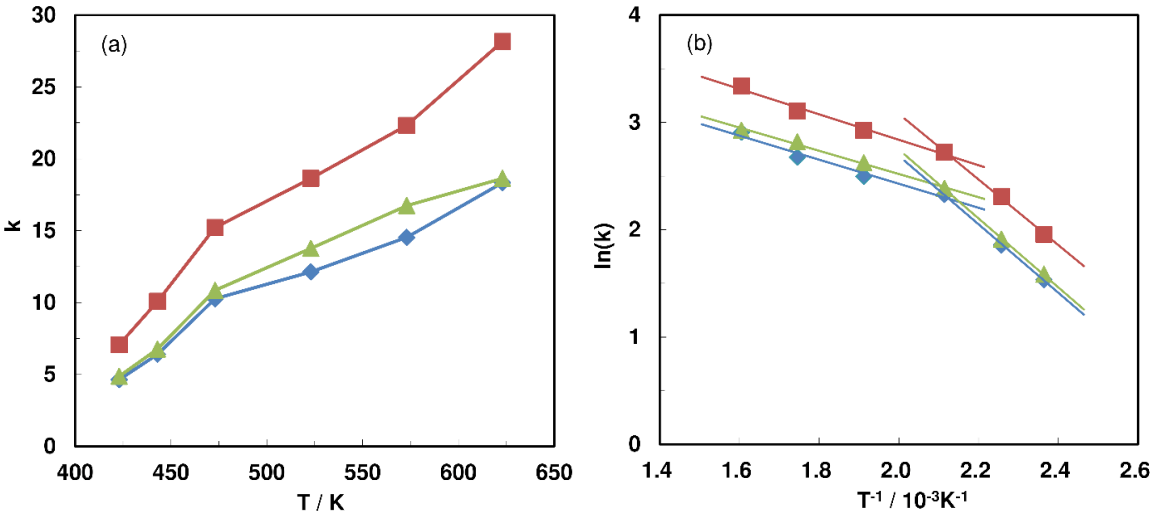

Figure 4. (a) Apparent reaction rate constant, k, assuming a first-order reaction (b) and Arrhenius plot for the NH_3-SCR activity test over V/TSM (■), VMo/TiO_2 (▲), and V/TS (♦). Reaction conditions: 200 ppm NO, 200 ppm NH_3, 10 vol% O_2, 10 vol% H_2O, N_2 balance, space velocity: 11,000 h^{-1}.

The Arrhenius plots were fitted using a linear least squares method in the temperature range 200–350 °C. However, the data obtained below 200 °C were on a different linear relationship. This variation suggests that a reaction-controlled regime was dominant at low temperatures, and shifted to a diffusion-controlled reaction by elevating the temperature.

A catalytic cycle (Scheme 1) involving the redox of vanadium species was recently proposed by Marberger et al. [33] for the NH_3-SCR reaction. According to their study, the rate-determining step of the NH_3-SCR reaction involves the reoxidation of the reduced vanadium species (step (d) in Scheme 1). Other researchers also claim that the gas-phase oxygen reoxidizes the vanadium species, and this process is very slow [34,35]. Molybdenum oxide has been reported to act as a promoter of NH_3-SCR and modifies the redox behavior of vanadium species [12,36]. Better redox properties combined with the presence of polymeric vanadate species are the main contributors to the superior activity of V/TSM, as previously reported by the author [23].

Scheme 1. Proposed reaction mechanism of NH_3-SCR.

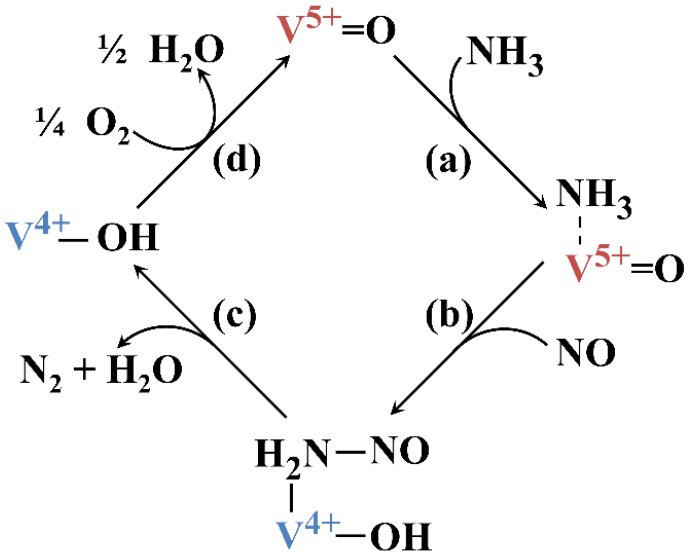

Thus, to further understand the redox properties of the V/TSM catalyst, the author performed H_2-TPR and *in-situ* XANES experiments.

3.3. Temperature-programmed reduction with H_2

The results of the H_2-TPR experiments for the support materials and catalysts are presented in Figure 5. The initial and maximum reduction temperatures (T_{onset} and T_{max}, respectively), and H_2 consumption (mol-H_2/mg-sample) obtained from the H_2-TPR data are listed in Table 2. T_{onset} was defined as the temperature at which the TCD signal exceeds a predetermined value (Figure 5(d)).

Figure 5 and Table 2 show that the TiO_2 and TS supports exhibited a small reduction peak at high temperatures near 600 °C. As indicated by Casagrande et al. [12], 10Mo/TiO_2 shows a broad H_2 consumption peak at a T_{max} of 455 °C, with tailing up to 700 °C. On the other hand, 10TSM shows a sharper peak than 10Mo/TiO_2, indicating that the molybdenum oxide species are homogeneously dispersed on 10TSM, owing to its larger specific surface area.

Notably, 10TSM exhibits higher T_{onset} and T_{max} values and lower H_2 consumption than 10Mo/TiO_2. In line with the XRD data, these results indicate that the majority of molybdenum oxide in TSM are incorporated into the anatase-TiO_2 structure throughout the coprecipitation procedure; therefore, H_2 consumption ascribable to the reduction of molybdate in the TSM is suppressed.

The H_2-TPR data of V/TS are similar to those of the analogous V_2O_5/TiO_2-SiO_2 system investigated by Gao et al. [37] In addition, V/TS exhibits higher T_{onset} and T_{max} values than 10Mo/TiO_2.

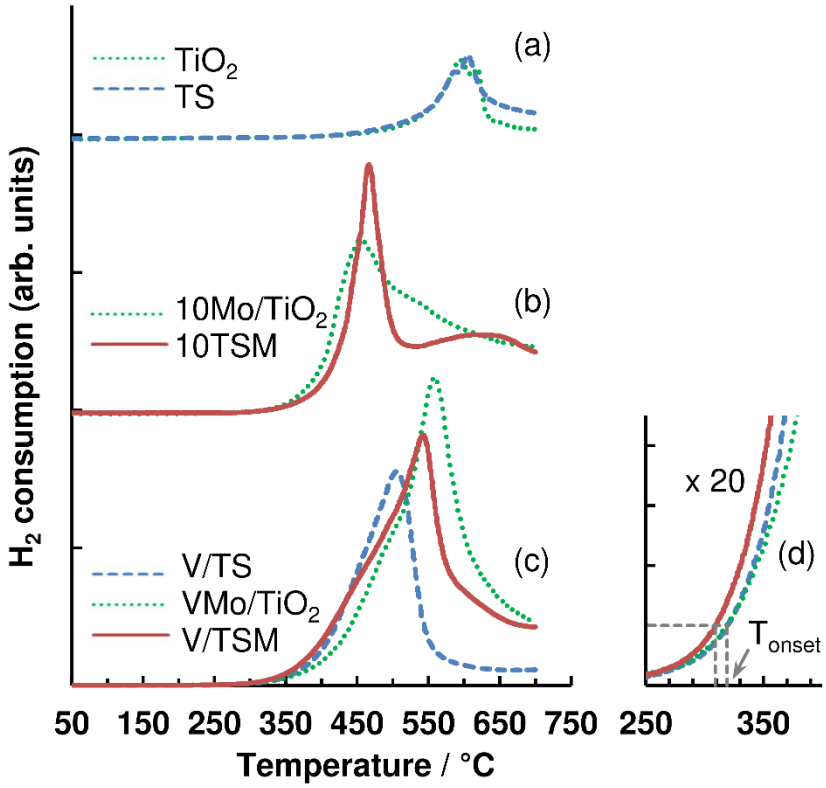

Figure 5. H_2-TPR profiles for (a) TiO_2, TS, (b) 10Mo/TiO_2, 10TSM, and (c) V/TS, VMo/TiO_2, V/TSM. (d) 20-times magnified data of (c) in the temperature range 250–400 °C.

Table 2. H_2-TPR results for the V- and/or Mo-containing samples

Sample	T_{onset} (°C)	T_{max} (°C)	H_2 consumption (mmol-H_2/g-sample)
10Mo/TiO_2	309	455	1.31
10TSM	325	467	1.15
V/TS	319	504	0.98
VMo/TiO_2	318	558	1.68
V/TSM	309	542	1.51

Casagrande et al. [12] reported that V/TiO_2 was reduced at a higher temperature compared to Mo/TiO_2, while bulk V_2O_5 was reduced at a lower temperature than MoO_3. They also suggested that supported vanadium and molybdenum oxides behave differently from the unsupported ones, owing to the interactions between supported oxides and the support material. The interactions of vanadium and molybdenum oxides on the VMo/TiO_2 catalyst surface with the nucleophilic sites of the TiO_2 support have also been reported [36].

VMo/TiO_2 and V/TSM exhibited TPR peaks at higher temperatures and consumed more H_2 than V/TS. These changes in the TPR profiles are due to the presence of both vanadium and molybdenum oxides. Quantitatively comparing the H_2 uptake in this case suggests that the H_2 consumed over VMo/TiO_2 (1.68 mmol/g) is considerably lower than the sum of the H_2 uptakes over V/TS and Mo/TiO_2 (Table 2; 0.98 and 1.31 mmol/g, respectively), suggesting an interaction between V and Mo, consistent with the XRD analysis. Similar behavior observed over V/TSM also indicates that the surface vanadate species interact with the TSM support. Moreover, V/TSM exhibits a lower T_{onset} than V/TS and VMo/TiO_2, suggesting that V/TSM can be easily reduced at low temperatures. These results demonstrate that the reducibility of V/TSM is enhanced by the strong interaction between V and Mo in the interior of the TSM support, whereas in the case of VMo/TiO_2, the interaction between V and Mo is weaker and independent of that between the V-Mo oxides and TiO_2 support [36].

3.4. In-situ XANES measurements under N_2 flow at 200 °C

Figure 6 shows the V K-edge XANES spectra of the vanadium reference compounds and vanadium-containing catalysts under N_2 flow at 200 °C. The pre-edge peak was found at ~5470 eV, and the XANES in this region was well fitted with a pseudo-

Voigt function combined with an error function (Figure 7). In this study, the main-edge position, observed at ~5480 eV, is defined as 50% of the normalized intensity. The height, full-width at half-maximum (FWHM), and position of the pre-edge peak determined from the pseudo-Voigt fitting and main-edge position for each sample are summarized in Table 3.

The pre-edge peak on the V K-edge XANES spectrum is attributed to the 3d–4p orbital hybridization of vanadium brought about by the distorted octahedral structure of the VO_x species [38–40]; the pre-edge intensity reflects the local geometry around the vanadium atom. The relatively intense pre-edge peak for crystalline V_2O_5 is related to the distortion of the VO_5 square-pyramid [40]. V_2O_3 and V_2O_4 (octahedrally coordinated) exhibited weak pre-edge peaks, whereas Na_3VO_4 (tetrahedrally coordinated) exhibited an intense and sharp pre-edge peak.

The pre-edge intensities of V/TS and VMo/TiO_2 were similar to that of crystalline V_2O_5; however, the post-edge features above 5480 eV for these catalysts exhibited different features compared to V_2O_5.

These results imply that the structures of the vanadium species in these catalysts are distorted from the octahedral VO_6 symmetry but different from the square-pyramid in V_2O_5. This suggests the coexistence of the highly distorted and less distorted VO_x species in these catalysts [26,41]. V/TSM exhibited a lower pre-edge peak than these catalysts, showing that the local geometry around the vanadium atom in V/TSM is less distorted and that a higher percentage of the vanadium species exists in its octahedral structure, compared to the other two catalysts.

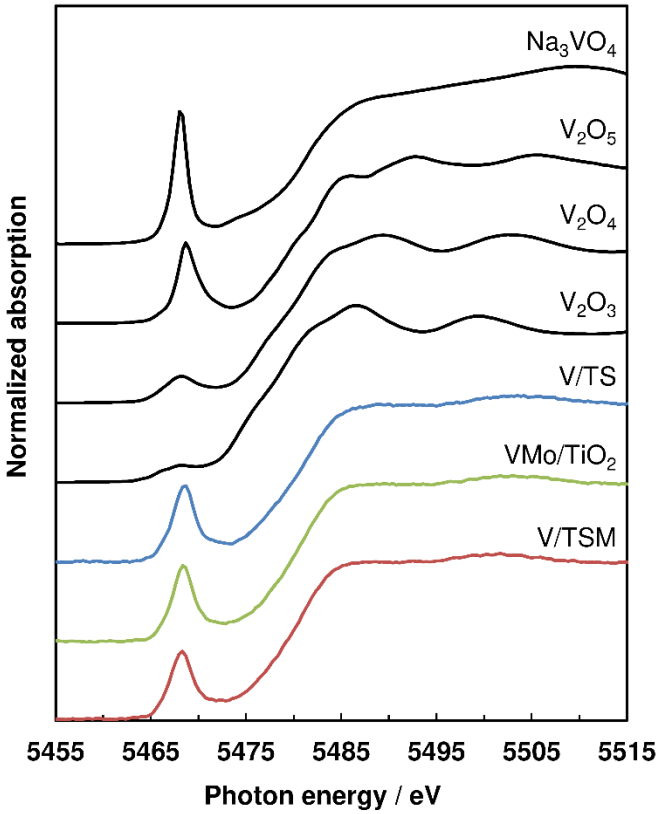

Figure 6. Normalized V K-edge XANES spectra for the reference samples and catalysts under N_2 flow at 200 °C.

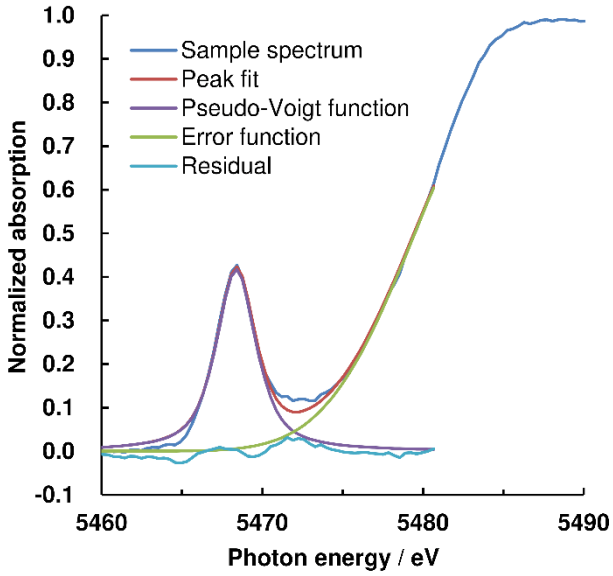

Figure 7. Fitting result for the pre-edge region of the normalized V K-edge XANES of the V/TSM catalyst under N_2 flow at 200 °C.

Table 3. Pre-edge peak heights, FWHM, positions, and main-edge positions (energy positions at 50% of normalized heights), and oxidation states determined for the reference samples and catalysts under N_2 flow at 200 °C.

Sample	Pre-edge height	Pre-edge FWHM (eV)	Relative energy positions [a)] (eV)	
			Pre-edge	Main-edge
V_2O_3	0.11	4.7	−1.0	7.6
V_2O_4	0.17	4.6	−0.5	9.8
V_2O_5	0.51	2.7	0.0	11.4
Na_3VO_4	0.83	1.7	−0.6	12.2
V/TS	0.48	3.0	−0.2	11.2
VMo/TiO_2	0.48	2.8	−0.3	11.0
V/TSM	0.40	3.0	−0.3	10.8

a) Calculated offset from the pre-edge position of V_2O_5 (approximately 5468.7 eV).

Notably, the main-edge position of VMo/TiO_2 is slightly lower than that of V/TS, indicating that molybdenum oxide can promote the reduction of the vanadium species in the catalyst. Furthermore, V/TSM exhibits an even lower oxidation state than VMo/TiO_2, suggesting that the molybdenum oxide in TSM has an enhanced effect in promoting the reduction of vanadium species.

3.5. In-situ XANES measurements during the NH_3-SCR reaction

In-situ V K-edge XANES measurements were conducted to clarify the behavior of the vanadium species during the NH_3-SCR reaction. Figure 8 displays the XANES spectra of V/TSM during the NH_3-SCR reaction at 200 °C. Immediately after the commencement of the NH_3-SCR reaction, both the absorption edge and pre-edge peaks

shift toward higher energies. Simultaneously, the pre-edge intensity evidently increases at the beginning of the reaction. These results indicate that the changes in the oxidation state and local geometry of the vanadium species in V/TSM are caused by NH_3-SCR.

The pre-edge peaks of V/TS and VMo/TiO_2 observed in the *in-situ* XANES spectra are displayed in Figure 9. With respect to the peak intensity, V/TS exhibits higher pre-edge peak intensities both before and after the reaction, indicating that the local environment of the vanadium species is more distorted. However, V/TSM demonstrates a remarkable change in the pre-edge intensity, width, and position at the beginning of the reaction, with the intensity increasing continuously during the reaction. In contrast, very small changes were observed for VMo/TiO_2.

The pre-edge of V/TSM was evidently broadened after the commencement of NH_3-SCR. The width of the pre-edge is considered to depend on the variance of the V–O distances and the valence state of the vanadium atom [40,42]; therefore, these results demonstrate that the changes in the local geometry of the vanadium species in V/TSM are more drastic than those in the other vanadium-containing catalysts.

For more information, the pre-edge heights, FWHM, positions, and main-edge positions are plotted in Figure 10 as a function of the reaction time. The data plotted at -5 min show the pre-edge peak intensity before the reaction (200 °C in N_2). After initiation of the NH_3-SCR reaction, the pre-edge height of V/TS exceeded that of V_2O_5 and increased continuously during the reaction, whereas very few changes were observed for VMo/TiO_2 throughout the *in-situ* experiment (Figure 10a).

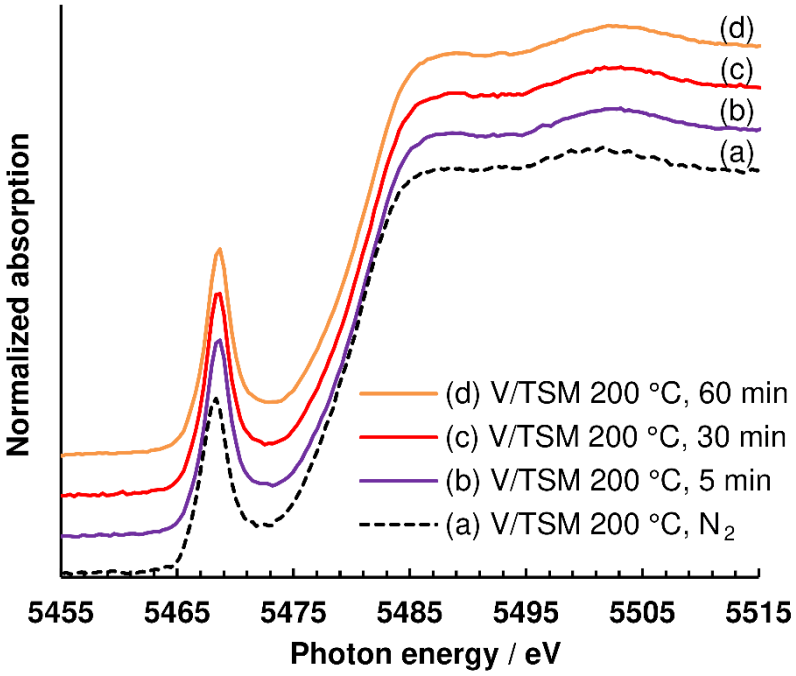

Figure 8. Normalized V K-edge *in-situ* XANES spectra for the V/TSM catalyst at different times: (a) before reaction at 200 °C in N_2, and under the reaction conditions at time on stream values of (b) 5 min, (c) 30 min, and (d) 60 min.

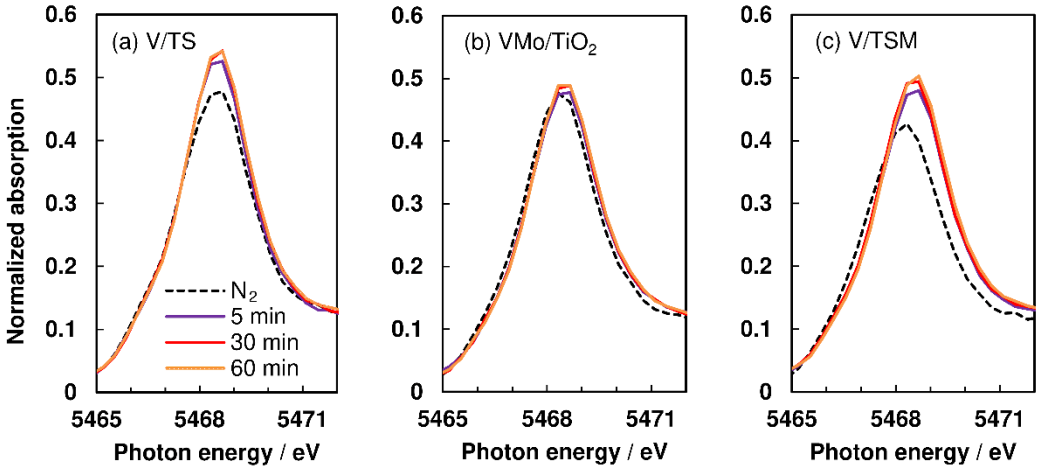

Figure 9. Magnified pre-edge region of the V K-edge *in-situ* XANES spectra for (a) V/TS, (b) VMo/TiO_2, and (c) V/TSM at 200 °C, in N_2 (dashed line) and in the reaction gas flow (solid lines).

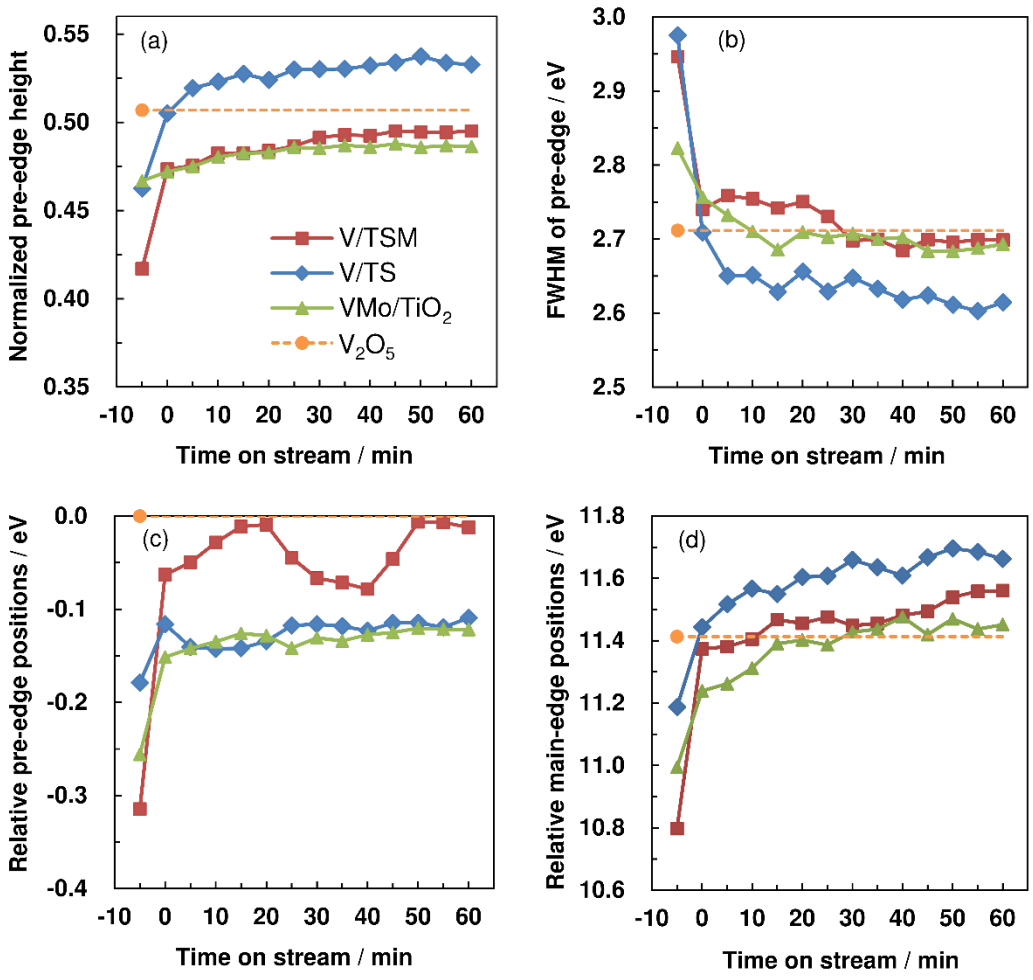

Figure 10. (a) Peak height, (b) FWHM, (c) pre-edge position, and (d) main-edge position of the normalized XANES data as a function of reaction time.

Of the three catalysts, V/TSM exhibited a lower pre-edge height than the other two catalysts under N_2 at 200 °C, and the height increased after initiation of the reaction. The pre-edge height under these reaction conditions was close to those of VMo/TiO_2 and V_2O_5 and was lower than that of V/TS until 60 min. The FWHM of the pre-edge decreased with increasing pre-edge height (Figure 10b). Consequently, V/TS exhibited a sharper pre-edge peak than the other two catalysts, and the author found that the geometry around the vanadium atom was more distorted than that observed for V_2O_5.

The pre-edge of V/TS was observed almost at the same position as that of VMo/TiO_2 during the NH_3-SCR, as well as under N_2 flow (Figure 10c). On the other hand, the pre-edge of V/TSM was observed at a lower energy than the other two under N_2 flow, and notably, the pre-edge position steeply increased to exceed those of the other two after the commencement of the reaction. The pre-edge position of V/TSM was similar to that of V_2O_5 and a slight fluctuation was observed during the reaction.

The trend in main-edge positions (Figure 10(d)) correlated with the oxidation state of the vanadium species [40]. Similar to the pre-edge peak behavior, the vanadium species of all the catalysts were rapidly oxidized at the beginning of the reaction, with continuous oxidization to a higher oxidation state.

V/TS exhibited higher oxidation states, both before and during the reaction, while V/TSM showed a significantly steep increase in the oxidation state of the vanadium species at the beginning of the reaction. In contrast to the pre-edge trend, the oxidation state of the vanadium species on V/TSM was lower than that of V/TS and slightly higher than that of VMo/TiO_2 during the reaction.

The main-edge positions of the catalysts after the reaction proceeded for 60 min were higher than that of V_2O_4 and between those of V_2O_5 and Na_3VO_4, suggesting that the oxidation states of the vanadium species in these catalysts are less than but close to +5.

Based on the data shown in Figures 9 and 10, the author can interpret the status changes observed during *in-situ* XANES as follows. Generally, the coordination geometry around the vanadium atom in a monomeric vanadate species is more distorted than that in a polymeric species [39]. The pre-edge intensity of V/TS is higher than that of crystalline V_2O_5 and lower than that of Na_3VO_4, wherein vanadium is tetrahedrally coordinated. These results imply that the vanadium species in V/TS is not completely monomeric; however, the fact that V/TS shows a relatively higher pre-edge intensity suggests the existence of a monomeric vanadate species, which is consistent with the results of the author's previous study [23].

The author had also reported the presence of a polymeric vanadate species formed on the surface of the V/TSM catalyst [23], accounting for a lower pre-edge peak than that observed for V/TS. The electronic and geometric structures of the vanadium species on V/TSM appear to be intermediate between those of V_2O_4 and V_2O_5 before the reaction. After exposure to the reaction gas, the structure around the vanadium atom is drastically modified with the oxidation of the vanadium species in V/TSM. The pre-edge intensity and FWHM of V/TSM during the reaction are similar to those of crystalline V_2O_5, suggesting the formation of vanadium species as distorted V_2O_5 under the reaction condition, and that the majority of vanadate remains as polymeric vanadate.

4. Discussion

4.1. Effects of vanadium redox properties

The physicochemical characteristics of the V/TSM catalyst, which shows superior NH_3-SCR activity at low temperatures (Figure 3), were investigated using XRD, H_2-TPR, and *in-situ* XANES, mainly focusing on the redox properties, which are closely related to the reaction cycle of the NH_3-SCR (Scheme 1). Considering the reaction mechanism shown in Scheme 1, the behaviors in H_2-TPR correspond to the reduction of V^{5+} to V^{4+} (step (b)), and the *in-situ* XANES spectra correspond to the reoxidation of V^{4+} to V^{5+} (step (d)), as suggested by the increase in the oxidation state of the vanadium species.

As the NH_3-SCR reaction is generally carried out in the temperature range 200–400 °C, reducibility at a lower temperature is important for improved catalytic activity. It has been previously proposed that the initial reduction temperature (T_{onset}) reflects the reducibility of the surface vanadium species [12,37]. Therefore, V^{5+} can be easily reduced to V^{4+} over a catalyst that shows lower T_{onset} values. Based on this, the order of reducibility derived from Table 2 is V/TSM > V/TS ≒ VMo/TiO_2.

Hence, the V^{5+} species in V/TSM should be more easily reduced to V^{4+} than those in V/TS and VMo/TiO_2 during the NH_3-SCR reaction, which is consistent with the order of NH_3-SCR activity (Figure 3). Furthermore, the trend of the relative main-edge positions in the *in-situ* XANES spectra (Section 3.5) are summarized in Table 4. The difference between the main-edge positions, before and after the reaction (represented in the brackets), follows the relationship V/TSM (+0.6) > V/TS (+0.2) = VMo/TiO_2 (+0.2). This order agrees well with the catalytic activity shown in Figure 3, indicating that the V^{4+}-to-V^{5+} reoxidation capability over V/TSM is greater than those of the other catalysts. As described above, the reoxidation step (d) in Scheme 1 is generally thought to be the

rate-determining step [33]. On the other hand, Zhu et al. [43] reported that the reduction of V^{5+} to V^{4+} (step (b) in Scheme 1) is the rate-determining step. Furthermore, Boningari et al. [44] noted that the enhanced reduction potential of vanadium species is responsible for the high NH_3-SCR activity. Hence, the contribution of the reducibility of V^{5+} in the reaction rate of NH_3-SCR should not be ruled out.

Table 4. Changes in the relative main-edge positions[a)] during the *in-situ* V K-edge XANES experiments

Sample	Before the reaction (N_2 flow at 200 °C)	At the beginning of the reaction (after 0–1 min)	After a reaction time of 60 min
V/TS	11.2	11.4	11.7
VMo/TiO_2	11.0	11.2	11.5
V/TSM	10.8	11.4	11.6

[a)] Calculated offset from the pre-edge position of V_2O_5 (~ 5468.7 eV).

Notably, while V/TS exhibits a higher vanadium oxidation state (Figure 10) than VMo/TiO_2 and V/TSM, indicating higher V^{4+} reoxidation capability, it demonstrates lower activity. As mentioned in Section 3.5, molybdenum oxide is effective in promoting the reduction of the vanadium species in the catalyst.

Furthermore, the polymeric vanadate species in V_2O_5/TiO_2 are reported to exhibit considerably greater NH_3-SCR activity [45–47] than the monomeric one. Nova et al. [47] reported that the polymeric vanadate demonstrates greater reducibility due to higher mobility of the lattice oxygen. Consequently, the lower activity of V/TS can be attributed to the lower reducibility of V^{5+}, due to the absence of molybdenum oxide and the presence of monomeric vanadate species that are less reducible than polymeric ones. In contrast,

the vanadium species on V/TSM consist mainly of polymeric vanadate, which may contribute to the higher reducibility, resulting in the remarkable catalytic activity. These findings support the author's hypothesis that the polymeric vanadate species contribute to the remarkable NH_3-SCR activity of V/TSM at low temperatures.

The presence of polymeric vanadate species in VMo/TiO_2 is also suggested. Nevertheless, this catalyst shows lower activity and reducibility (Figures 3 and 5), indicating that molybdenum oxide, which should enhance the reducibility, acts as an inhibitor by preventing the surface vanadium species from accessing H_2. The lower vanadium oxidation state during the reaction (Figure 10) may also be associated with a similar effect, whereby the reoxidation of V^{4+} is inhibited by molybdenum oxide. These trends can be attributed to lower dispersion of molybdenum oxide, as observed in the XRD results (Figure 2), due to the lower surface area of the TiO_2 support. Boningari et al. [48] reported that the NH_3-SCR activity over V/ZrO_2 catalyst was decreased by the addition of MoO_3, due to blocking of the catalyst pores. This literature strongly supports the author's hypothesis.

In this study, the H_2-TPR and XANES results confirm that V/TSM possesses higher activity for both V^{5+} reduction and V^{4+} reoxidation, indicating that the reducibility of vanadium species, as well as their reoxidation capability, is important for increasing the reactivity of NH_3-SCR at low temperatures.

4.2. Effect of physicochemical properties

The XRD and H_2-TPR results suggest that molybdenum oxide is incorporated in the TSM, wherein part of the Ti in the anatase TiO_2 structure is replaced by Mo to form a solid solution, as previously reported by the author [24]. This may indicate that the interaction between V and Mo is enhanced due to the highly dispersed molybdenum oxide

in TSM, significantly accelerating electron transfer between the vanadium species and TSM.

As shown in Scheme 1, the reduction of V^{5+} to V^{4+} is caused by gaseous NH_3, while the reoxidation of V^{4+} is caused by gaseous O_2 [34]. As described in Section 4.1, the author believes that the molybdenum oxide loaded on the catalyst surface has an inhibiting effect due to the contact of the vanadium species with such gaseous molecules. Consequently, the catalyst is required to have a designated local environment, where highly dispersed molybdenum oxide interacts with vanadium species, and the contact between vanadium species and the gaseous molecules is not inhibited.

The local structure of V/TSM is a desirable environment for the reduction and particularly, the reoxidation of vanadium species. This is because molybdenum oxide is highly dispersed in the TSM support and can easily interact with the vanadium species; such an environment has been established by the coprecipitation method. Moreover, the drastic change in V–O distances in the vanadium species on V/TSM is suggested, based on the behavior observed in the pre-edge peak shape (Figures 9 and 10). Such characteristics may be attributed to this desirable environment, where the vanadium species can change their structure without inhibition by the surface molybdates. Hence, drastic changes in the oxidation state and local structure can occur rapidly, resulting in the excellent catalytic activity of V/TSM for NH_3-SCR (Figure 3).

The author revealed that improvements in the electronic interactions between the vanadium species and support, and in the contact efficiency of the vanadium species with gaseous molecules, are important for enhancing the NH_3-SCR catalytic activity at low temperatures. By applying the author's findings to future catalyst research, including the design of surface geometries that provide easier access for gaseous molecules to reach polymeric vanadium species, the author expects to facilitate the development of catalysts

that exhibit remarkably higher NH_3-SCR activity.

5. Conclusions

The author performed XRD, H_2-TPR, and XAFS analyses to obtain information on the structure and redox behavior of a V/TSM catalyst. Both reduction of V^{5+} and reoxidation of V^{4+} were found to play important roles in realizing superior NH_3-SCR activity at low temperatures. Notably, XANES was proven to be a suitable tool for the *in-situ* study of the oxidation state and local geometry of vanadium-containing catalysts during the NH_3-SCR reaction. The incorporated molybdenum oxide promoted the V^{5+}-to-V^{4+} reduction, particularly when vanadium oxide was supported on a TSM solid solution. Furthermore, the XANES spectra suggested a remarkably higher V^{4+}-to-V^{5+} reoxidation capability over V/TSM. These results enabled the author to confirm that the acceleration of the reduction of V^{5+} as well as the reoxidation of V^{4+} are essential for improving catalytic performance. This improved redox reactivity was found to be induced by the interaction of the highly dispersed polymeric vanadate with molybdenum, and by the appropriate surface geometry of the vanadium species for promoting contact with gaseous NH_3 and O_2. These desirable characteristics of the species can be attributed to the TSM solid solution structure, wherein molybdenum oxide is intimately incorporated into the anatase-TiO_2 structure. The relationship between the NH_3-SCR catalytic activity and redox behavior, as well as the local structure around the vanadium species, was successfully investigated in this study. The results from the present study were insightful and confirmed that *in-situ* XANES is a significant tool for analyzing these kinds of catalytic reactions. However, more data is needed to elucidate the detailed relationship between catalytic activity and physicochemical properties. Additional experiments over

other catalysts and *in-situ* XAFS studies should be conducted under conditions different from those reported herein, for the development of new catalysts with higher activity.

Acknowledgment

The author acknowledges Dr. K. Kimijima (High Energy Accelerator Research Organization, KEK) for helpful assistance and valuable discussions on the XAFS experiments. He also gratefully acknowledges Nippon Shokubai Co., Ltd. for funding and permission to publish this article.

References

[1] L. Lietti, J. Svachula, P. Forzatti, G. Busca, G. Ramis, P. Bregani, *Catal. Today* **1993**, *17*, 131–139.

[2] G. Busca, L. Lietti, G. Ramis, F. Berti, *Appl. Catal. B Environ.* **1998**, *18*, 1–36.

[3] M. Kobayashi, R. Kuma, S. Masaki, N. Sugishima, *Appl. Catal. B Environ.* **2005**, *60*, 173–179.

[4] J. M. Herrmann, J. Disdier, *Catal. Today* **2000**, *56*, 389–401.

[5] I. Giakoumelou, C. Fountzoula, C. Kordulis, S. Boghosian, *J. Catal.* **2006**, *239*, 1–12.

[6] S. T. Choo, Y. G. Lee, I.-S. Nam, S.-W. Ham, J.-B. Lee, *Appl. Catal. A Gen.* **2000**, *200*, 177–188.

[7] B. Shen, F. Wang, B. Zhao, Y. Li, Y. Wang, *J. Ind. Eng. Chem.* **2016**, *33*, 262–269.

[8] M. Kobayashi, M. Hagi, *Appl. Catal. B Environ.* **2006**, *63*, 104–113.

[9] P. G. W. A. Kompio, A. Brückner, F. Hipler, G. Auer, E. Löffler, W. Grünert, *J. Catal.* **2012**, *286*, 237–247.

[10] M. A. Vuurman, I. E. Wachs, A. M. Hirt, *J. Phys. Chem.* **1991**, *95*, 9928–9937.

[11] M. Zhu, J. K. Lai, U. Tumuluri, Z. Wu, I. E. Wachs, *J. Am. Chem. Soc.* **2017**, *139*, 15624–15627.

[12] L. Casagrande, L. Lietti, I. Nova, P. Forzatti, A. Baiker, *Appl. Catal. B Environ.* **1999**, *22*, 63–77.

[13] R. Wu, N. Zhang, L. Li, H. He, L. Song, W. Qiu, *Catalysts* **2018**, *8*, 143.

[14] P. G. Smirniotis, D. A. Peña, B. S. Uphade, *Angew. Chemie Int. Ed.* **2001**, *40*, 2479–2482.

[15] P. M. Sreekanth, D. A. Peña, P. G. Smirniotis, *Ind. Eng. Chem. Res.* **2006**, *45*, 6444–6449.

[16] T. Boningari, P. R. Ettireddy, A. Somogyvari, Y. Liu, A. Vorontsov, C. A. McDonald, P. G. Smirniotis, *J. Catal.* **2015**, *325*, 145–155.

[17] C. Liu, J.-W. Shi, C. Gao, C. Niu, *Appl. Catal. A Gen.* **2016**, *522*, 54–69.

[18] T. Boningari, P. G. Smirniotis, *Curr. Opin. Chem. Eng.* **2016**, *13*, 133–141.

[19] T. Boningari, D. K. Pappas, P. G. Smirniotis, *J. Catal.* **2018**, *365*, 320–333.

[20] C. Gao, J.-W. Shi, Z. Fan, G. Gao, C. Niu, *Catalysts* **2018**, *8*, 11.

[21] D. Damma, P. R. Ettireddy, B. M. Reddy, P. G. Smirniotis, *Catalysts* **2019**, *9*, 349.

[22] S. Xie, L. Li, L. Jin, Y. Wu, H. Liu, Q. Qin, X. Wei, J. Liu, L. Dong, B. Li, *Appl. Surf. Sci.* **2020**, *515*, 146014.

[23] M. Kobayashi, R. Kuma, A. Morita, *Catal. Letters* **2006**, *112*, 37–44.

[24] R. Kuma, T. Kitano, T. Tsujiguchi, T. Tanaka, *Appl. Catal. A Gen.* **2020**, *595*, 117496.

[25] M. Ruitenbeek, F. M. F. de Groot, A. J. van Dillen, D. C. Koningsberger, in *Top. Catal.*, **2000**, pp. 241–254.

[26] A. M. Beale, I. Lezcano-Gonzalez, T. Maunula, R. G. Palgrave, *Catal. Struct. React.* **2015**, *1*, 25–34.

[27] W. C. Vining, J. Strunk, A. T. Bell, *J. Catal.* **2012**, *285*, 160–167.

[28] A. Burkardt, W. Weisweiler, T. J.A.A. van den, A. Schäfer-Sindlinger, E. S. Lox, *Top. Catal.* **2001**, *16*, 369–375.

[29] D. E. Doronkin, M. Casapu, T. Günter, O. Müller, R. Frahm, J.-D. Grunwaldt, *J. Phys. Chem. C* **2014**, *118*, 10204–10212.

[30] D. E. Doronkin, F. Benzi, L. Zheng, D. I. Sharapa, L. Amidani, F. Studt, P. W. Roesky, M. Casapu, O. Deutschmann, J.-D. Grunwaldt, *J. Phys. Chem. C* **2019**, *123*, 14338–14349.

[31] Y. Inomata, S. Hata, M. Mino, E. Kiyonaga, K. Morita, K. Hikino, K. Yoshida, H. Kubota, T. Toyao, K. Shimizu, M. Haruta, T. Murayama, *ACS Catal.* **2019**, *9*, 9327–9331.

[32] Y. Qiu, B. Liu, J. Du, Q. Tang, Z. Liu, R. Liu, C. Tao, *Chem. Eng. J.* **2016**, *294*, 264–272.

[33] A. Marberger, D. Ferri, M. Elsener, O. Kröcher, *Angew. Chemie Int. Ed.* **2016**, *55*, 11989–11994.

[34] L. Lietti, P. Forzatti, F. Bregani, *Ind. Eng. Chem. Res.* **1996**, *35*, 3884–3892.

[35] G. Ramis, G. Busca, F. Bregani, P. Forzatti, *Appl. Catal.* **1990**, *64*, 259–278.

[36] L. Lietti, I. Nova, G. Ramis, L. Dall'Acqua, G. Busca, E. Giamello, P. Forzatti, F. Bregani, *J. Catal.* **1999**, *187*, 419–435.

[37] X. T. Gao, S. R. Bare, J. L. G. Fierro, I. E. Wachs, *J. Phys. Chem. B* **1999**, *103*, 618–629.

[38] F. Amano, T. Tanaka, *Catal. Commun.* **2005**, *6*, 269–273.

[39] P. A. Kumar, Y. E. Jeong, S. Gautam, H. P. Ha, K. J. Lee, K. H. Chae, *Chem. Eng. J.* **2015**, *275*, 142–151.

[40] J. Wong, F. W. Lytle, R. P. Messmer, D. H. Maylotte, *Phys. Rev. B* **1984**, *30*, 5596–5610.

[41] S. Yoshida, T. Tanaka, T. Hanada, T. Hiraiwa, H. Kanai, T. Funabiki, *Catal. Letters* **1992**, *12*, 277–285.

[42] T. Tanaka, H. Yamashita, R. Tsuchitani, T. Funabiki, S. Yoshida, *J. Chem. Soc. Faraday Trans. 1 Phys. Chem. Condens. Phases* **1988**, *84*, 2987.

[43] M. Zhu, J. K. Lai, U. Tumuluri, M. E. Ford, Z. Wu, I. E. Wachs, *ACS Catal.* **2017**, *7*, 8358–8361.

[44] T. Boningari, R. Koirala, P. G. Smirniotis, *Appl. Catal. B Environ.* **2013**, *140–141*, 289–298.

[45] G. T. Went, L.-J. Leu, R. R. Rosin, A. T. Bell, *J. Catal.* **1992**, *134*, 492–505.

[46] L. Lietti, P. Forzatti, *J. Catal.* **1994**, *147*, 241–249.

[47] I. Nova, L. Dall'Acqua, L. Lietti, E. Giamello, P. Forzatti, *Appl. Catal. B Environ.* **2001**, *35*, 31–42.

[48] T. Boningari, R. Koirala, P. G. Smirniotis, *Appl. Catal. B Environ.* **2012**, *127*, 255–264.

Chapter 5

Deactivation Mechanism and Enhanced Durability of V_2O_5/TiO_2–SiO_2–MoO_3 Catalysts for NH_3-SCR in the Presence of SO_2

Abstract

V_2O_5/TiO_2-type catalysts are widely applied for selective catalytic NO reduction by NH_3 (NH_3-SCR), but enhanced sulfur tolerance and low-temperature activity are required. Herein, V_2O_5/TiO_2–SiO_2–MoO_3 (V/TSM) was demonstrated to have excellent catalytic activity and durability for NH_3-SCR in the presence of SO_2 at temperatures lower than 200 °C. The deactivation mechanism and factors influencing SO_2 durability were investigated using catalytic durability tests, Fourier-transform infrared spectroscopy, and temperature-programmed desorption/decomposition. The author's results revealed that $(NH_4)_2S_2O_3$ and NH_4HSO_4 form on catalyst surfaces by NH_3–SO_2–H_2O reactions at low temperatures, resulting in catalyst deactivation via pore blockage. However, V/TSM was found to possess an increased number of active sites for decomposing deposited ammonium sulfate salts. The decomposition activity was related to the solid acidity, which enhanced SO_2 desorption and reactions between ammonium sulfate salts and NO. These findings will contribute to the development of catalysts with improved lifetimes for NH_3-SCR.

1. Introduction

To control emissions from stationary sources, such as power plants, V_2O_5/TiO_2-type catalysts have been widely employed for selective catalytic NO_x (NO and NO_2) reduction using ammonia as a reductant (NH_3-SCR) [1–12]. Numerous studies have examined V_2O_5–WO_3/TiO_2 [13–23] and V_2O_5–MoO_3/TiO_2 [24–30] as catalysts for NH_3-SCR, where WO_3 or MoO_3 is added to promote the catalytic activity.

The sulfur tolerance of such catalysts is important because sulfur oxides are generally present in the flue gas, and the adhesion of SO_3 formed by SO_2 oxidation can result in apparatus corrosion [31]. In addition, it is known that the deactivation of NH_3-SCR catalysts is caused by the accumulation of ammonium sulfate compounds such as NH_4HSO_4 (ammonium bisulfate, ABS) and $(NH_4)_2SO_4$ (ammonium sulfate, AS) [32–35], which block the catalyst pores. These compounds can be considered to form via the following reactions [36,37]:

$$SO_2 + 1/2O_2 \rightarrow SO_3 \cdots\cdots (1)$$

$$NH_3 + SO_3 + H_2O \rightarrow NH_4HSO_4 \cdots\cdots (2)$$

$$2NH_3 + SO_3 + H_2O \rightarrow (NH_4)_2SO_4 \cdots\cdots (3)$$

Therefore, to avoid deactivation through these reactions, de-NO_x catalysts with lower SO_2 oxidation activities are required. As tungsten and molybdenum can suppress the SO_2 oxidation activity, the addition of WO_3 or MoO_3 may also improve the sulfur tolerance of NH_3-SCR catalysts [14,19,29,30].

However, the flue gas temperature, for example, from a municipal incinerator, tends to be lower than 200 °C because the catalyst is placed downstream from an

electrostatic precipitator or a bag filter. Therefore, catalysts with improved activities at low temperatures are also desirable. Manganese-based catalysts such as Mn–Ce/TiO_2 are also known to exhibit high activity at temperatures lower than 180 °C [38–45]. However, the V_2O_5/TiO_2-type catalysts are commonly applied for commercial waste gas treatments, as they exhibit good durability in the presence of SO_2.

For V_2O_5/TiO_2-type catalysts, it is known that MoO_3 is a more effective promoter than WO_3 at low temperatures for both, catalytic activity and durability [29,46]. However, further improvements of V_2O_5–MoO_3/TiO_2-type catalysts are required for industrial use. The author has previously reported that a vanadium catalyst supported on TiO_2–SiO_2–MoO_3 prepared by coprecipitation (V/TSM) shows significantly enhanced activity at low temperatures [47]. This catalyst exhibits improved SO_2 durability at very low temperatures, such as 175 °C; however, the deactivation mechanism and the factors responsible for the high SO_2 durability have not been clarified.

Although catalyst deactivation by SO_2 is generally accelerated at low temperatures [36], SO_2 conversion to SO_3 tends to be reduced at low temperatures and is almost 0% at temperatures lower than 200 °C [26]. Thus, Equations (1)–(3) are not sufficient to explain the deactivation mechanism at low temperatures. However, very few studies have investigated this issue. Wang et al. suggested the possibility of NH_3–SO_2–H_2O reactions at low temperatures using density functional theory (DFT) calculations, claiming that a Ti–O–S bond is associated with ABS formation [48]. Zhu et al. studied V_2O_5–Nb_2O_5/WO_3–TiO_2 catalysts deactivated at 175 °C using Fourier-transform infrared (FT-IR) spectroscopy [49]. By comparing FT-IR spectra, they concluded that the formation of ammonium sulfate salts was the main reason for catalyst deactivation. However, no specific reactions for the formation of these salts were proposed. Thus, the deactivation mechanism at temperatures lower than 200 °C remains unclear.

In this study, the author reports the NH_3-SCR activity and durability of V/TSM in the presence of SO_2. Moreover, the deactivation mechanism and the factors affecting the SO_2 durability are discussed, based on FT-IR spectroscopy, diffuse reflectance infrared Fourier transform spectroscopy (DRIFTS), temperature-programmed desorption of NH_3 or SO_2 (NH_3- or SO_2-TPD), and temperature-programmed decomposition (TPDC).

2. Results and Discussion

2.1. NH_3-SCR Activity and SO_2 Durability

The NH_3-SCR activity and durability of three catalysts including vanadium and molybdenum oxides (V–Mo catalysts) were tested in the presence of SO_2 at 200 or 175 °C (Figure 1). VMo/TS and V/TSM are both commercially employed catalysts that have been developed based on the conventional VMo/TiO_2 catalyst. As the author reported previously, among these V–Mo catalysts, V/TSM exhibits a superior NH_3-SCR activity at low temperatures owing to improved reducibility and reoxidizability between V^{4+} and V^{5+} in polymeric vanadates on the catalyst surface [47,50].

While slight differences were observed in the initial activities at 200 °C, all the catalysts exhibited almost constant conversions until 400 h. By contrast, the catalytic activity of VMo/TiO_2 quickly deteriorated at 175 °C. V/TSM exhibited both superior durability and a higher initial catalytic activity, whereas the durability of VMo/TS was intermediate between those of VMo/TiO_2 and V/TSM. Throughout all the catalytic activity and durability tests, no other components such as N_2O or NO_2 were observed in the outlet gas of the reactor, indicating that the N_2 selectivity was almost 100%.

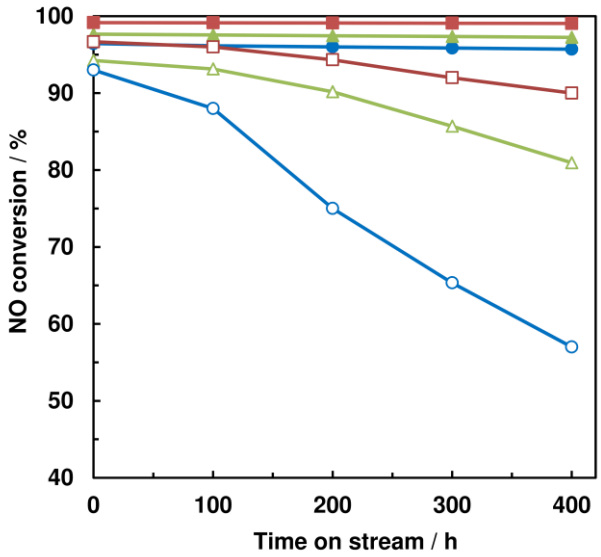

Figure 1. NH_3-SCR activities at 200 °C (filled symbols) and 175 °C (open symbols) of V/TSM (squares), VMo/TS (triangles), and VMo/TiO_2 (circles). Reaction conditions: 100 ppm NO, 100 ppm NH_3, 150 ppm SO_2, 10 vol% O_2, 10 vol% H_2O, N_2 balance, GHSV: 6,000 h^{-1} for the activity tests; for the durability tests, the NH_3 concentration was changed to 80 ppm.

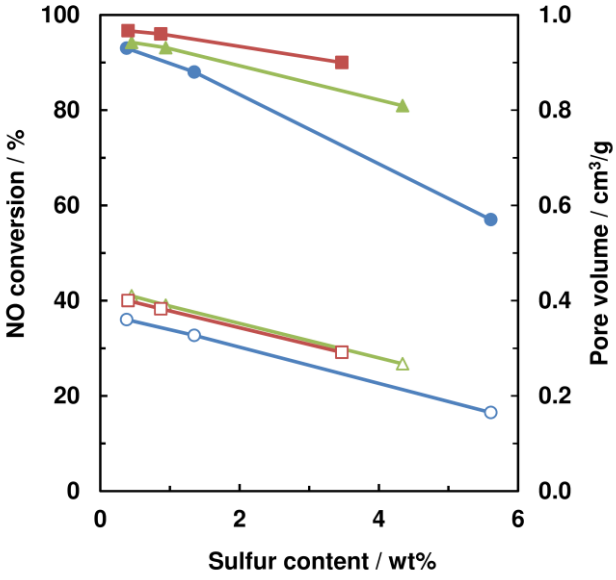

Figure 2. NH_3-SCR activities (filled symbols) and pore volumes (open symbols) of V/TSM (squares), VMo/TS (triangles), and VMo/TiO_2 (circles) at 175 °C as a function of sulfur content.

The sulfur contents before and after the SO_2 durability tests at 200 and 175 °C are shown in Table 1. A small amount of sulfur was contained in each catalyst before the reaction (fresh catalysts), which originated from the starting material titanyl sulfate. When NH_3-SCR was performed in the presence of SO_2 at 200 °C, sulfur accumulated on each catalyst, with the amount increasing over time. Furthermore, when the reaction was performed at 175 °C, a greater amount of sulfur was deposited, with sulfur accumulation increasing in the following order: V/TSM < VMo/TS < VMo/TiO_2. NO conversion and the catalyst pore volume as a function of the sulfur content are shown in Figure 2. A decrease in pore volume with increasing sulfur content was accompanied by catalyst deactivation, confirming that pore blocking is a major cause of deactivation. As shown in Table 1, the Brunauer–Emmett–Teller (BET) specific surface areas of the V–Mo catalysts also decreased in accordance with their sulfur contents. Notably, sulfur accumulation and pore blocking were significantly suppressed on the V/TSM catalyst, contributing to its high durability. To further investigate the accumulated sulfur compounds, the author characterized the used catalysts with FT-IR spectroscopy.

Table 1. Sulfur contents (as sulfur atom) and pore volumes of the V–Mo catalysts before and after SO_2 durability tests.

		Fresh catalyst	Used catalyst			
Time on stream (h)		0	100	400	100	400
Reaction temperature (°C)		-	200	200	175	175
Sulfur content (wt%)	VMo/TiO_2	0.29	0.44	0.59	1.35	5.61
	VMo/TS	0.40	0.49	0.65	0.94	4.34
	V/TSM	0.45	0.44	0.59	0.87	3.47
Pore volume (cm^3/g)	VMo/TiO_2	0.36	0.36	0.35	0.33	0.16
	VMo/TS	0.41	0.40	0.40	0.39	0.27
	V/TSM	0.40	0.40	0.40	0.38	0.29
Specific surface area (m^2/g)	VMo/TiO_2	60	55	53	45	13
	VMo/TS	111	102	99	93	39
	V/TSM	101	93	90	85	45

2.2. FT-IR Analysis of Accumulated Sulfur Compounds

The FT-IR spectra of the catalysts before and after the NH_3-SCR reactions are displayed in Figure 3. During NH_3-SCR, the catalysts were exposed to a reaction gas including SO_2 at 200, 175, or 160 °C for 400 h. The spectra of all the samples exhibited bands at 1630 cm^{-1}, which was assigned to adsorbed H_2O. A broad band in the range of 1000–1200 cm^{-1} with a maximum at approximately 1102 cm^{-1} was observed for the fresh VMo/TS catalyst. This peak was attributed to free SO_4^{2-} [33], resulting from residual sulfate species derived from titanyl sulfate (Table 1).

For both VMo/TS and V/TSM, sharp peaks at 1400 cm^{-1} corresponding to the N–H stretching vibrations of adsorbed NH_4^+ [33,51] were observed in the spectra of the used catalysts. In both cases, the catalysts used at 200 °C exhibited peaks at 975, 1042, and 1136 cm^{-1} with a shoulder peak at 1220 cm^{-1}. The intensities of these peaks increased at 160 °C, and new bands at 1179 cm^{-1} appeared for the catalysts used at 175 and 160 °C. These results indicate that the surface species on the catalysts used at temperatures lower than 175 °C are different from those on the catalyst used at 200 °C. This phenomenon was observed for all the catalysts, despite their differences in SO_2 durability.

Subsequently, to aid in identifying the accumulated sulfur compounds, aqueous solutions of various sulfur- and ammonium-containing salts were added to the fresh V/TSM catalyst, and FT-IR analyses were performed after drying at 120 °C in air. The FT-IR spectra of V/TSM after the addition of the salts are shown in Figure 4. Hereafter, these samples are denoted as “salt/V/TSM”.

For all the samples, a band with a maximum at 1400 cm^{-1} assigned to NH_4^+ was observed. A peak at 1110 cm^{-1} assigned to free SO_4^{2-} was predominant for $(NH_4)_2SO_4$/V/TSM, as also observed for the fresh catalyst (Figure 3).

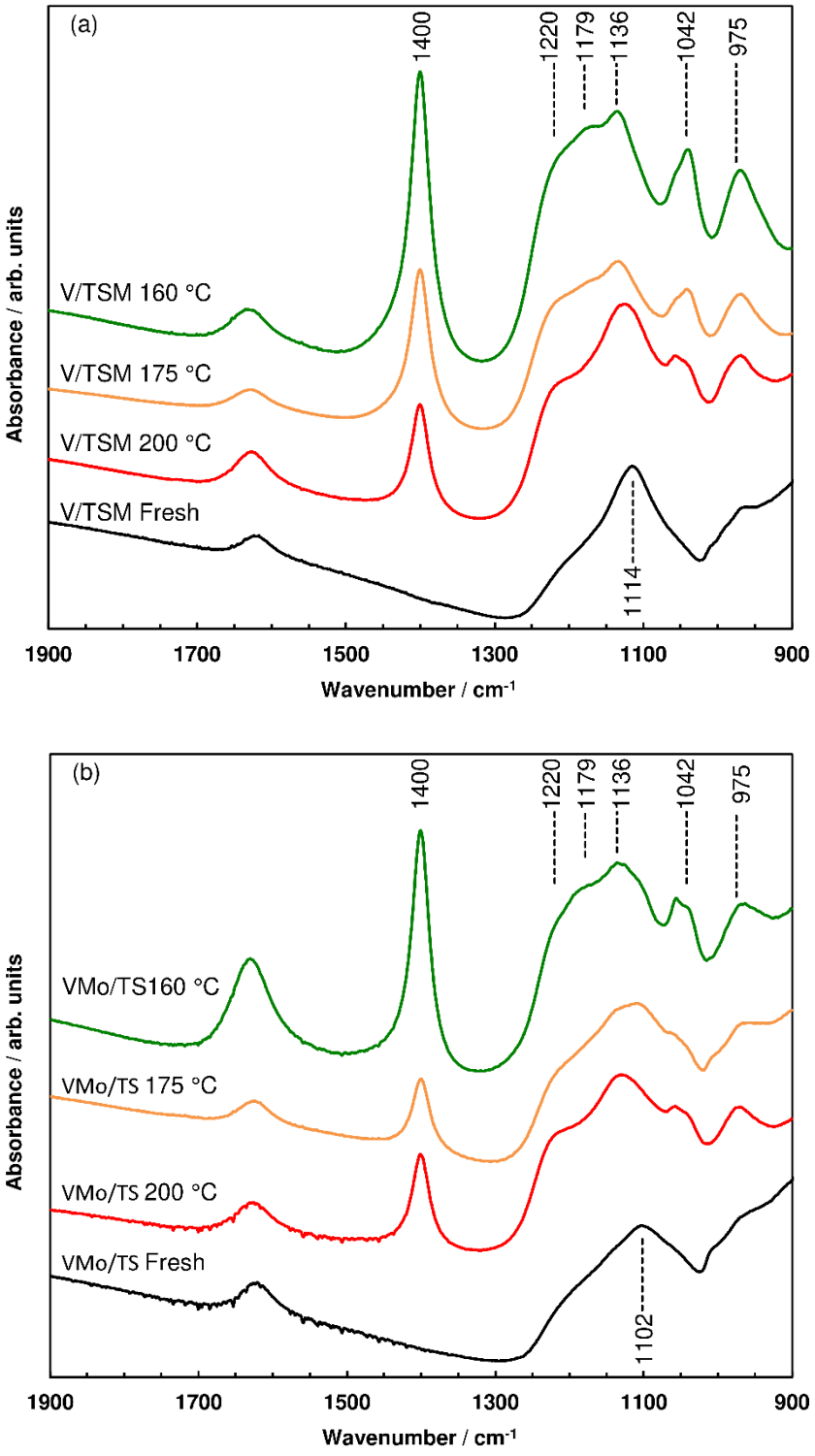

Figure 3. FT-IR spectra of fresh catalysts and catalysts used for 400 h at various temperatures: (a) V/TSM and (b) VMo/TS.

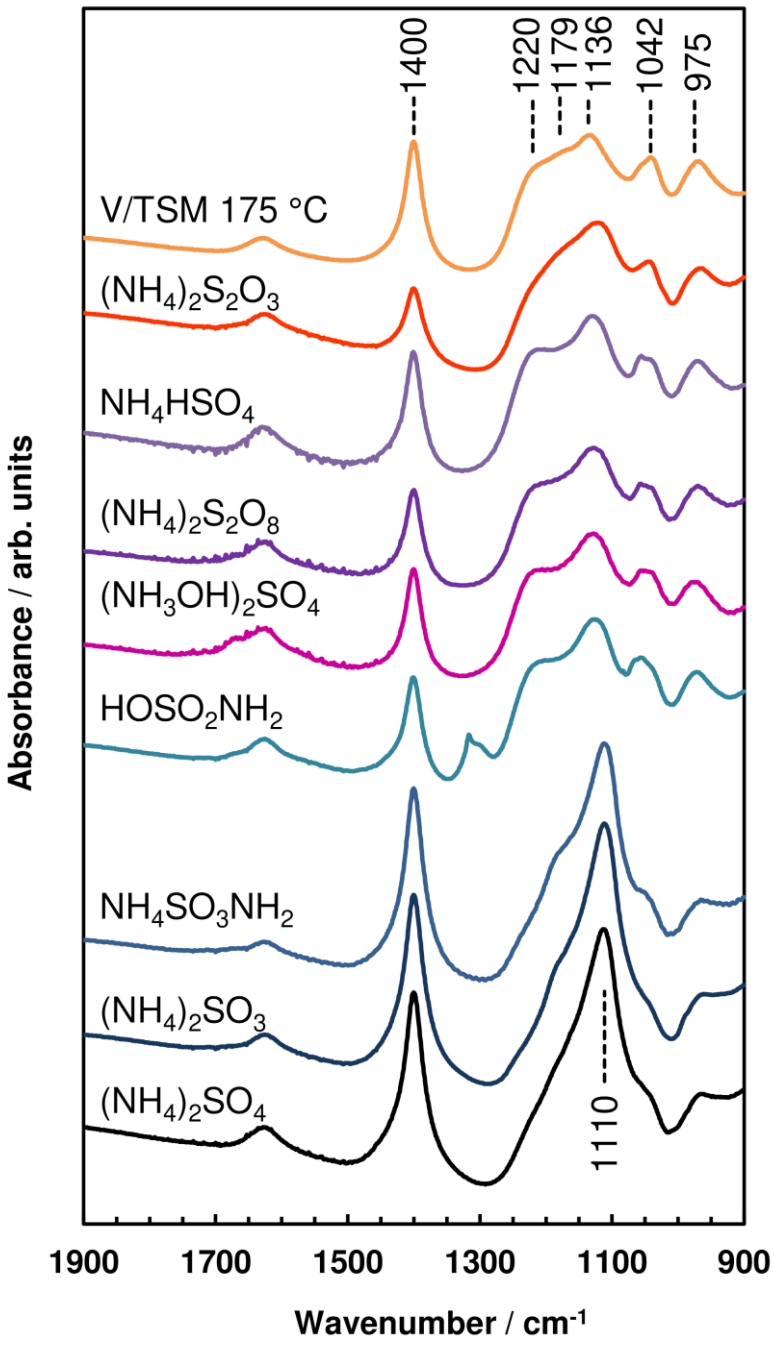

Figure 4. FT-IR spectra of the fresh V/TSM catalyst impregnated with various sulfur- and ammonium-containing compounds. For comparison, the spectrum of the V/TSM catalyst used at 175 °C is also displayed.

$(NH_4)_2SO_3$/V/TSM and $NH_4SO_3NH_2$/V/TSM exhibited spectra similar to that of $(NH_4)_2SO_4$/V/TSM, indicating that these salts were mostly converted to $(NH_4)_2SO_4$ at 120 °C in air. However, these spectra were fundamentally different from those of the used catalysts. $HOSO_2NH_2$/V/TSM exhibited a spectrum similar to those of the used catalysts. However, a weak but distinct peak was observed at 1315 cm^{-1} for $HOSO_2NH_2$/V/TSM, implying that $HOSO_2NH_2$ was not present on the used catalysts.

The spectra of NH_4HSO_4/V/TSM, $(NH_4)_2S_2O_8$/V/TSM, and $(NH_3OH)_2SO_4$/V/TSM were very similar. Thus, $(NH_4)_2S_2O_8$ and $(NH_3OH)_2SO_4$ on the V/TSM catalyst likely decompose to form NH_4HSO_4 at 120 °C in air. The V/TSM catalyst used at 200 °C exhibited a spectrum similar to that of NH_4HSO_4/V/TSM, which is consistent with the deactivation mechanism reported by other research groups [32–35]. However, the characteristic band at 1179 cm^{-1} observed for the catalysts used at 175 or 160 °C was not observed for NH_4HSO_4/V/TSM.

The spectrum of $(NH_4)_2S_2O_3$/V/TSM exhibited bands at 975, 1042, and 1136 cm^{-1}. Notably, a shoulder peak at 1179 cm^{-1} was also observed. Newman reported that the IR spectra of copper-thiosulfato compounds exhibit bands at 1182 and 1140 cm^{-1}, and concluded that these bands are associated with the S–O vibrations of S_2O_3 groups that are distorted by metal–ligand interactions [52]. Thus, the peak observed for $(NH_4)_2S_2O_3$/V/TSM at 1179 cm^{-1} can be assigned to the asymmetric S–O vibrations of S_2O_3 groups interacting with the catalyst. From these results, it can be concluded that the band observed in the FT-IR spectra of the used catalysts at temperatures lower than 175 °C is indicative of the formation of $(NH_4)_2S_2O_3$ (ammonium thiosulfate, ATS) on the catalysts.

2.3. Deactivation Mechanism at Low Temperatures

As described above, almost no SO_2 oxidation proceeds at low temperatures; therefore, ABS and AS cannot be formed by Equations (1)–(3). As examples of other ammonium sulfates, NH_4HSO_3 and $(NH_4)_2SO_3$ could potentially be formed via the direct reactions of SO_2 with NH_3 and H_2O, as follows:

$$NH_3 + SO_2 + H_2O \rightarrow NH_4HSO_3 \cdots\cdots (4)$$

$$2NH_3 + SO_2 + H_2O \rightarrow (NH_4)_2SO_3 \cdots\cdots (5)$$

However, the FT-IR spectrum of $(NH_4)_2SO_3$/V/TSM was distinct from those of the used catalysts (Figure 4). As these compounds are unstable, they will be easily decomposed, even at temperatures lower than 200 °C; therefore, they cannot be the main reason for deactivation. By contrast, the author has verified that ATS is formed at low temperatures (Figure 4). Kim et al. reported that ATS is formed from sulfur atoms or H_2S through Equations (6) or (7) [53].

$$(NH_4)_2SO_3 + S \rightarrow (NH_4)_2S_2O_3 \cdots\cdots (6)$$

$$3(NH_4)_2SO_3 + SO_2 + 2H_2S \rightarrow 3(NH_4)_2S_2O_3 \cdots\cdots (7)$$

However, as oxygen is present in the NH_3-SCR reaction gas feed, little S or H_2S can be formed. Consequently, the author suggests that reactions such as the following are likely to proceed to form ATS from NH_3, SO_2, and H_2O.

$$4NH_3 + 4SO_2 + 3H_2O \rightarrow (NH_4)_2S_2O_3 + 2NH_4HSO_4 \cdots\cdots (8)$$

$$6NH_3 + 4SO_2 + 3H_2O \rightarrow (NH_4)_2S_2O_3 + 2(NH_4)_2SO_4 \cdots\cdots (9)$$

As the band at approximately 1110 cm^{-1}, corresponding to free SO_4^{2-}, is not predominant in the FT-IR spectra of the catalysts used at temperatures lower than 175 °C (Figure 3), Equation (8) is likely the main route for $(NH_4)_2S_2O_3$ formation.

Hence, the formation of $(NH_4)_2S_2O_3$, as well as NH_4HSO_4, is one of the causes of catalyst deactivation. To the best of the author's knowledge, this is a new insight into the deactivation mechanism during NH_3-SCR at low temperatures. However, as both VMo/TS and V/TSM exhibit a peak at 1179 cm^{-1} when used at temperatures lower than 175 °C, $(NH_4)_2S_2O_3$ formation is not responsible for the enhanced durability of V/TSM. Thus, based on Equations (8) and (9), the author performed NH_3-TPD and SO_2-TPD experiments to investigate the factors that affect the durability.

2.4. NH_3-TPD and DRIFTS

The NH_3-TPD profiles of V/TSM, VMo/TS, and VMo/TiO_2 are shown in Figure 5. In this experiment, the desorption of not only NH_3 but also N_2 was observed owing to NH_3 decomposition by the catalyst. The signals at m/z = 16 and 28 were monitored for NH_3 and N_2, respectively. An NH_3 desorption peak with a maximum at 200 °C and two N_2 formation peaks at approximately 200 and 400 °C were observed for each catalyst.

The desorption amounts of NH_3 (A_{NH3}) and N_2 (A_{N2}) as well as the total adsorption amount of NH_3 (A_{total}) for each catalyst are shown in Table 2. A_{total}, which was estimated using the following equation: $A_{total} = A_{NH3} + 2 \times A_{N2}$, decreased in the following order: V/TSM > VMo/TS > VMo/TiO_2. In particular, V/TSM exhibited 1.5 times greater NH_3 adsorption than VMo/TiO_2.

A_{total} corresponds to the acidity of the catalyst; thus, the NH_3 adsorption amount per specific surface area was calculated as an index of acid site density [54]. The TiO_2–SiO_2 (TS) mixed oxide is known to be a solid acid [8,55], and its acidity is enhanced by the

presence of approximately 0.5 wt% sulfate [56]. The amount of sulfate included in TSM is similar to that in TS. The author has reported that TSM forms a solid solution [57], which should also contribute to a greater solid acidity. Thus, the acidities of the catalysts varied depending on these differences in the solid acidities of the support materials. Additionally, V/TSM exhibited a higher acid site density than VMo/TS, which had a higher specific surface area (Table 1), indicating that the incorporation of Mo into TS increases the acid site density.

Further, a DRIFTS analysis of adsorbed pyridine was attempted to determine the contributions of Brønsted and Lewis acidity in V/TSM (Figure 6). The peak at 1537 cm^{-1} was assigned to protonated pyridine derived from interactions with Brønsted acid sites, whereas that at 1448 cm^{-1} correspond to pyridine coordinated to Lewis acid sites [58–60]. The DRIFTS data indicated that Brønsted acid sites are predominant on the V/TSM surface, along with a smaller amount of Lewis acid sites.

Table 2. Amounts of NH_3 desorbed (A_{NH3}), N_2 formed (A_{N2}), and NH_3 adsorbed (A_{total}) during NH_3-TPD experiments.

	A_{NH3}	A_{N2}	A_{total}[a]	
	($\mu mol \cdot g^{-1}$)	($\mu mol \cdot g^{-1}$)	($\mu mol \cdot g^{-1}$)	($\mu mol \cdot m^{-2}$)
VMo/TiO_2	878	320	1519	25.3
VMo/TS	1048	486	2020	18.2
V/TSM	1143	546	2234	22.1

[a] Calculated using the equation $A_{total} = A_{NH3} + 2 \times A_{N2}$ ($\mu mol \cdot g^{-1}$), and then divided by the specific surface area ($\mu mol \cdot m^{-2}$).

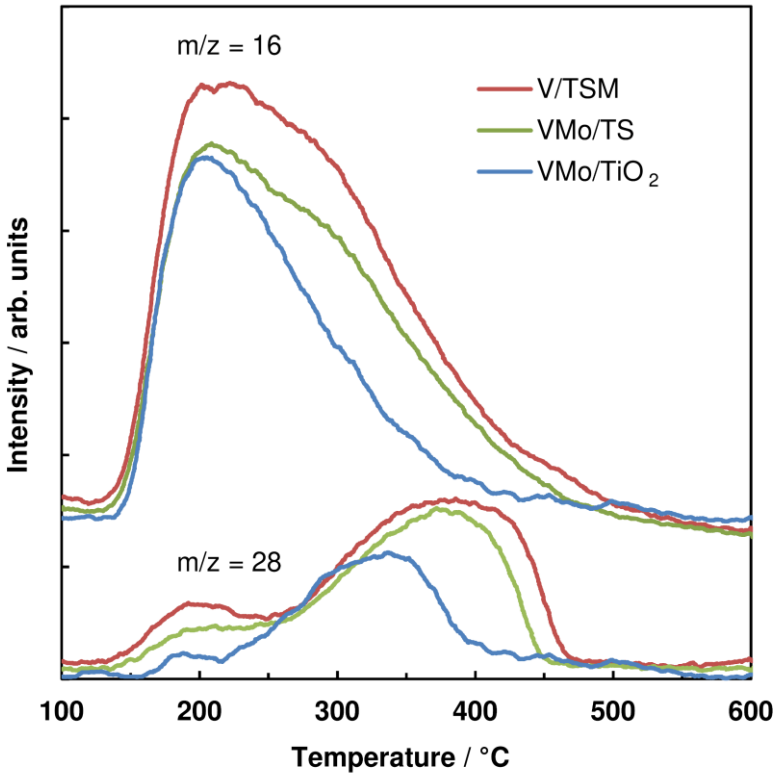

Figure 5. NH_3-TPD profiles of V/TSM, VMo/TS, and VMo/TiO_2.

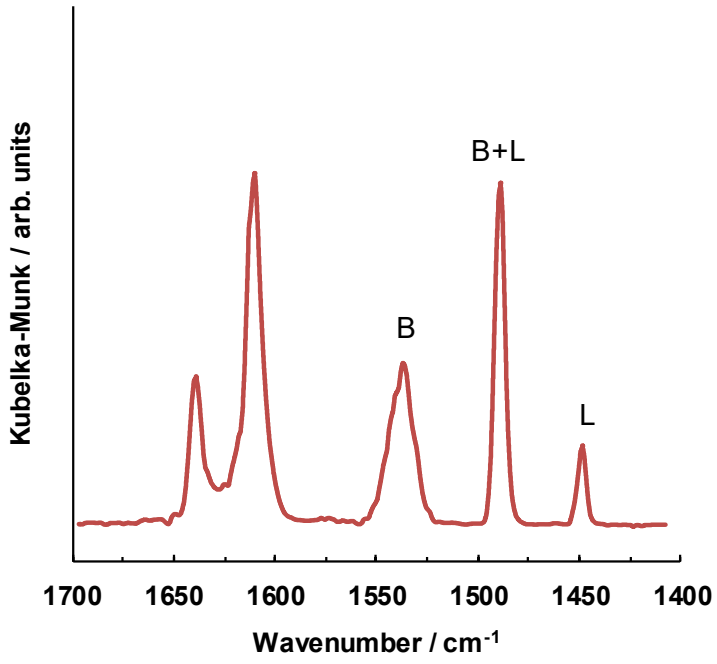

Figure 6. DRIFTS spectrum of pyridine adsorbed on V/TSM.

2.5. SO_2-TPD

Figure 7(a) shows the TPD profiles for the adsorption of SO_2 on V/TSM, VMo/TS, and VMo/TiO_2 at 160 °C. The signal at m/z = 64 was employed as the index for SO_2 desorption. As the catalysts contain sulfur originating from titanyl sulfate (Table 1), SO_2 desorption was observed during TPD before SO_2 adsorption. Thus, the author performed SO_2-TPD experiments before and after SO_2 adsorption by the samples. The SO_2 desorption amounts before (S1) and after (S2) the SO_2 adsorption treatment were calculated by integrating the peak areas, and the SO_2 adsorption amount was estimated from the difference between these values (S2 − S1).

The TPD profiles of the three catalysts showed different trends after SO_2 adsorption. For VMo/TiO_2, a small desorption peak was observed at approximately 400 °C, followed by a main peak starting at 450 °C with a maximum at 660 °C. For VMo/TS, SO_2 desorption started at 420 °C with two peaks occurring at 500 and 650 °C. Notably, for V/TSM, SO_2 desorption started at 370 °C with a predominant peak at 490 °C and a second peak at 610 °C. The lower onset temperature and the greater desorption peak at ~500 °C for V/TSM suggest that this catalyst possesses a superior SO_2 desorption capability. The TPD profiles collected before SO_2 adsorption exhibited similar trends but the peak areas were smaller.

The difference profiles for the SO_2-TPD data are shown in Figure 7(b). The desorption of SO_2 adsorbed on V/TSM started from 360 °C with a peak at 470 °C, which was lower than the temperature range for SO_2 desorption from the other two catalysts. Further, the amount of SO_2 adsorbed on V/TSM was estimated to be more than twice that on the other catalysts (Table 3).

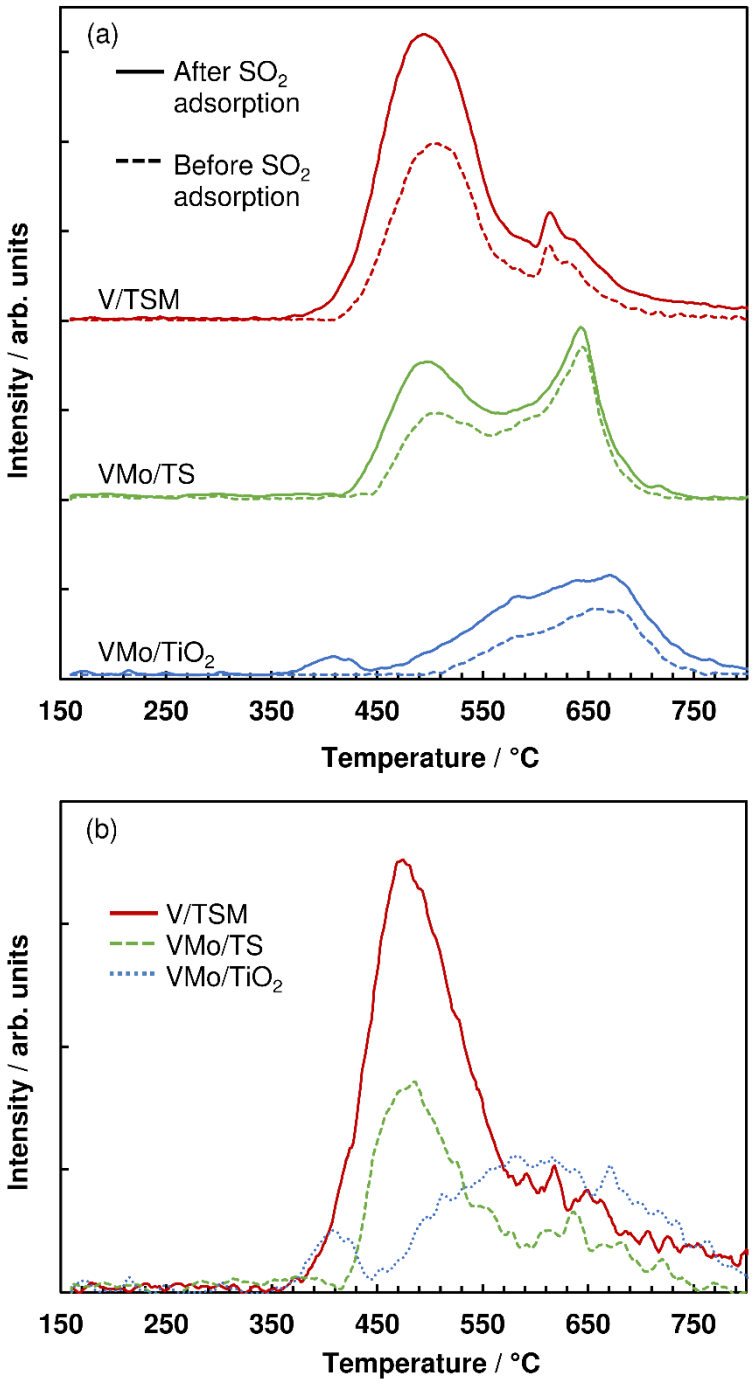

Figure 7. (a) TPD profiles of V/TSM, VMo/TS, and VMo/TiO_2 before and after SO_2 adsorption and (b) differences between the profiles before and after SO_2 adsorption.

As V/TSM exhibited less SO_2 accumulation and a smaller decrease in pore volume after the SO_2 durability test (Table 1), the author expected that this catalyst might suppress the adsorption of NH_3 or SO_2. However, the NH_3- and SO_2-TPD results revealed the opposite trend. Instead, these experiments suggested the possibility that V/TSM can enhance the desorption of SO_2. Thus, the author performed TPDC experiments for the catalysts impregnated with ABS, AS, or ATS to investigate the decomposition and desorption behaviors of ammonium sulfate salts.

Table 3. Amounts of desorbed SO_2 before (S1) and after (S2) SO_2 adsorption, and estimated amounts of adsorbed SO_2 (S2 − S1).

	SO_2 amount ($\mu mol \cdot g^{-1}$)		
	Before SO_2 adsorption (S1)	After SO_2 adsorption (S2)	Adsorbed SO_2 (S2 − S1)
VMo/TiO_2	12.8	21.9	9.1
VMo/TS	27.5	39.2	11.7
V/TSM	32.4	60.3	27.9

2.6. TPDC of Ammonium Sulfate Salts

The TPDC profiles of 1 wt% ABS, AS, or ATS supported on the catalysts are displayed in Figure 8. The signal at m/z = 15 was employed in this experiment to monitor NH_3 while avoiding interference from oxygen atoms (m/z = 16). As the intensity of the m/z = 15 signal is approximately 5% relative to that of the m/z = 17 signal [61], the data were multiplied by 20. The signals at m/z = 28 and 64 were used to monitor N_2 and SO_2, respectively, and the small signal at m/z = 30 (NO) was also detected.

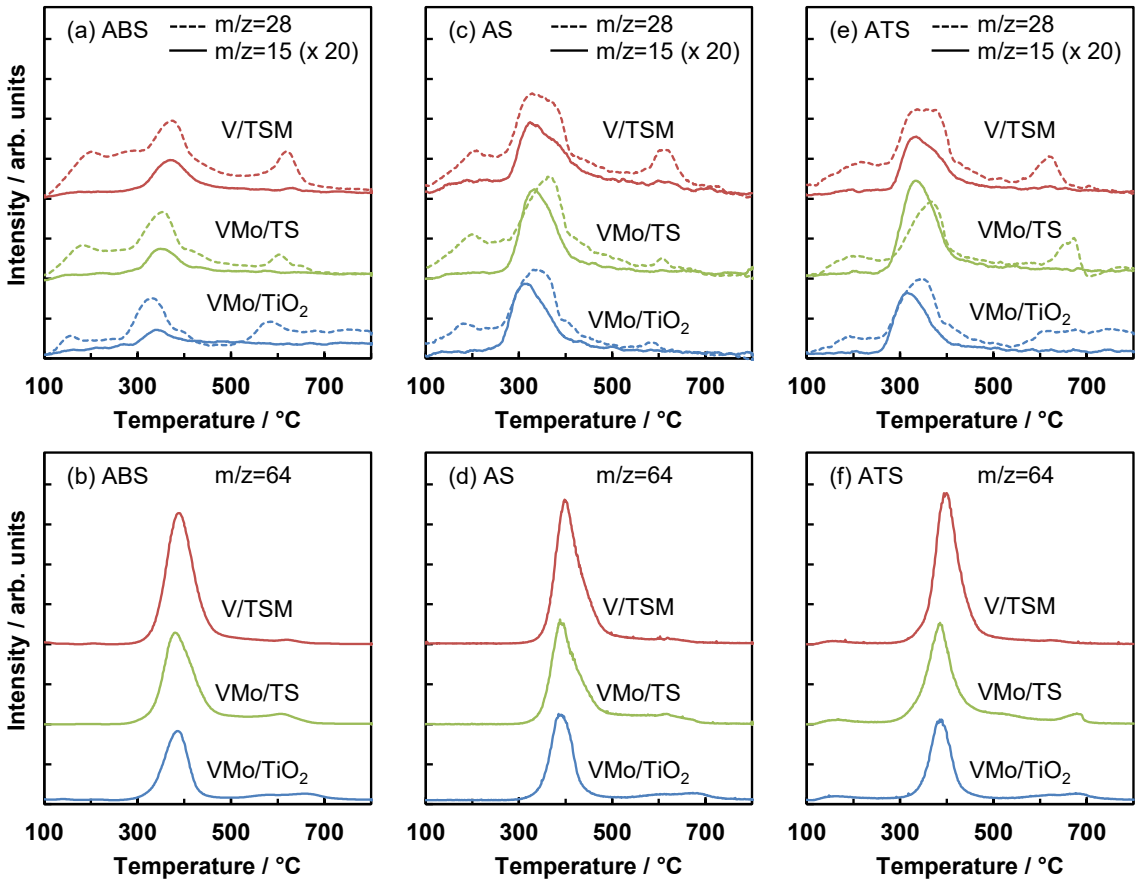

Figure 8. TPDC profiles of V/TSM, VMo/TS, and VMo/TiO_2 impregnated with (a,b) ABS, (c,d) AS, and (e,f) ATS.

Table 4. Desorbed amounts of NH_3, N_2, and SO_2 estimated from the peak areas of the TPDC profiles in Figure 8.

	ABS (μmol·g^{-1})			AS (μmol·g^{-1})			ATS (μmol·g^{-1})		
	NH_3	N_2	SO_2	NH_3	N_2	SO_2	NH_3	N_2	SO_2
VMo/TiO_2	25	260	199	49	359	216	37	280	209
VMo/TS	37	357	303	55	442	295	59	354	311
V/TSM	33	478	352	57	593	355	49	424	365

The author was unable to quantify the desorbed amounts accurately owing to interference by fragment ions from several compounds. Thus, a relative comparison based on the desorption peak areas was performed. The detected amounts of NH_3, N_2, and SO_2 estimated from the integrated TPDC peak areas are shown in Table 4.

For all the samples, N_2 desorption started at 100 °C with peaks observed in the ranges 300–400 °C and 500–700 °C; in addition, fluctuations occurred throughout the entire temperature range. According to the literature, the decomposition of sulfate salts on V_2O_5/TiO_2-type catalysts is enhanced in the presence of NO [37,62–65]. In the present study, ammonium species in the sulfate salts might be oxidized by lattice oxygens on the catalyst surface. The formed NO could then react with the ammonium species in the salts to form N_2. The fact that NO was detected in this experiment supports this hypothesis.

The amount of desorbed N_2 decreased in the following order: V/TSM > VMo/TS > VMo/TiO_2, regardless of the type of sulfate salt, in agreement with the order observed for NH_3-SCR durability (Figure 1). In addition, no distinct differences were observed between the catalysts for the temperatures at which NH_3 and N_2 desorption occurred. These results suggest that V/TSM has a greater number of active sites for the reaction of ammonium groups in the sulfate salts with NO than the other two catalysts. Hence, the decomposition of sulfate salts was enhanced on V/TSM and a greater amount of N_2 was formed.

The SO_2 desorption peak was observed at approximately 390 °C for all the samples. The amount of desorbed SO_2, formed by the decomposition of sulfate groups in the salts, decreased in the same order as for N_2. These results demonstrate that V/TSM possesses a greater number of active sites for decomposing the sulfate groups as well as the ammonium group of the salts.

2.7. Durability Enhancement Mechanism of V/TSM

Herein, the author elucidated that the formation of ATS and ABS is a crucial factor in SO_2 deactivation at temperatures lower than 200 °C. However, as ATS was formed on both V/TSM and VMo/TS, the formation of ATS itself is not responsible for the difference in durability.

In the TPDC experiments (Figure 8), the desorption of N_2 was observed at temperatures lower than 200 °C. This result suggested that both the formation and decomposition of ammonium sulfate salts occur during NH_3-SCR in the presence of SO_2 at low temperatures. Other research groups have reported that ABS deposited on V_2O_5/TiO_2-type catalysts can be decomposed by reacting with NO, and N_2 is formed in this reaction [37,62–65]. Yu et al. suggested that deposited ABS interacts with the Lewis acid sites on the catalyst surface, which enhances the reaction of NH_4^+ in ABS with NO [65]. On the contrary, Romero et al. described that the NH_3-SCR activities of V_2O_5/TiO_2-type catalysts at low temperatures are promoted by Brønsted acidity [66]. The NH_3-TPD results indicate that V/TSM possesses greater acidity than the other two catalysts (Figure 5), and the DRIFTS results suggested that Brønsted acid sites are predominant on V/TSM (Figure 6). Thus, the author believes that the reaction between NO and the sulfate salts was enhanced by the greater Brønsted acidity of the V/TSM catalyst.

By contrast, as a temperature higher than 300 °C is required for the desorption of SO_2 (Figure 7), it is difficult to decompose the sulfate groups in the sulfate salts at low temperatures. Nevertheless, for the catalyst with higher durability, less sulfur was accumulated (Table 1) and a greater amount of SO_2 was desorbed (Table 4). These results indicate that the deposited sulfur-containing compounds are partly desorbed as SO_2 during low-temperature NH_3-SCR under an actual reaction atmosphere. Yu et al. reported

that the decomposition and desorption of SO_4^{2-} on VMo/TiO_2 proceeds at low temperatures, which strongly supports the author's hypothesis [65].

The sulfur components in ABS and ATS are present as SO_4^{2-} and $S_2O_3^{2-}$, respectively. The formal valence states of sulfur are +6 in SO_4^{2-}, +2 in $S_2O_3^{2-}$, and +4 in SO_2, implying that the reduction of S^{6+} to S^{4+} and the oxidation of S^{2+} to S^{4+} are required for these sulfates to desorb as SO_2. The author previously reported that the redox of vanadium species is enhanced on V/TSM owing to active electron transfer between vanadium and TSM [57]. Similarly, the author believes that V/TSM can enhance the redox of sulfate salts deposited on the surface, which is expected to account for the observed enhancement of SO_2 desorption from V/TSM at low temperatures (Figure 7). Ye et al. reported that the acid sites on the catalyst are associated with electron transfer between V_2O_5/TiO_2-type catalysts and deposited ABS [67]. In this study, the acidity corresponded to the SO_2 desorption amount, demonstrating that the greater number of acid sites on V/TSM enhances the redox and desorption of sulfur species in deposited sulfur-containing compounds, thus suppressing the accumulation of sulfur.

In summary, the accumulation of ABS and ATS formed by a NH_3–SO_2–H_2O reaction (Equation (8)) is the crucial factor for the deactivation of low-temperature NH_3-SCR in the presence of SO_2. The acidity of the catalyst plays a key role in determining the reactivity of deposited ammonium sulfate salts with NO. Moreover, a greater acidity also contributes to the decomposition of sulfate groups in ammonium sulfate compounds. Hence, the superior SO_2 durability of V/TSM was brought about not by suppressing SO_2 adsorption but by enhancing the decomposition of ammonium and sulfate groups in ABS and ATS, which is associated with the solid acidity.

Thus, solid acidity plays an important role in SO_2 durability, and increasing the acidity is expected to further enhance the performance. However, excessive acidity is

known to reduce the NH_3-SCR activity [8]. Thus, strategies other than controlling the solid acidity are necessary to improve the SO_2 durability. As is apparent from Equation (8), H_2O is essential for the formation of ABS and ATS. Therefore, the formation of these sulfate salts could be suppressed by preventing the adsorption or accelerating the desorption of H_2O. The author expects the insights obtained in this study will aid in further improving the activity and durability of commercial NH_3-SCR catalysts.

3. Conclusions

In this study, the author showed that V/TSM exhibits superior durability for NH_3-SCR in the presence of SO_2 at low temperatures. Further, the deactivation mechanism and the factors affecting the durability were clarified by investigating the structures and behaviors of the ammonium sulfate salts accumulated on the catalyst surfaces. FT-IR analysis revealed the formation of NH_4HSO_4 (ABS) and $(NH_4)_2S_2O_3$ (ATS) after the low-temperature reaction, which enabled the author to propose the following reaction: $4NH_3 + 4SO_2 + 3H_2O \rightarrow (NH_4)_2S_2O_3 + 2NH_4HSO_4$, as one of the main routes for sulfate salt formation. As solid acid sites can enhance the reaction of the ammonium groups in ABS and ATS with NO, the decomposition of these sulfate salts was thought to be enhanced by the greater number of solid acid sites on the V/TSM catalyst. The greater acidity of V/TSM also affected the redox of sulfur ions in the deposited sulfur compounds and enhanced the desorption of SO_2. Thus, pore blocking by the accumulated sulfate salts was suppressed, resulting in the excellent durability of V/TSM. This clarification of the deactivation mechanism of NH_3-SCR catalysts by SO_2 at low temperatures suggests effective strategies for prolonging the catalyst lifetime. However, the detailed mechanisms for ATS formation and decomposition under the actual reaction atmosphere

remain unclear. The author will focus on these points in the future to realize more effective NH_3-SCR catalysts for practical applications in environmental protection.

4. Experimental

4.1. Catalyst Preparation

The catalysts were prepared using the procedures described in the author's previous studies [47,57]. The TSM support material ($TiO_2/SiO_2/MoO_3$ = 83:7:10) was prepared via a coprecipitation method. In brief, titanyl sulfate was dissolved in deionized water (Tayca Corp., 70 g/L TiO_2) and then mixed with silica-sol (Nissan Chemical, 30 wt%) and ammonium molybdate (Taiyo Koko) dissolved in an aqueous ammonia solution. The mixed slurry was filtered, dried at 150 °C, and calcined in air at 500 °C using a box-type electric furnace. The TS (TiO_2/SiO_2 = 93:7) and TiO_2 supporting materials were prepared via similar procedures.

The preparation method for the V/TSM honeycomb catalyst has been reported elsewhere [47,57]. In brief, a mixed solution of oxalic acid, monoethanol amine, and ammonium metavanadate was kneaded with the TSM powder. The clay-like kneaded material was then extruded to form a honeycomb monolithic catalyst with an outer diameter of 50 mm and a cell pitch of 3.2 mm. The molded honeycomb was dried at 60 °C and then calcined in an air atmosphere at 450 °C in a box-type electric furnace. The VMo/TS and VMo/TiO_2 catalysts were also prepared via the extrusion molding method. A mixed solution of monoethanol amine, oxalic acid, ammonium metavanadate, and ammonium molybdate was kneaded with the TS or TiO_2 powder. The cell pitch and the drying and calcination temperatures were the same as those for V/TSM. The vanadia loading amount for all the catalysts was fixed at 8 wt% V_2O_5. The final compositions of

the catalysts were VMo/TiO_2: 8 wt% V_2O_5, 10 wt% MoO_3, and 82 wt% TiO_2; VMo/TS: 8 wt% V_2O_5, 10 wt% MoO_3, 76.3 wt% TiO_2, and 5.7 wt% SiO_2; and V/TSM: 8 wt% V_2O_5, 9.2 wt% MoO_3, 76.4 wt% TiO_2, and 6.4 wt% SiO_2.

4.2. Characterization of Catalysts

The specific surface areas were measured by the BET method using a Mountech Macsorb Model 1210 apparatus. The samples were degassed in flowing N_2 at 200 °C for 60 min before the measurements. The sulfur contents were measured using a Bruker S8 Tiger X-ray fluorescence spectrometer. For these measurements, 4 g of powdered sample was pressed into a round-shaped disc with a diameter of 3 cm.

Porosity measurements were carried out with a porosimeter (AutoPore IV9520, Micromeritics). A sample of approximately 0.1 g was pretreated under flowing N_2 at 200 °C for 1 h. Subsequently, the porosity was measured via the mercury intrusion method in the pressure range of 0.007–414 MPa.

FT-IR spectroscopy was carried out using a Thermo Nicolet IS50 spectrometer in the range from 4000 to 400 cm^{-1} with a resolution of 2 cm^{-1} at 25 °C under flowing N_2 at atmospheric pressure. For these measurements, the catalyst sample was crushed and sieved to pass 100 mesh. Then, after mixing with potassium bromide (KBr) in a 1:60 ratio (w/w), 0.12 g of the mixed sample powder was pressed into a tablet with a diameter of 10 mm. A KBr tablet of the same size was used to collect the background. Eight sulfur- and nitrogen-containing reagents, namely, ammonium thiosulfate ($(NH_4)_2S_2O_3$), ammonium bisulfate (NH_4HSO_4), amidosulfuric acid ($HOSO_2NH_2$), hydroxyl ammonium sulfate ($(NH_3OH)_2SO_4$), ammonium persulfate ($(NH_4)_2S_2O_8$), ammonium amidosulfate ($NH_4OSO_2NH_2$), ammonium sulfite monohydrate ($(NH_4)_2SO_3 \cdot H_2O$), and ammonium sulfate ($(NH_4)_2SO_4$), were used for comparison with the used catalysts via FT-IR analysis.

Ammonium thiosulfate was purchased from Alfa Aesar, and the other reagents were obtained from Fujifilm Wako Pure Chemical Corporation. Each reagent was dissolved in deionized water at 25 °C and then mixed with the fresh V/TSM catalyst. After drying in air at 120 °C for 5 h, the mixture was ground in a mortar. The sulfur content of each sample was fixed at 5.0 wt% by varying the amount of reagent used.

A BEL-CAT apparatus (Bell Japan) was used for NH_3-TPD, SO_2-TPD, and TPDC experiments with the ammonium sulfate salts. The outlet gas was analyzed using a mass spectrometer (BEL-mass, Bell Japan) coupled to the BEL-CAT apparatus.

For the NH_3-TPD experiments, 100 mg of catalyst powder was placed in a U-shaped quartz tube and pretreated in flowing He at 400 °C for 1 h. After cooling to 100 °C, He gas containing 2% NH_3 was fed to the sample for 10 min. The sample was maintained at 100 °C and purged with helium gas for 30 min, and then the sample was heated to 600 °C at 10 °C/min.

The SO_2-TPD experiments were conducted using a similar method as for the NH_3-TPD experiments. In brief, 100 mg of catalyst powder was placed in a U-shaped quartz tube and pretreated in flowing He at 400 °C for 1 h. After cooling to 100 °C, He gas containing 2% SO_2 was fed to the sample for 10 min. The sample was maintained at 100 °C and purged with helium gas for 30 min, and then the sample was heated to 800 °C at 10 °C/min.

The TPDC experiments were carried out using samples prepared by the incipient wetness method. ABS, AS, or ATS was dissolved in deionized water and mixed with catalyst powders, which had previously been crushed and sieved to pass 100 mesh. The loading amounts of ABS, AS, and ATS were 1 wt%. The mixed sample was dried at 80 °C for 12 h in an air atmosphere in a box-type oven, and then the sample was crushed and sieved. Subsequently, 100 mg of the resultant powder was placed in a U-shaped quartz

tube and heated to 80 °C under flowing He. The sample was then heated to 800 °C at 10 °C/min under flowing He.

The DRIFTS experiment for a pyridine-adsorbed sample was performed using a Nicolet iS50 FT-IR spectrometer equipped with an *in situ* diffuse reflectance accessory. For this measurement, 30 mg of sample was placed on the sample stage and pretreated at 400 °C for 60 min under flowing air (40 cm^3/min). After cooling to 25 °C, the spectrum was collected. The sample was then heated to 150 °C and pyridine was supplied by flowing He (40 cm^3/min) through a saturator for 10 min. After purging with He (40 cm^3/min) at 150 °C for 120 min, the sample stage was cooled to 25 °C and the spectrum was collected. The spectrum of the sample before pyridine treatment was subtracted from that after treatment to obtain only the peaks corresponding to adsorbed pyridine.

4.3. Catalytic Activity Tests

The fixed-bed NH_3-SCR activity and durability tests in the presence of SO_2 were carried out under steady-state conditions. The honeycomb catalyst was cut to the size of 16 cells and placed in the stainless-steel reactor tube (3.8 cm inner diameter). After heating to the required temperature (160, 175, or 200 °C), the reaction gas consisting of 100 ppm NO, 100 ppm NH_3, 150 ppm SO_2, 10 vol% O_2, and 10 vol% H_2O with N_2 balance was fed to the catalyst for the activity tests. For the durability tests, the NH_3 concentration was changed to 80 ppm and then restored to 100 ppm every 100 h to check the activity. The gas hourly space velocity (GHSV) was 6,000 h^{-1}, and the concentrations of NO and NO_2 were measured using an on-line chemiluminescence NO_x analyzer (Thermo Fisher Scientific, Model 5100). A gas chromatograph (Shimadzu GC-14A) equipped with a Porapak-Q column was used to determine the N_2O concentration.

The following equation was used to calculate the conversion of NO.

$$\text{NO conversion} = \left(1 - \frac{[\text{outlet NO}]}{[\text{inlet NO}]}\right) \times 100\ (\%)$$

Acknowledgements

The author gratefully acknowledges funding and publication permission from Nippon Shokubai Co., Ltd.

References

[1] L. Lietti, J. Svachula, P. Forzatti, G. Busca, G. Ramis, P. Bregani, *Catal. Today* **1993**, *17*, 131–139.

[2] L. Lietti, P. Forzatti, *J. Catal.* **1994**, *147*, 241–249.

[3] N. Y. Topsøe, H. Topsøe, J. A. Dumesic, *J. Catal.* **1995**, *151*, 226–240.

[4] P. Ciambelli, M. E. Fortuna, D. Sannino, A. Baldacci, *Catal. Today* **1996**, *29*, 161–164.

[5] X. T. Gao, S. R. Bare, J. L. G. Fierro, I. E. Wachs, *J. Phys. Chem. B* **1999**, *103*, 618–629.

[6] S. T. Choo, Y. G. Lee, I.-S. Nam, S.-W. Ham, J.-B. Lee, *Appl. Catal. A Gen.* **2000**, *200*, 177–188.

[7] A. Burkardt, W. Weisweiler, T. J.A.A. van den, A. Schäfer-Sindlinger, E. S. Lox, *Top. Catal.* **2001**, *16*, 369–375.

[8] M. Kobayashi, R. Kuma, S. Masaki, N. Sugishima, *Appl. Catal. B Environ.* **2005**, *60*, 173–179.

[9] I. Giakoumelou, C. Fountzoula, C. Kordulis, S. Boghosian, *J. Catal.* **2006**, *239*,

1–12.

[10] S. Yamazoe, Y. Masutani, T. Shishido, T. Tanaka, *Res. Chem. Intermed.* **2008**, *34*, 487–494.

[11] T. Boningari, R. Koirala, P. G. Smirniotis, *Appl. Catal. B Environ.* **2012**, *127*, 255–264.

[12] T. Boningari, R. Koirala, P. G. Smirniotis, *Appl. Catal. B Environ.* **2013**, *140–141*, 289–298.

[13] M. A. Vuurman, I. E. Wachs, A. M. Hirt, *J. Phys. Chem.* **1991**, *95*, 9928–9937.

[14] L. Lietti, P. Forzatti, F. Bregani, *Ind. Eng. Chem. Res.* **1996**, *35*, 3884–3892.

[15] M. D. Amiridis, J. P. Solar, *Ind. Eng. Chem. Res.* **1996**, *35*, 978–981.

[16] I. E. Wachs, G. Deo, B. M. Weckhuysen, A. Andreini, M. A. Vuurman, M. de Boer, M. D. Amiridis, *J. Catal.* **1996**, *161*, 211–221.

[17] J. M. Herrmann, J. Disdier, *Catal. Today* **2000**, *56*, 389–401.

[18] E. Tronconi, I. Nova, C. Ciardelli, D. Chatterjee, M. Weibel, *J. Catal.* **2007**, *245*, 1–10.

[19] P. G. W. A. Kompio, A. Brückner, F. Hipler, G. Auer, E. Löffler, W. Grünert, *J. Catal.* **2012**, *286*, 237–247.

[20] A. Marberger, D. Ferri, M. Elsener, O. Kröcher, *Angew. Chemie Int. Ed.* **2016**, *55*, 11989–11994.

[21] B. Shen, F. Wang, B. Zhao, Y. Li, Y. Wang, *J. Ind. Eng. Chem.* **2016**, *33*, 262–269.

[22] M. Zhu, J. K. Lai, U. Tumuluri, Z. Wu, I. E. Wachs, *J. Am. Chem. Soc.* **2017**, *139*, 15624–15627.

[23] J.-K. Lai, I. E. Wachs, *ACS Catal.* **2018**, *8*, 6537–6551.

[24] L. Casagrande, L. Lietti, I. Nova, P. Forzatti, A. Baiker, *Appl. Catal. B Environ.*

1999, *22*, 63–77.

[25] L. Lietti, I. Nova, G. Ramis, L. Dall'Acqua, G. Busca, E. Giamello, P. Forzatti, F. Bregani, *J. Catal.* **1999**, *187*, 419–435.

[26] Y. Gao, T. Luan, T. Lv, H. M. Xu, *Adv. Mater. Res.* **2012**, *573–574*, 58–62.

[27] Y. Qiu, B. Liu, J. Du, Q. Tang, Z. Liu, R. Liu, C. Tao, *Chem. Eng. J.* **2016**, *294*, 264–272.

[28] R. Wu, N. Zhang, X. Liu, L. Li, L. Song, W. Qiu, H. He, *Catal. Letters* **2018**, *148*, 1228–1235.

[29] D. W. Kwon, K. H. Park, H. P. Ha, S. C. Hong, *Appl. Surf. Sci.* **2019**, *481*, 1167–1177.

[30] Y. Xu, X. Wu, Q. Lin, J. Hu, R. Ran, D. Weng, *Appl. Catal. A Gen.* **2019**, *570*, 42–50.

[31] R. K. Srivastava, C. A. Miller, C. Erickson, R. Jambhekar, *J. Air Waste Manage. Assoc.* **2004**, *54*, 750–762.

[32] F. Nakajima, I. Hamada, *Catal. Today* **1996**, *29*, 109–115.

[33] Z. Zhu, Z. Liu, S. Liu, H. Niu, *Appl. Catal. B Environ.* **2001**, *30*, 267–276.

[34] D. W. Kwon, K. H. Park, S. C. Hong, *Chem. Eng. J.* **2016**, *284*, 315–324.

[35] Y. Xi, N. A. Ottinger, Z. G. Liu, *Appl. Catal. B Environ.* **2014**, *160–161*, 1–9.

[36] H. H. Phil, M. P. Reddy, P. A. Kumar, L. K. Ju, J. S. Hyo, *Appl. Catal. B Environ.* **2008**, *78*, 301–308.

[37] Y. J. Shi, H. Shu, Y. H. Zhang, H. M. Fan, Y. P. Zhang, L. J. Yang, *Fuel Process. Technol.* **2016**, *150*, 141–147.

[38] P. G. Smirniotis, D. A. Peña, B. S. Uphade, *Angew. Chemie Int. Ed.* **2001**, *40*, 2479–2482.

[39] Z. Wu, R. Jin, Y. Liu, H. Wang, *Catal. Commun.* **2008**, *9*, 2217–2220.

[40] P. R. Ettireddy, N. Ettireddy, T. Boningari, R. Pardemann, P. G. Smirniotis, *J. Catal.* **2012**, *292*, 53–63.

[41] T. Boningari, P. R. Ettireddy, A. Somogyvari, Y. Liu, A. Vorontsov, C. A. McDonald, P. G. Smirniotis, *J. Catal.* **2015**, *325*, 145–155.

[42] Z. Sheng, Y. Hu, J. Xue, X. Wang, W. Liao, *J. Rare Earths* **2012**, *30*, 676–682.

[43] D. K. Pappas, T. Boningari, P. Boolchand, P. G. Smirniotis, *J. Catal.* **2016**, *334*, 1–13.

[44] T. Boningari, D. K. Pappas, P. G. Smirniotis, *J. Catal.* **2018**, *365*, 320–333.

[45] D. Damma, P. R. Ettireddy, B. M. Reddy, P. G. Smirniotis, *Catalysts* **2019**, *9*, 349.

[46] L. Lietti, I. Nova, P. Forzatti, *Top. Catal.* **2000**, *11–12*, 111–122.

[47] M. Kobayashi, R. Kuma, A. Morita, *Catal. Letters* **2006**, *112*, 37–44.

[48] X. Wang, X. Du, S. Liu, G. Yang, Y. Chen, L. Zhang, X. Tu, *Appl. Catal. B Environ.* **2020**, *260*, 118168.

[49] L. Zhu, Z. Zhong, J. Xue, Y. Xu, C. Wang, L. Wang, *J. Environ. Sci.* **2018**, *65*, 306–316.

[50] R. Kuma, T. Kitano, T. Tsujiguchi, T. Tanaka, *Ind. Eng. Chem. Res.* **2020**, *59*, 13467–13476.

[51] Q. Liang, J. Li, H. He, W. Liang, T. Zhang, X. Fan, *Front. Environ. Sci. Eng.* **2017**, *11*, 4.

[52] G. A. Newman, *J. Mol. Struct.* **1970**, *5*, 61–66.

[53] M.-I. Kim, G.-H. Lee, D.-W. Kim, D.-H. Kang, D.-W. Park, *Korean J. Chem. Eng.* **2014**, *31*, 2162–2169.

[54] J. Janlamool, B. Jongsomjit, *J. Oleo Sci.* **2017**, *66*, 1029–1039.

[55] M. Itoh, H. Hattori, K. Tanabe, *J. Catal.* **1974**, *35*, 225–231.

[56] M. Kobayashi, M. Hagi, *Appl. Catal. B Environ.* **2006**, *63*, 104–113.

[57] R. Kuma, T. Kitano, T. Tsujiguchi, T. Tanaka, *Appl. Catal. A Gen.* **2020**, *595*, 117496.

[58] J. Datka, A. M. Turek, J. M. Jehng, I. E. Wachs, *J. Catal.* **1992**, *135*, 186–199.

[59] G. Berhault, M. Lacroix, M. Breysse, F. Maugé, J.-C. Lavalley, H. Nie, L. Qu, *J. Catal.* **1998**, *178*, 555–565.

[60] W. Li, K. Oshihara, W. Ueda, *Appl. Catal. A Gen.* **1999**, *182*, 357–363.

[61] G. A. A. Cruz-Diaz, G. M. M. Muñoz Caro, A. Jiménez-Escobar, *EAS Publ. Ser.* **2012**, *58*, 333–336.

[62] Z. Zhu, H. Niu, Z. Liu, S. Liu, *J. Catal.* **2000**, *195*, 268–278.

[63] G. Baltin, H. Köser, K.-P. Wendlandt, *Catal. Today* **2002**, *75*, 339–345.

[64] X. Wang, X. Du, L. Zhang, G. Yang, Y. Chen, J. Ran, *Energy and Fuels* **2018**, *32*, 6990–6994.

[65] J. Yu, E. Zhang, L. Wang, Z. Song, F. Kong, Y. Ma, H. Zhao, L. Sun, *Energy and Fuels* **2020**, *34*, 2107–2116.

[66] M. Aguilar-Romero, R. Camposeco, S. Castillo, J. Marín, V. Rodríguez-González, L. A. García-Serrano, I. Mejía-Centeno, *Fuel* **2017**, *198*, 123–133.

[67] D. Ye, R. Qu, H. Song, C. Zheng, X. Gao, Z. Luo, M. Ni, K. Cen, *RSC Adv.* **2016**, *6*, 55584–55592.

Chapter 6

General Conclusions

The author investigated the physico-chemical characteristics of the transition metal oxide catalysts for the waste gas treatment throughout this thesis, and the relationship between active-site structures and catalytic activities has been elucidated for NO-CO-O_2 reaction, *o*-chlorotoluene decomposition, and NH_3-SCR. The author proposed new mechanisms for superior activity and durability for the low-temperature NO_x/dioxins abatement reaction over the V/TSM catalyst, as well as new characterization methods for supported Cu catalysts.

In Chapter 2, the local structure around Cu supported on Al_2O_3 was characterized, and the relationship between catalytic performance for NO-CO-O_2 reaction and state of supported Cu species was discussed. A new method for estimating the fraction of aggregated Cu species to isolated Cu species was proposed from the spectroscopic analyses. The active sites for the NO–CO–O_2 reaction are confirmed to be the isolated Cu^{2+} species supported on γ-Al_2O_3, and coexistence of the aggregated Cu species drastically reduces the activity of NO reduction. The analysis method obtained here, namely, the XAFS analysis in combination with other spectroscopy, paved the way for the detailed analyses of the V/TSM catalyst, as reported in Chapters 3 and 4.

In Chapter 3, the author reports the physico-chemical analysis on the structure of the V/TSM catalyst that exhibits excellent activity for *o*-chlorotoluene decomposition at low temperatures, as well as NH_3-SCR (Chapter 4). Throughout the XAFS spectroscopy, the author unraveled that the molybdenum species in the TSM support material were highly dispersed as Mo^{6+}, replacing Ti^{4+} in the anatase TiO_2 framework, forming a TSM

solid solution. The redox capability of the vanadium species in the catalyst is enhanced by electron transfer from the TSM support to vanadium, likely due to the coexistence of Mo^{6+} and Ti^{4+} in the TSM solid solution, which has a unique structure. The author concluded that the enhanced redox capability of V/TSM is responsible for the superior oxidative decomposition activity of *o*-chlorotoluene, which shows similar decomposition behavior to dioxins.

In Chapter 4, the structures of the V/TSM catalyst for the NH_3-SCR at low temperatures were investigated using *in-situ* V K-edge XANES measurements. The V/TSM showed a significantly steep increase in the main-edge energy at the beginning of the reaction. The author clarified that the excellent NH_3-SCR catalytic activity of V/TSM can be ascribed to the remarkable V^{4+}-to-V^{5+} reoxidation capability, and the easier V^{5+}-to-V^{4+} reducibility. This improved redox reactivity is induced by the interaction of the highly dispersed polymeric vanadate with TSM solid solution and by the appropriate surface geometry of vanadium species, which enabled contact with NH_3 and O_2 in the gas phase.

In Chapter 5, the deactivation mechanism of the NH_3-SCR catalysts was investigated. The V/TSM catalyst was demonstrated to have excellent durability for NH_3-SCR in the presence of SO_2 at temperatures lower than 200 °C. The author unraveled that ammonium sulfate salts were formed on catalyst surfaces by NH_3–SO_2–H_2O reactions at low temperatures, resulting in catalyst deactivation via pore blockage. The author proposed the following new reaction: $4NH_3 + 4SO_2 + 3H_2O \rightarrow (NH_4)_2S_2O_3 + 2NH_4HSO_4$, as one of the main routes for sulfate salt formation. Moreover, V/TSM was found to possess an increased number of active sites for decomposing deposited ammonium sulfate salts. The decomposition activity was related to the solid acidity, which enhanced SO_2 desorption and reactions between ammonium sulfate salts and NO.

In summary, the author investigated the physico-chemical characteristics of the V/TSM catalyst, applying the XAFS analysis methods acquired in Chapter 2. The overview of the catalytic activity and durability enhancement mechanism of the V/TSM catalyst is displayed in Figure 1. Herein, the author has elucidated that the redox capability of the vanadium species in this catalyst is enhanced by electron transfer from the TSM support to vanadium. This behavior of the TSM support is also effective for enhancing the dioxins decomposition activity (Chapter 3) and accelerating the decomposition of ammonium sulfate salts (Chapter 5). Further, the local structure around vanadium in the V/TSM catalyst was unraveled. The contact of the vanadium species and gaseous molecules is not inhibited by the surface molybdenum oxide, as molybdenum is incorporated into the TSM support (Chapter 4). By employing these findings in future catalyst research, such as, by enhancing further redox capability, and by designing surface geometries that enable easier access for gaseous molecules to the vanadium species, the development of novel catalysts that exhibit remarkably higher performance for the waste gas treatment can be expected.

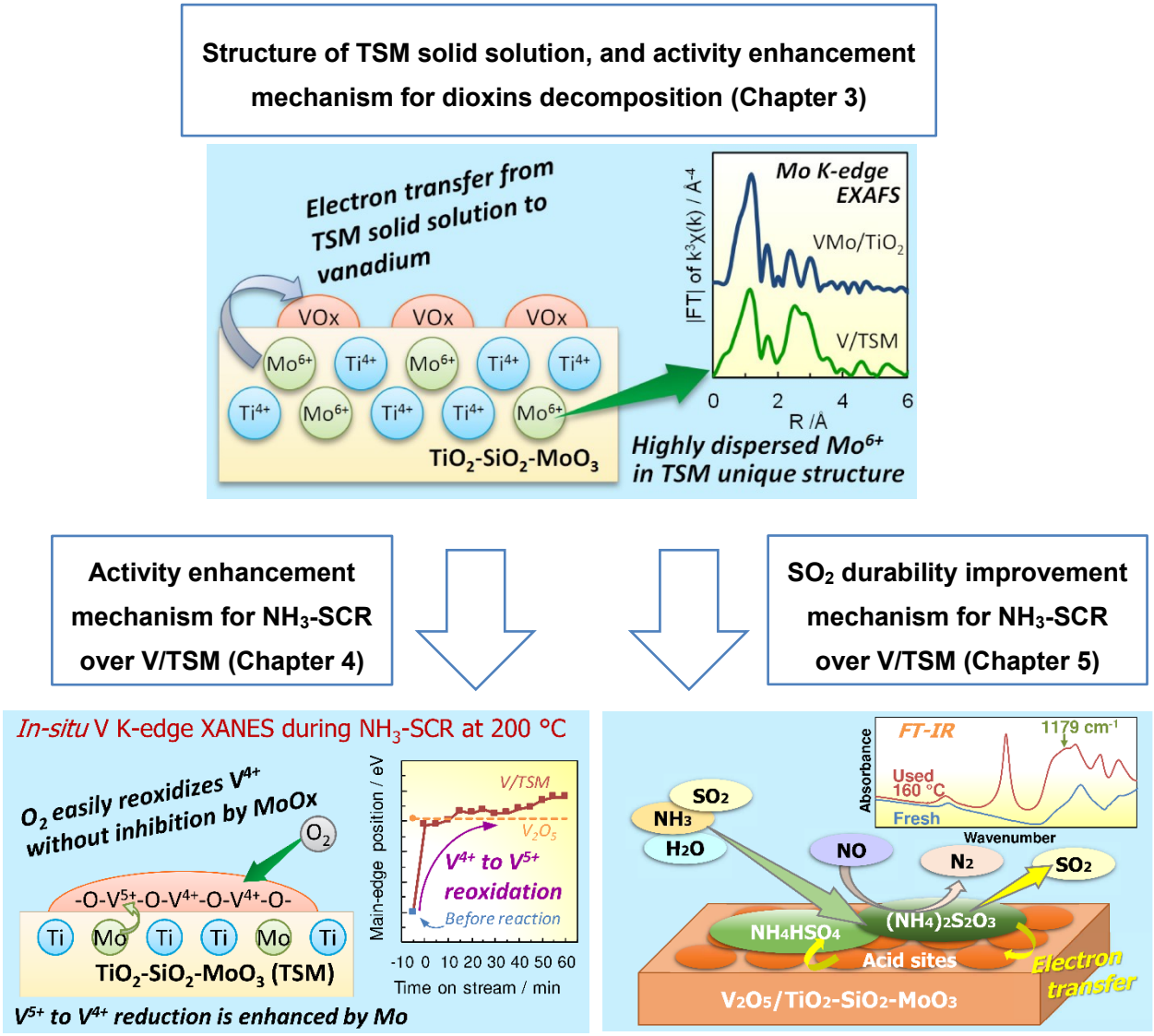

Figure 1. Graphical overview of catalytic activity and durability enhancement mechanism for the NH_3-SCR reaction over the V/TSM catalyst.

List of Publications

Publications Related to the Works Described in This Thesis

Chapter 2:

1. Takashi Yamamoto, Tsunehiro Tanaka, Sosuke Suzuki, Ryoji Kuma, Kentaro Teramura, Yuan Kou, Takuzo Funabiki and Satohiro Yoshida, *Top. Catal.* **2002**, *18*, 113–118. DOI: 10.1023/A:1013897331031
   "NO reduction with CO in the presence of O_2 over Cu/Al_2O_3 (3) –structural analysis of active species by means of XAFS and UV/VIS/NIR spectroscopy"

Chapter 3:

2. Ryoji Kuma, Tomoyuki Kitano, Takuya Tsujiguchi, Tsunehiro Tanaka, *Appl. Catal. A Gen.* **2020**, *595*, 117496. DOI: 10.1016/j.apcata.2020.117496
   "Effect of molybdenum on the structure and performance of $V_2O_5/TiO_2–SiO_2–MoO_3$ catalysts for the oxidative degradation of *o*-chlorotoluene"

Chapter 4:

3. Ryoji Kuma, Tomoyuki Kitano, Takuya Tsujiguchi, Tsunehiro Tanaka, *Ind. Eng. Chem. Res.* **2020**, *59*, 13467–13476. DOI: 10.1021/acs.iecr.0c02308
   "In-situ XANES characterization of V_2O_5/TiO_2-SiO_2-MoO_3 catalyst for selective catalytic reduction of NO by NH_3"

Chapter 5:

4. Ryoji Kuma, Tomoyuki Kitano, Takuya Tsujiguchi, Tsunehiro Tanaka, *ChemCatChem* **2020**, *12*, 5938–5947. DOI: 10.1002/cctc.202001155
   "Deactivation mechanism and enhanced durability of V_2O_5/TiO_2-SiO_2-MoO_3 catalysts for NH_3-SCR in the presence of SO_2"

Publications Not Included in This Thesis

1. Takashi Yamamoto, Tsunehiro Tanaka, Ryoji Kuma, Sosuke Suzuki, Fumiaki Amano, Yutaka Shimooka, Yoshiumi Kohno, Takuzo Funabiki, Satohiro Yoshida, *Phys. Chem. Chem. Phys*., **2002**, *4*, 2449-2458. DOI: 10.1039/B201120B
   "NO reduction with CO in the presence of O_2 over Al_2O_3-supported and Cu-based catalysts"

2. Noboru Sugishima, Sinyuki Masaki, Junichiro Kugai, Ryoji Kuma, Motonobu Kobayashi, *Stud. Surf. Sci. Catal.* **2003**, *145*, 473–474. DOI: 10.1016/S0167-2991(03)80266-5
   "Development of a low-temperature dioxin decomposition catalyst"

3. Motonobu Kobayashi, Ryoji Kuma, Sinyuki Masaki, Noboru Sugishima, *Appl. Catal. B Environ.* **2005**, *60*, 173–179. DOI: 10.1016/j.apcatb.2005.02.030
   "TiO_2-SiO_2 and V_2O_5/TiO_2-SiO_2 catalyst: Physico-chemical characteristics and catalytic behavior in selective catalytic reduction of NO by NH_3"

4. Motonobu Kobayashi, Ryoji Kuma, Atsushi Morita, *Catal. Letters* **2006**, *112*, 37–44. DOI: 10.1007/s10562-006-0161-4
"Low temperature selective catalytic reduction of NO by NH_3 over V_2O_5 supported on TiO_2–SiO_2–MoO_3"

5. Ryoji Kuma, Motonobu Kobayashi, Sinyuki Masaki, Noboru Sugishima, *Stud. Surf. Sci. Catal*. **2007**, *172*, 605–606. DOI: 10.1016/B978-0-444-53202-2.50162-7
"Influence of physico-chemical characteristics of support on selective catalytic reduction of NO by NH_3 and SO_2 oxidation over V_2O_5/TiO_2-SiO_2"

6. Ryoji Kuma, *Shokubai* **2020**, *62*, 185–189.
"Wastewater treatment process and catalyst technology for the catalytic wet oxidation method" (in Japanese)

Patents (U.S.)

1. Shinyuki Masaki, Ryoji Kuma, Noboru Sugishima,
   "Catalyst for purification of exhaust gases, production process therefor, and process for purification of exhaust gases"
   U.S. Patent 6638486, **2003**.

2. Shinyuki Masaki, Ryoji Kuma, Noboru Sugishima,
   "Catalyst for purification of exhaust gases, production process therefor, and process for purification of exhaust gases"
   U.S. Patent 6884402, **2005**.

3. Ryoji Kuma, Shinyuki Masaki, Noboru Sugishima,
   "Method for treating exhaust gas"
   U.S. Patent 7264784, **2007**.

4. Atsuhi Morita, Ryoji Kuma, Shinyuki Masaki, Motonobu Kobayashi,
   "Titanium oxide, catalyst for treating exhaust gas and method for purifying exhaust gas"
   U.S. Patent 8173098, **2012**.

Patents (JP)

5. Junichiro Kugai, Ryoji Kuma, Shinyuki Masaki, Atsushi Morita, Noboru Sugishima, *JP2001113167A*, ***2000***.
   "Exhaust gas treating catalyst, its manufacturing method and method for treating exhaust gas"

6. Junichiro Kugai, Ryoji Kuma, Shinyuki Masaki, Atsushi Morita, Noboru Sugishima, *JP2001113169A*, ***2000***.
   "Exhaust gas treating catalyst and method for treating exhaust gas"

7. Ryoji Kuma, Shinyuki Masaki, Noboru Sugishima, *JP2001321667A*, ***2000***.
   "Catalyst for treating waste gas, method for treating waste gas and manufacturing method of catalyst for treating waste gas"

8. Masaichi Hashimoto, Ryoji Kuma, Shinyuki Masaki, Noboru Sugishima, *JP20020066336A*, ***2000***.
   "Organic halogen compound decomposition catalyst and its preparation process and application"

9. Ryoji Kuma, Shinyuki Masaki, Atsushi Morita, Noboru Sugishima, *JP20021102655A*, ***2000***.
   "Treating method for waste gas containing dioxin or the like"

10. Ryoji Kuma, Shinyuki Masaki, Noboru Sugishima, *JP2003112046A*, ***2001***.
    "Waste gas treating catalyst and method"

11. Ryoji Kuma, Shinyuki Masaki, Noboru Sugishima, *JP2003112047A*, ***2001***.
    "Waste gas treatment catalyst and method"

12. Ryoji Kuma, Shinyuki Masaki, Noboru Sugishima, *JP2004081994A*, ***2002***.
"Waste gas treatment catalyst and method of treating waste gas using the same"

13. Ryoji Kuma, Shinyuki Masaki, Noboru Sugishima, *JP2004081995A*, ***2002***.
"Denitration catalyst and denitration method using the same"

14. Ryoji Kuma, Shinyuki Masaki, Noboru Sugishima, *JP2005125211A*, ***2003***.
"Exhaust gas treatment method"

15. Ryoji Kuma, Shinyuki Masaki, Noboru Sugishima, *JP2005125212A*, ***2003***.
"Exhaust gas treatment method"

16. Ryoji Kuma, Shinyuki Masaki, Noboru Sugishima, *JP2005125213A*, ***2003***.
"Exhaust gas treatment method"

17. Ryoji Kuma, Shinyuki Masaki, Noboru Sugishima, *JP2005144300A*, ***2003***.
"Exhaust gas treating catalyst and exhaust gas treating method"

18. Ryoji Kuma, Atsushi Morita, Noboru Sugishima, *JP2005270872A*, ***2004***.
"Catalyst for exhaust gas treatment and exhaust gas treatment method"

19. Ryoji Kuma, Shinyuki Masaki, *JP2006150352A*, ***2004***.
"Catalyst and method for exhaust gas treatment"

20. Ryoji Kuma, *JP2006320803A*, ***2005***.
"Catalyst and method for treating exhaust gas"

21. Motonobu Kobayashi, Ryoji Kuma, *JP2007313474A*, ***2006***.
"Catalyst and method for treating exhaust gas"

22. Mitsuharu Hagi, Ryoji Kuma, Atsushi Morita, Hiroki Tsutsumi, *JP2008264604A*, ***2007***.
"Catalyst for treating waste gas, manufacturing method of the catalyst and treating method of organic halogen compound in waste gas using the catalyst"